UNIVERSITÄT OSNABRÜCK

Cantilever properties and noise figures in high-resolution non-contact atomic force microscopy

Dissertation

zur Erlangung des Grades eines
Doktors der Naturwissenschaften (Dr. rer. nat.)
am Fachbereich Physik der Universität Osnabrück

vorgelegt von

Jannis Ralph Ulrich Lübbe

geboren in Herford

Osnabrück, November 2012

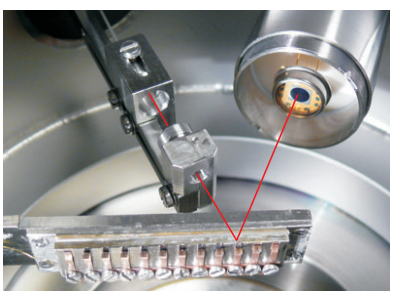
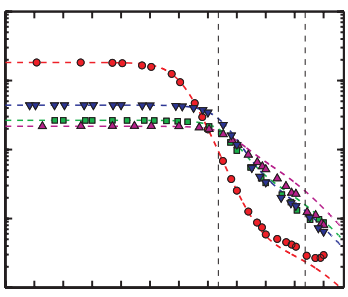
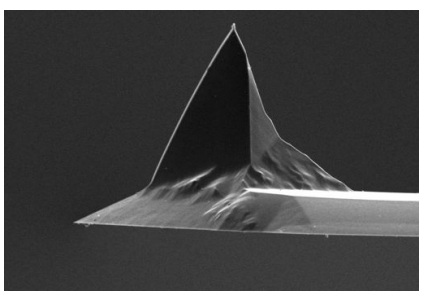

Contents

1 Introduction **1**

2 Fundamentals **3**
2.1 NC-AFM principle . . . 3
2.2 Force and frequency shift in NC-AFM . . . 5
2.2.1 Frequency shift from tip-sample interaction . . . 7
2.2.2 Normalised frequency shift . . . 8
2.2.3 Force from frequency shift . . . 9
2.3 NC-AFM cantilevers . . . 17
2.3.1 Oscillation modes . . . 18
2.3.2 Frequency response . . . 22
2.3.3 Thermally excited cantilever oscillation . . . 23
2.4 Phase-Locked-Loop (PLL) and amplitude control . . . 28
2.5 Optimisation of imaging parameters . . . 32
2.5.1 Stability and jump-to-contact . . . 32
2.5.2 Noise for negligible tip-sample interaction . . . 33
2.5.3 Noise with significant tip-sample interaction . . . 33
2.5.4 Bandwidth, scan speed and thermal drift . . . 39
2.6 Experimental setups . . . 47
2.6.1 Omicron UHV AFM/STM (system A) . . . 47
2.6.2 Omicron VT AFM/STM (system B) . . . 48
2.6.3 RHK UHV 750 (system C) . . . 48
2.6.4 Cantilever test chamber . . . 53
2.6.5 Scanning electron microscope (SEM) . . . 53
2.6.6 Static cantilever stiffness measurement . . . 56

3 Achieving high effective Q-factors in ultra-high vacuum dynamic force microscopy **57**
J. Lübbe, L. Tröger, S. Torbrügge, R. Bechstein, C. Richter, A. Kühnle, M. Reichling
Measurement Science and Technology **21**, 125501 (2010)

4 Measurement and modelling of non-contact atomic force microscope cantilever properties from ultra-high vacuum to normal pressure conditions **59**
J. Lübbe, M. Temmen, H. Schnieder, M. Reichling
Measurement Science and Technology **22**, 055501 (2011)

5 Precise determination of force microscopy cantilever stiffness from dimensions and eigenfrequencies **61**
J. Lübbe, L. Doering, M. Reichling
Measurement Science and Technology **23**, 045401 (2012)

6 Thermal noise limit for ultra-high vacuum noncontact atomic force microscopy **63**
J. Lübbe, M. Temmen, S. Rode, P. Rahe, A. Kühnle, M. Reichling
Beilstein Journal of Nanotechnology **4**, 32 (2013)

7 Determining cantilever stiffness from thermal noise **65**
J. Lübbe, M. Temmen, P. Rahe, A. Kühnle, M. Reichling
Beilstein Journal of Nanotechnology **4**, 227 (2013)

8 Summary **67**

Bibliography **71**

Publications and presentations **79**

1 Introduction

The cornerstone of scanning probe microscopy (SPM) was set in the year 1981 with the invention of the scanning tunneling microscope (STM) [1] by Gerd Binnig and Heinrich Rohrer, who were awarded the 1986 Nobel Price in Physics. The STM for the first time allowed measuring surface topographies in real space at the atomic scale [2]. Its application range, however, is limited to surfaces providing at least a minimum electrical conductivity. The invention of the STM was followed by the atomic force microscope (AFM) in 1986 [3], which determines the force acting between a probe tip and the surface. Most often, this is realised by measuring the displacement of a cantilever, to which the tip is attached, by optical methods. Although most AFM systems are operated in ambient conditions, an ultra-high vacuum (UHV) or a clean liquid environment is required for studies at the atomic level making AFM operation more challenging. In non-contact atomic force microscopy (NC-AFM), utilizing the frequency modulation (FM) technique [4], the cantilever is oscillated at its resonance frequency close to the sample surface and forces acting between tip and sample yield a slight shift of the resonance frequency. This frequency shift can be measured with high accuracy using a phase-locked loop (PLL) as FM demodulator. In 1995 atomically resolved images of the silicon(111) surface were presented for the first time by Giessibl *et al.* [5] as well as by Kitamura *et al.* [6] using the NC-AFM technique. The great advantage over the STM is that the NC-AFM allows for obtaining atomic resolution on strongly ionic insulators [7, 8] as well as on insulating metal oxides [9]. Most impressively, the development of this technique lead to the chemical identification of individual surface atoms using high-precision force spectroscopy [10]. As the latest development, the combination of lateral scanning with force-distance spectroscopy is used to measure force fields above the surface as three-dimensional force maps with atomic resolution [11–15]. Such measurements are extremely elaborative, touching the border of both, technical possibilities and physical limits.

Remaining issues to be solved for even more enhanced NC-AFM imaging and spectroscopy are the limits given by noise on a small time scale as well as by thermal drift on a larger time scale. Most dominant contributions to noise in FM-AFM are thermal noise from the cantilever and instrumental noise generated in the detection system measuring the cantilever oscillation [16, 17]. The impact of thermal noise in an NC-AFM measurement is mainly governed by the ambient temperature and cantilever properties. Due to the high quality factors (Q-factors) of cantilevers operated under UHV conditions, the thermal noise contribution is typically small compared to the detection system noise in a large bandwidth measurement. Important experimental parameters for characterising the total noise in the frequency shift signal are the cantilever oscillation amplitude and the frequency

response of the FM demodulator. Upon bringing the tip in close proximity to the sample, additional noise sources appear due to a coupling of the PLL to the amplitude control loop [18], while instabilities in the distance control loop further contribute to the overall noise. To obtain an optimum signal-to-noise ratio, the cantilever properties as well as the oscillation amplitude have to be considered [19]. Besides the frequency noise on a short time scale, thermal drift of the cantilever eigenfrequency disturbs the accuracy of frequency shift measurements [20, 21]. Thermal drift in the instrument yields distorted images, especially at slow scan speeds. These distortions can either be removed offline by a detailed analysis of the recorded images [22] or can be prevented by an online drift correction using atom-tracking in combination with the feed-forward technique [15, 23, 24].

In this thesis, I investigate and develop strategies for determining various cantilever properties under different conditions. Furthermore, I explore the influence of these properties and NC-AFM system settings on the noise in the cantilever displacement and frequency shift signals from both, theoretical and experimental studies. The thesis consists of an introductory section in Chapter 2 and five journal articles presented in Chapters 3 to 7. Chapter 2 provides an overview of the NC-AFM principle, tip-sample interactions, the cantilever oscillation and its control by a PLL system. This introduction is followed by considerations regarding the optimisation of imaging parameters and a description of the experimental setups used within this work. Although the focus of this thesis is on the modelling and measurement of frequency shift noise, the effect of thermal drift on NC-AFM images for typical experimental conditions is illustrated by simulated data.

In Chapter 3, the Q-factors of cantilevers are investigated as a function of material properties and dimensions. The dependence of the Q-factor and the cantilever resonance frequency on the surrounding medium is discussed in Chapter 4. An even more important cantilever property is the stiffness, required for a quantitative analysis of force imaging and spectroscopy results [14, 25, 26]. In Chapter 5, a methodology is presented to derive the static stiffness from the knowledge of cantilever dimensions and material parameters. This method suffers from the large uncertainty in the determination of the cantilever thickness, however, including the eigenfrequency in the calculation can significantly reduce the uncertainty provided the tip mass is known. Results for the stiffness determination are verified by high-precision tip-destructive static measurements performed at the Physikalisch-Technische Bundesanstalt (PTB, Braunschweig, Germany).

The dependence of the cantilever displacement and frequency shift noise on cantilever properties and system parameters is discussed in Chapter 6. This includes the determination of the detection system noise floor and an investigation of the PLL frequency response. Finally, a method to determine cantilever properties and specifically modal stiffness from the measurement of fluctuations of a thermally excited cantilever is discussed in Chapter 7. Utilizing the relationship between the cantilever thermal excitation and the frequency shift noise at the output of the PLL demodulator, a simple method for the stiffness determination is presented. This bypasses the difficult procedures of high-resolution spectral analysis of the cantilever resonances required for displacement noise measurements.

2 Fundamentals

2.1 NC-AFM principle

A typical NC-AFM setup is schematically depicted in Fig. 2.1. The centrepiece of such a system is an oscillating probe sensing tip-sample interactions. Typical NC-AFM probes are cantilevers, tuning fork sensors [27] and needle sensors [28]. Depending on the sensor type, the oscillation is detected via optical beam deflection (OBD), laser interferometry, piezoelectricity or piezoresistance.

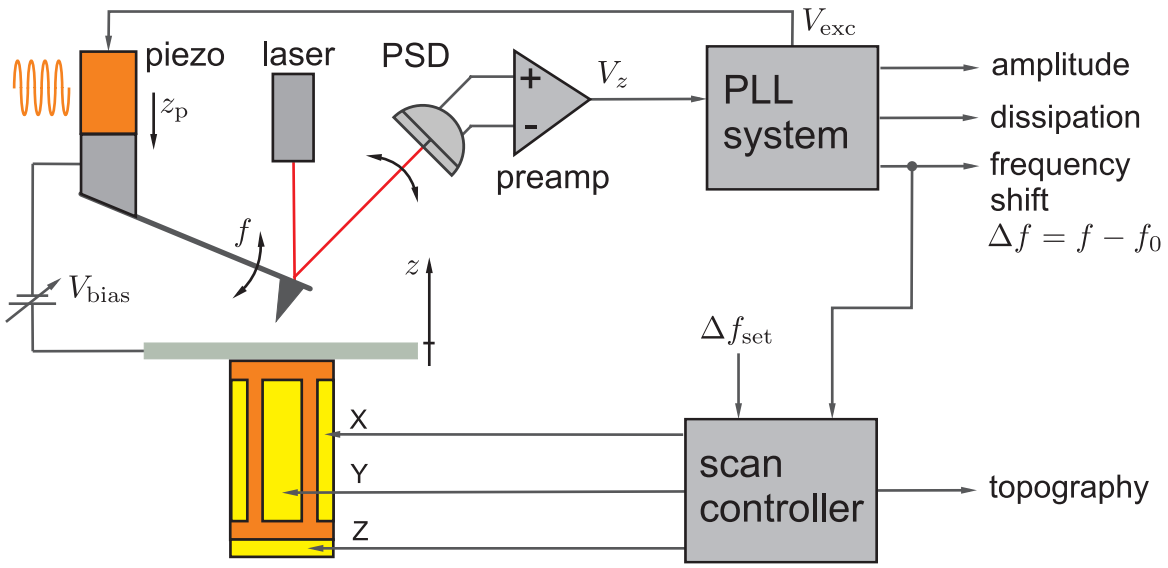

Figure 2.1: Schematic overview of NC-AFM operation in the frequency modulation mode.

NC-AFM measurements discussed here are performed with systems utilizing a silicon cantilever with a fundamental mode eigenfrequency f_0 and the OBD technique. The cantilever oscillation is controlled by a PLL system as described in Section 2.4. The sinusoidal voltage signal V_{exc} is applied to a piezo to excite the cantilever at its resonance frequency f. The cantilever oscillation is detected by a laser beam reflected from the back of the cantilever onto a position sensitive device (PSD). By a transimpedance preamplifier, the current signal from the PSD is converted into a voltage V_z being proportional to the displacement Δz of the cantilever. The sample movement relative to the tip position is typically realised by a piezoceramic tube being driven by a scan controller. Depending on the NC-AFM system,

the sample may be fixed while the tip is moved or vice-versa. Tip-sample interactions yield a shift of the resonance frequency $\Delta f = f - f_0$, which is detected by the PLL. During experiments, an appropriate bias voltage V_{bias} is applied between tip and sample to compensate for long-range electrostatic interactions.

For NC-AFM imaging, there are mainly two modes of operation: In the *constant height* mode, the frequency shift Δf is measured as a function of the lateral position of the tip scanning over the surface at a constant distance. The contrast in the frequency shift signal is based on position-dependent differences in the force between tip and sample.

In the *constant frequency-shift* mode, a distance control loop is employed, regulating the tip-sample distance to a value where a given set point Δf_{set} for the frequency shift is reached. In the idealised case, there would be no contrast in the Δf signal but the full height information in the topography signal.

Practically, measurements are performed somewhere in between the definitions of these two modes. A true *constant frequency-shift* mode is hardly possible as the distance control loop is typically too slow to immediately follow any fast change of the frequency shift. Therefore, some contrast will remain in the frequency shift image.

Measurements in the true *constant height* mode require the tilt of the sample to be compensated. Additionally true *constant height* imaging is extremely sensitive to thermal drift in z-direction, therefore, a drift compensation system is recommended. To circumvent these problems, the *quasi constant-height* mode can be used where the distance control loop is set so slow that it does not follow the local surface corrugation, but compensates sample tilt and thermal drift yielding a contrast in the frequency shift signal similar to true *constant height* measurements [29].

Apart from 2D imaging, 1D spectroscopy curves obtained by keeping the tip at a laterally fix position yield valuable information for one point on the surface:

In $\Delta f(V_{\mathrm{bias}})$ spectroscopy, the frequency shift Δf is recorded as a function of the bias voltage V_{bias}, which is swept over a chosen interval. A typical measurement is shown in Fig. 2.2a. The $\Delta f(V_{\mathrm{bias}})$ curve allows to determine the tip-sample contact potential difference V_{CPD}. Setting V_{bias} to the value of V_{CPD} yields long-range electrostatic tip-sample interactions to be minimised.

In $\Delta f(z)$ spectroscopy, the frequency shift Δf is recorded as a function of the tip-surface distance z controlled by the piezo displacement z_p. Figure 2.2b shows typical $\Delta f(z)$ curves recorded with different bias voltages illustrating the effect of long-range electrostatic interactions on the total tip-sample interaction. The black curve with $V_{\mathrm{bias}} = 1$ V shows the case of compensated V_{CPD}. The absolute tip-sample distance z is usually unknown, but may be obtained from suitable data analysis. The tip-sample force in units of Newton can be recovered from $\Delta f(z)$ curves with appropriate algorithms [26, 30, 31].

A combination of $\Delta f(z)$ spectroscopy with lateral repositioning of the tip can be used to determine three-dimensional force fields. Such measurements require a drift-free scan

environment and are typically performed either at low temperature [25, 32] or utilizing a drift-compensation technique for measurements at room temperature [14, 15].

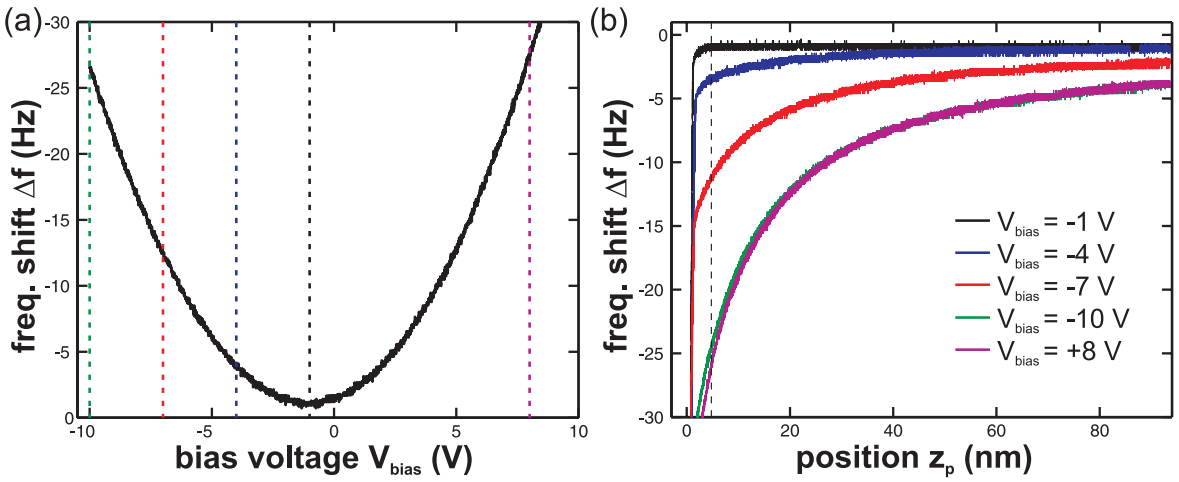

Figure 2.2: (a) Frequency shift Δf measured as a function of the tip-sample voltage V_{bias}. The tip-sample contact potential difference is $V_{\mathrm{CPD}} = -1.05$ V. Dashed lines are markers for the values of V_{bias} at which $\Delta f(z)$ curves shown in (b) are measured. (b) Frequency shift Δf measured as a function of the vertical piezo displacement z_p for different settings of V_{bias}. The dashed line indicates the position of the piezo where the $\Delta f(V_{\mathrm{bias}})$ curve from (a) is recorded. The measurements have been performed using cantilever AG 3 (PtIr coating) on a CaF_2(111) surface.

2.2 Force and frequency shift in NC-AFM

The total force F_{tot} between tip and sample in a typical UHV NC-AFM experiment consists mainly of the following contributions:

$$F_{\mathrm{tot}} = F_{\mathrm{vdW}} + F_{\mathrm{el}} + F_{\mathrm{chem}} \tag{2.1}$$

with long-range van-der-Waals forces F_{vdW} [33], long-range electrostatic forces F_{el} and the short-range chemical forces F_{chem} [10]. Other forces such as magnetic forces are not relevant within this work.

Interactions between two permanent dipoles (Keesom forces), a permanent dipole and an induced dipole (Debye forces) and two induced dipoles (London dispersion forces) are subsumed to the van-der-Waals forces [33–35]. While Keesom and Debye forces require permanent electrical dipoles and are relevant only in special cases, London dispersion forces

are omnipresent. At the macroscopic level, the London dispersion forces can be modelled as that of a pyramidal tip of infinite height and a flat sample surface yielding

$$F_{\mathrm{vdW}}(z) = -A_H \frac{4\tan^2(\beta/2)}{6\pi}\frac{1}{z} \tag{2.2}$$

with β being the full tip angle and A_H being the Hamaker constant, which depends on the tip and sample materials and is typically of the order of 1 eV [33].

A potential difference V between tip and sample yields an electrostatic force

$$F_{\mathrm{el}}(z) = -\frac{1}{2}V^2\frac{dC(z)}{dz} = -\frac{1}{2}(V_{\mathrm{CPD}} - V_{\mathrm{bias}})^2\frac{dC(z)}{dz} \tag{2.3}$$

with dC/dz as the gradient of the capacitance between tip and sample surface [36]. The contact potential difference can be caused by different work functions of tip and sample or by localised charges on the sample surface typically remaining after in-situ cleavage of insulators. The bias voltage V_{bias} is typically set to a value where the contact potential and, therefore, the electrostatic force is minimized. For spatial resolution of localized charges or work function differences, the Kelvin-probe technique (KPFM) can be employed [37].

At a tip-sample distance z in the order of interatomic spacings, the van-der-Waals force between the macroscopic tip and the sample becomes negligible compared to the van-der-Waals force between the topmost tip atom and the nearest sample atom. Additionally, short-range repulsive forces between these two atoms occur due to the Pauli exclusion principle. Such a situation is usually approximated by a Lennard-Jones potential

$$V_{\mathrm{LJ}}(z) = -E_{\mathrm{bond}}\left[2\left(\frac{z_0}{z}\right)^6 - \left(\frac{z_0}{z}\right)^{12}\right] \tag{2.4}$$

with bond energy E_{bond} and equilibrium distance z_0 [33, 38, 39]. $V_{\mathrm{LJ}}(z)$ has an attractive term $\propto z^{-6}$ modeling the atom-atom van-der-Waals interaction and a repulsive term $\propto z^{-12}$ [33]. Depending on the bond type, many different potentials have been described in literature [40–42].

The tip-sample force $F_{\mathrm{LJ}}(z)$ is obtained from a derivation of the tip-sample potential:

$$F_{\mathrm{LJ}}(z) = -\frac{\partial V_{\mathrm{ts}}}{\partial z} = -12\frac{E_{\mathrm{bond}}}{z_0}\left[\left(\frac{z_0}{z}\right)^7 - \left(\frac{z_0}{z}\right)^{13}\right] \quad . \tag{2.5}$$

A further derivation yields the force gradient $k_{\mathrm{LJ}}(z)$, which has the unit of a spring constant:

$$k_{\mathrm{LJ}}(z) = -\frac{\partial F_{\mathrm{ts}}}{\partial z} = -\frac{E_{\mathrm{bond}}}{z_0^2}\left[84\left(\frac{z_0}{z}\right)^8 - 156\left(\frac{z_0}{z}\right)^{14}\right] \quad . \tag{2.6}$$

As an example potential, the Lennard-Jones potential is calculated for the interaction between two silicon atoms with $E_{\mathrm{bond}} = 2.315$ eV and $z_0 = 0.235$ nm [39]. This potential is used as a generic curve representing general tip-surface interaction parameters V_{ts}, F_{ts} and k_{ts} for the remaining parts of this chapter. The tip-sample potential as well as its first two derivatives, force F_{ts} and force gradient k_{ts}, are shown in Fig. 2.3. The minimum of the potential is at $V_{\mathrm{ts}}(z_0)$ where the force $F_{\mathrm{ts}}(z)$ changes from the repulsive regime for $z < z_0$ to the attractive regime for $z > z_0$.

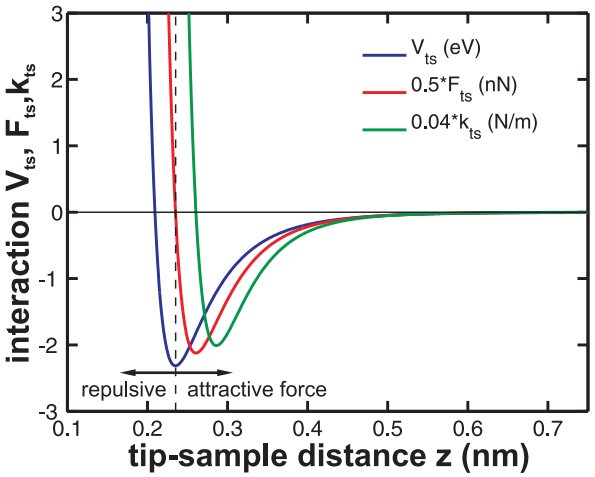

Figure 2.3: Lennard-Jones model potential V_{ts} and its first two derivatives, force F_{ts} and force gradient k_{ts}, for the interaction between two silicon atoms. The dashed line indicates the transition between attractive and repulsive tip-sample forces. The curves for F_{ts} and k_{ts} are scaled in vertical direction for better display (see legend for scaling factors).

Depending on the tip and surface chemical nature additional forces, commonly referred to as chemical forces, appear. Chemical forces consist of several short-range contributions that may include covalent bonding and ionic bonding. They are most important for atomic resolution force imaging and spectroscopy but not relevant in the context of this work.

2.2.1 Frequency shift from tip-sample interaction

Brought close to the sample, the cantilever can be described as a weakly disturbed harmonic oscillator where its resonance frequency changes from the eigenfrequency f_0 to $f = f_0 + \Delta f$ due to the force gradient k_{ts} between tip and sample. Assuming the force gradient to be constant in z-direction during the full cantilever oscillation cycle, the frequency shift can be calculated as [4]

$$\Delta f(z, f_0, k) = \frac{f_0}{2k} k_{\mathrm{ts}} \quad , \tag{2.7}$$

which is valid for amplitudes A being small compared to the range of the tip-sample interaction force [39]. For larger amplitudes, the frequency shift is calculated as

$$\Delta f(z, f_0, k, A) = \frac{f_0}{2k} \frac{2}{\pi A^2} \int_{-A}^{A} k_{\mathrm{ts}}(z + A - q) \sqrt{A^2 - q^2}\, dq \tag{2.8}$$

where the constant force gradient k_{ts} of Eq. (2.7) is replaced by a weighted average of k_{ts} [31]. The distance z here denotes the position of the tip at the lower turning point of the oscillation cycle. Equation (2.8) can also be written as a function of the tip-sample force F_{ts}

$$\Delta f(z, f_0, k, A) = -\frac{f_0}{2k}\frac{2}{\pi A^2}\int_{-A}^{A}\frac{F_{\mathrm{ts}}(z+A-q)q}{\sqrt{A^2-q^2}}dq \quad . \tag{2.9}$$

In Fig. 2.4, the frequency shift is calculated using Eqs. (2.7) and (2.8) for different oscillation amplitudes A. A comparison of the magenta curve for $A = 10$ pm calculated using Eq. (2.8) and the black curve calculated using Eq. (2.7) gives an impression of the amplitude range where the small-amplitude approximation of Eq. (2.7) is valid. For larger amplitudes, the magnitude of the frequency shift is strongly decreased. The zero crossing as well as the minimum of the $\Delta f(z)$ curve is shifted towards smaller tip-sample distance z for larger amplitudes. Therefore, it is for an arbitrary amplitude usually not possible to determine from the sign of Δf whether the lower turning point of the cantilever oscillation is in the attractive or the repulsive force regime [43].

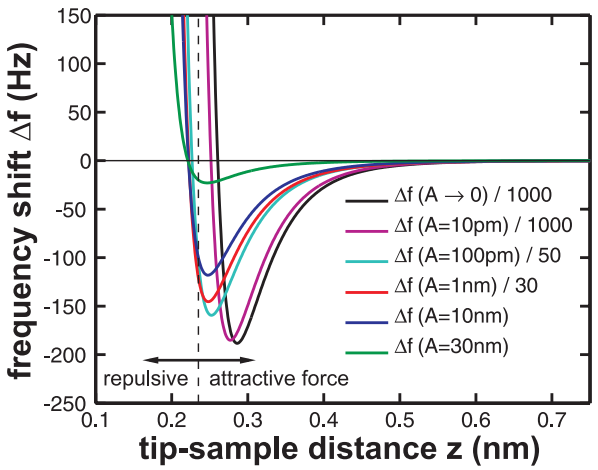

Figure 2.4: Calculated frequency shift Δf versus tip-sample distance z for different cantilever oscillation amplitudes A using Eq. (2.8) and typical cantilever properties $f_0 = 300$ kHz and $k = 40$ N/m. The black curve is calculated using Eq. (2.7), which is valid for amplitudes being small compared to the range of the tip-sample interaction force. Some curves are scaled in vertical direction for better display (see legend for scaling factors).

2.2.2 Normalised frequency shift

The measured frequency shift $\Delta f(z, f_0, k, A)$ depends not only on the potential acting between tip and sample, but also on several experimental parameters and cantilever properties. This complicates the comparison of data obtained under different experimental conditions. To circumvent this problem, Giessibl introduced the normalised frequency shift γ [39] as:

$$\gamma(z, A) = \frac{kA^{3/2}}{f_0}\Delta f(z, f_0, k, A) \quad . \tag{2.10}$$

Using this normalised frequency shift, Eq. (2.8) can be simplified to an expression without f_0 and k:

$$\gamma(z, A) = \frac{1}{\pi\sqrt{A}} \int_{-A}^{A} k_{\mathrm{ts}}(z + A - q)\sqrt{A^2 - q^2}dq \quad . \tag{2.11}$$

In Fig. 2.5, the normalised frequency shift is shown in dependence on the tip-sample distance for different oscillation amplitudes. This illustrates that the normalisation works well for amplitudes larger than the interaction length yielding coincident curves, while it fails for amplitudes being smaller than the interaction length of the tip-sample potential.

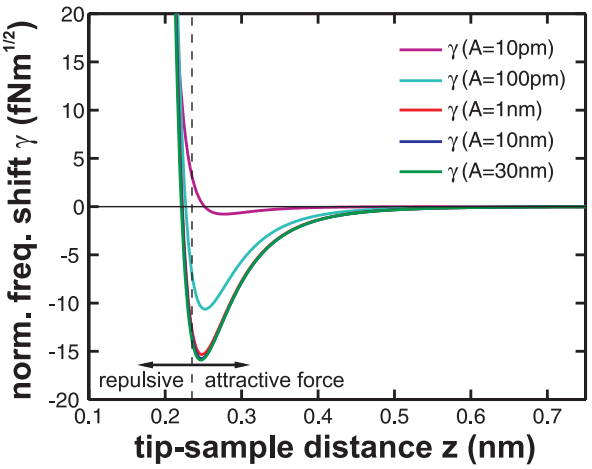

Figure 2.5: Calculated normalised frequency shift γ versus tip-sample distance z for different cantilever oscillation amplitudes A using Eq. (2.11) and a Lennard-Jones potential for Si-Si.

2.2.3 Force from frequency shift

There are mainly two approaches, to recover the force F_{ts} from a measured $\Delta f(z)$ curve:

1. A model potential for the tip-sample interaction is assumed for the oscillation model of Eq. (2.8) and fitted to the experimental data of the frequency shift [44].
2. A force deconvolution algorithm is applied allowing to extract force information from the $\Delta f(z)$ curve without any knowledge of the nature of the force contributions. Two variants of the deconvolution approach have been implemented and are now widely used, namely the matrix method based on an inversion of Eq. (2.9) developed by Giessibl [31] and the analytical force-deconvolution method developed by Sader and Jarvis [30].

For applying the Sader-Jarvis algorithm, the following expression to recover the force $F_{\mathrm{ts}}(z)$ from the frequency shift $\Delta f(z)$ is used:

$$F_{\mathrm{ts}}(z) = \frac{2k}{f_0} \int_{z}^{\infty} \left[\left(1 + \frac{\sqrt{A}}{8\sqrt{\pi(t-z)}} \right) \Delta f(t) - \frac{A^{3/2}}{\sqrt{2(t-z)}} \frac{d\Delta f(t)}{dt} \right] dt \quad . \tag{2.12}$$

For the following model calculations, a numerical implementation of Eq. (2.12) given in the supplemental material of [26] will be used. This implementation includes correction terms [45] to circumvent the divergence of the integrand in Eq. (2.12) for $t = z$.

For applying the matrix method, Eq. (2.9) is expressed as a matrix equation for discrete values [26]:

$$\Delta f_i = \sum_{j=1}^{N} W_{ij} F_{\mathrm{ts},j} \quad . \tag{2.13}$$

After determination of all matrix elements W_{ij}, the inverse matrix $\mathbf{M} = \mathbf{W}^{-1}$ can be used to calculate the force for a given frequency shift curve

$$F_{\mathrm{ts},j} = \sum_{i=1}^{N} M_{ji} \Delta f_i \quad . \tag{2.14}$$

In contrast to the Sader-Jarvis algorithm, the matrix method requires data points $\Delta f_i = \Delta f(z_i)$ with equidistant spacing along the z-axis [26].

2.2.3.1 Force deconvolution from model data

To compare both methods regarding their operation range and reliability, simulations with artificial $\Delta f(z)$ curves are performed as schematically depicted in Fig. 2.6. The reference for all following calculations is the tip-sample force $F_{\mathrm{ts}}(z)$ calculated for a Lennard-Jones potential as shown in Fig. 2.3.

In Fig. 2.7a, the force F_{ts} (dash-dotted) calculated from a Lennard-Jones potential is compared to the force $F_{\mathrm{S}}^{\Delta f}$ (solid lines) extracted from the frequency shift $\Delta f(z)$ using the Sader-Jarvis algorithm for different cantilever oscillation amplitudes A. The same calculation performed using the matrix method is shown in Fig. 2.8a. In principle, all deconvoluted curves agree well with the tip-sample force derived from the Lennard-Jones potential. Only for the Sader-Jarvis algorithm, an overestimation of the force for an amplitude of $A = 10$ pm as well as an underestimate for $A = 100$ pm occurs.

To illustrate the difference between F_{ts} and the deconvoluted force, the residuals

$$\Delta F_{\mathrm{S/M}}^{\Delta f} = F_{\mathrm{S/M}}^{\Delta f} - F_{\mathrm{ts}} \tag{2.15}$$

are plotted for different amplitudes in Fig. 2.7b and Fig. 2.8b for the Sader-Jarvis algorithm and the matrix method, respectively. To quantify these deviations, the shift ΔF_{min} of the minimum force

$$\Delta F_{\mathrm{min}} = \min(F_{\mathrm{ts}}^{\Delta f}) - \min(F_{\mathrm{ts}}) \tag{2.16}$$

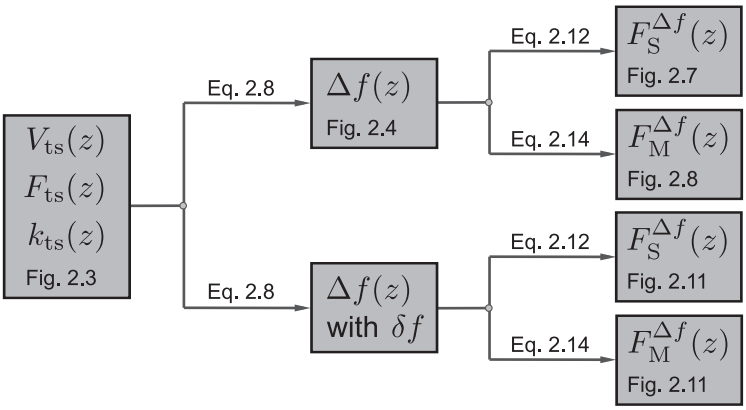

Figure 2.6: Scheme for performing model calculations for the deconvolution of (noisy) $\Delta f(z)$ data. The $\Delta f(z)$ curves are calculated using Eq. (2.8) from the force gradient $k_{ts}(z)$ of the model Lennard-Jones potential for different cantilever oscillation amplitudes. The forces $F_S^{\Delta f}(z)$ and $F_M^{\Delta f}(z)$ are extracted from the $\Delta f(z)$ curves using the Sader-Jarvis algorithm and the matrix method with results compiled in Figs. 2.7 and 2.8, respectively. For a quantification of accuracy, results $F_S^{\Delta f}(z)$ and $F_M^{\Delta f}(z)$ are compared to the previously calculated $F_{ts}(z)$. To study the effect of noise on the deconvolution methods, the $\Delta f(z)$ curves are superimposed with random numbers corresponding to a frequency shift noise with an RMS value of $\delta f = 10$ Hz. The latter results are compiled in Fig. 2.11.

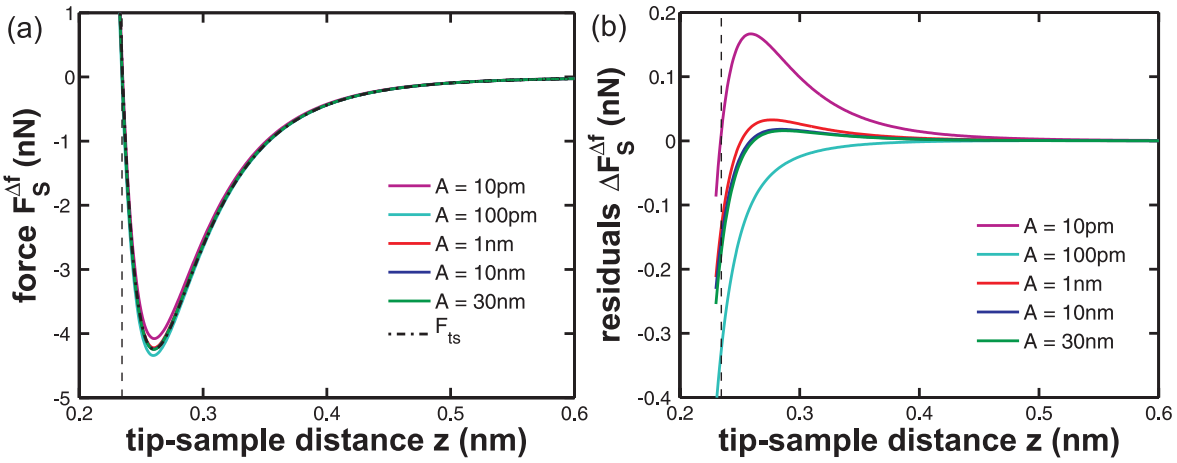

Figure 2.7: (a) Tip-sample force F_{ts} calculated from the Lennard-Jones potential (dash-dotted curve) compared to the force $F_S^{\Delta f}$ deconvoluted from $\Delta f(z)$ using the Sader-Jarvis algorithm for different cantilever oscillation amplitudes A (solid coloured curves, compare to Fig. 2.4). (b) Residuals $\Delta F_S^{\Delta f}$ from force deconvolution using the Sader-Jarvis algorithm. The dashed line represents the transition between attractive and repulsive tip-sample forces F_{ts}.

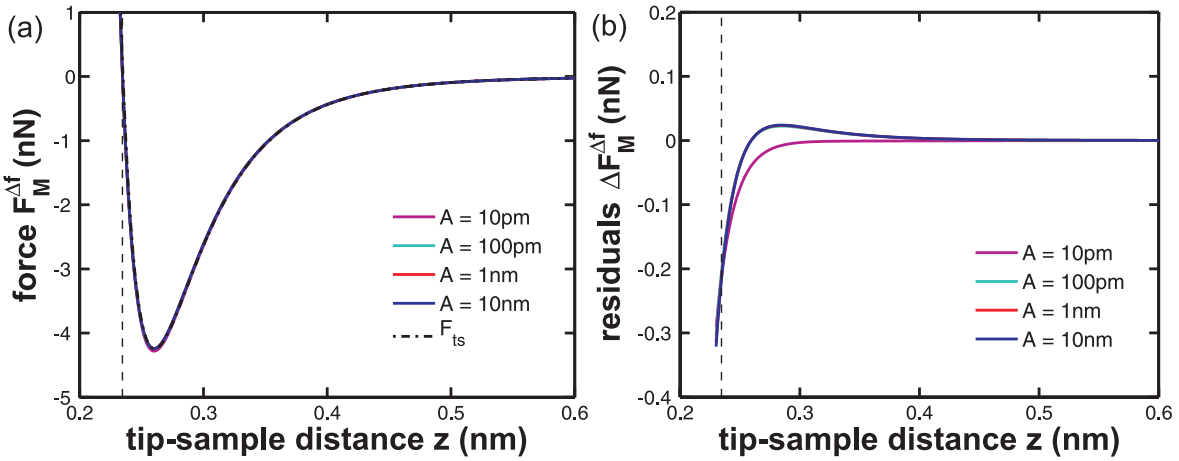

Figure 2.8: (a) Tip-sample force F_{ts} calculated from the Lennard-Jones potential (dash-dotted curve) compared to the force $F_{\mathrm{M}}^{\Delta f}$ deconvoluted from the frequency shift Δf using the matrix method for different cantilever oscillation amplitudes A (solid coloured curves, compare to Fig. 2.4). (b) Residuals $\Delta F_{\mathrm{M}}^{\Delta f}$ from force deconvolution using the matrix method. The dashed line represents the transition between attractive and repulsive tip-sample forces F_{ts}.

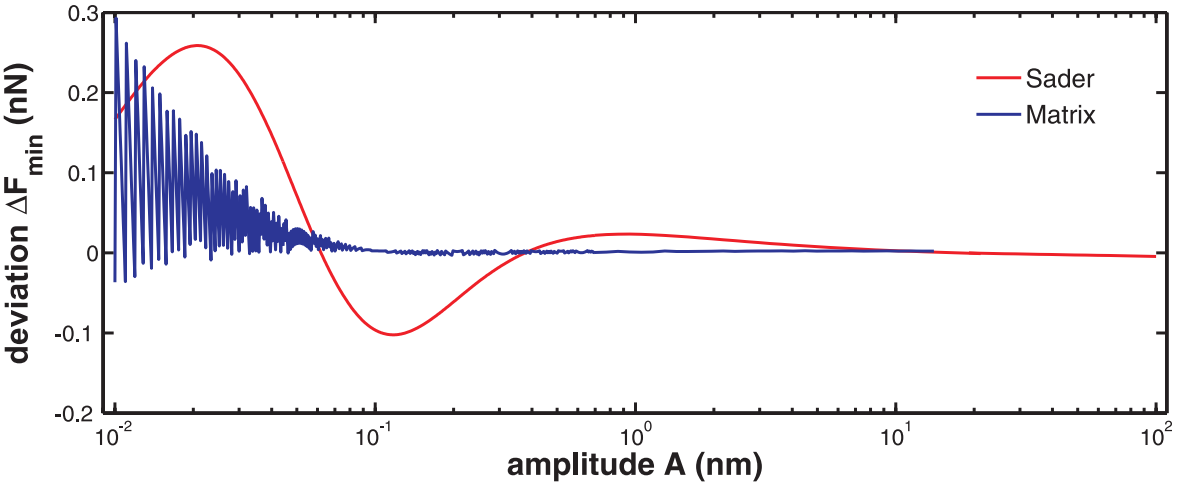

Figure 2.9: Deviation ΔF_{min} of the minimum of the deconvoluted force curve in dependence on the cantilever oscillation amplitude.

is determined as a function of the amplitude A (see Fig. 2.9).

The maximum of $\Delta F_{\min}$ at $A = 21$ pm and the minimum of $\Delta F_{\min}$ at $A = 120$ pm by using the Sader-Jarvis algorithm as well as the fluctuations for small amplitudes by using the matrix method are discussed by Welker *et al.* in [26]. As these amplitudes are below the working range of the cantilevers used in this thesis, the focus is set on larger amplitudes. For silicon cantilever based AFM systems as used in this work, typical amplitudes are between 0.5 nm and 50 nm depending on the cantilever type as discussed in the following section. Therefore, the relative error in $F_{\min}$ does not exceed 0.6% at the local maximum around $A = 1$ nm for the Sader-Jarvis algorithm. With less than 0.1%, this error is even lower for the matrix method as well as for the Sader-Jarvis algorithm for larger amplitudes. For all these calculations, the z-axis was divided into sections of 1 pm length. The shift $\Delta z_{\min}$ of the position of the force minimum does not exceed ± 1 pm for both deconvolution methods at all amplitudes investigated here, yielding a relative error smaller than 0.4%. The shift of the zero crossing of $F_{\mathrm{ts}}^{\Delta f}$ compared to F_{ts} is not shown here but akin to the shift of the force minimum. All deconvolution calculations are performed with simulated $\Delta f(z)$ curves covering a z range, which is at least three times larger than the oscillation amplitude, e.g. up to $z = 300$ nm for $A = 100$ nm. The matrix method can be performed with an acceptable speed as long as the matrix fits in the working memory of the computer. Therefore, these calculation were performed up to a matrix size of 43×43 nm with 1 pm resolution, which requires 13.8 GB of working memory for double precision numbers, allowing to calculate the deconvolution up to amplitudes of $A = 14$ nm.

To quantify the quality of the force deconvolution, the coefficient of determination (CoD) is calculated

$$R^2 = 1 - \frac{\sum_{i=1}^{N} (F_{\mathrm{S/M},i}^{\Delta f} - F_{\mathrm{ts},i})^2}{\sum_{i=1}^{N} (F_{\mathrm{S/M},i}^{\Delta f} - \overline{F_{\mathrm{S/M}}})^2} \tag{2.17}$$

where a value of $R^2 = 1$ corresponds to a perfect fit [46]. The CoD is calculated in dependence on the amplitude for both the Sader-Jarvis algorithm and the matrix method. Results are shown in Fig. 2.10. In conclusion, both methods can principally be used for the deconvolution of data obtained with oscillation amplitudes down to 100 pm. The matrix method yields highly accurate results over the entire range of amplitudes down to 100 pm while the Sader-Jarvis algorithm yields somewhat less precise results in the range of 100 pm to 1 nm. For amplitudes below 10 pm, a simple analysis according to Eq. (2.7) can be expected to yield precise results. Hence, it is the amplitude region of 10 to 100 pm that requires further attention for the development of precise deconvolution procedures. The Sader-Jarvis algorithm yields a slightly better CoD and is easy applied to large datasets where the matrix method is limited by the size of the working memory. Another advantage of the Sader-Jarvis algorithm is the fact that it does not require equidistant data points like the matrix method. Therefore, high-precision measurements can be performed close to the sample while the long-range components of the frequency shift are recorded with less point resolution.

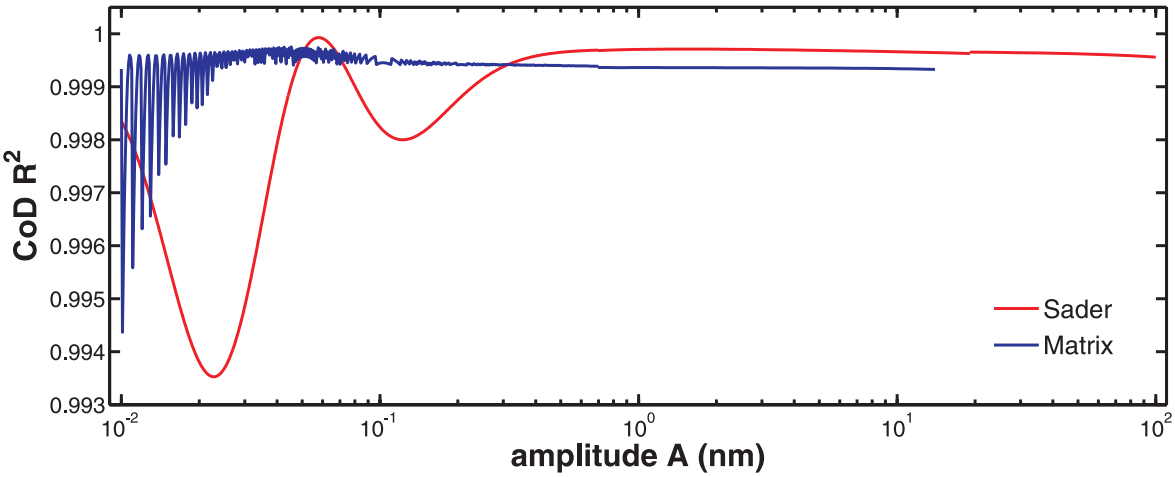

Figure 2.10: Coefficient of determination R^2 in dependence on the oscillation amplitude. The CoD was calculated for $F^{\Delta f}$ up to $z = 5$ nm for all simulated amplitudes. The curves show that the deconvolution quality is excellent with $R^2 > 0.999$ except for the already mentioned problems at amplitudes smaller than 0.25 nm.

2.2.3.2 Force deconvolution from experimental data

In the previous section, the force deconvolution quality was investigated for a perfect model environment without any external disturbances. As real NC-AFM measurements are always overlaid by noise depending on several environmental, instrumental and cantilever parameters (see Chapter 6), the following simulation incorporates a typical frequency shift noise level. For this simulation, a $\Delta f(z)$ curve calculated for an amplitude $A = 1$ nm is overlaid with random numbers normalised to an RMS noise amplitude $\delta f = 10$ Hz. This value is reasonable if the AFM tip in close proximity to the sample. The deconvolution is performed using both methods on segments of the $\Delta f(z)$ curve for different ranges of the z-axis spanning a range from 0.23 nm to $z_{\max}$. During the calculation, $z_{\max}$ is varied between 5 nm and 43 nm. As illustrated in Fig. 2.11a, the noise levels found in the force curves extracted from the short $\Delta f(z)$ segment ($z_{\max} = 5$ nm) are nearly identical for the Sader-Jarvis algorithm and the matrix method. In contrast, Fig. 2.11b shows a strong increase of noise for the force $F_{\mathrm{M}}^{\Delta f}$ extracted from a larger segment by the matrix method ($z_{\max} = 43$ nm), while the noise level of $F_{\mathrm{S}}^{\Delta f}$ extracted by the Sader-Jarvis algorithm appears to be unaffected by the length of the $\Delta f(z)$ curve segment. To quantify this, the CoD for this simulation is shown in dependence on $z_{\max}$ in Fig. 2.12, where the value for the Sader-Jarvis algorithm remains nearly constant at $R^2 = 0.96$. This value is very good, but but not as perfect as for the undisturbed curves in the previous section. On the other hand, the R^2 for the matrix method strongly decreases as a function of $z_{\max}$.

Finally, a typical experimental Δf versus distance curve is shown in Fig. 2.13a. It has been measured on system C described in Section 2.6.3, using a silicon cantilever with $f_0 = 363484.6$ Hz and $k = 66$ N/m on a $CaF_2(111)$ surface. The extracted tip-sample force $F_{\mathrm{S}}^{\Delta f}$ shown in Fig. 2.13b is calculated using the Sader-Jarvis algorithm. The z-

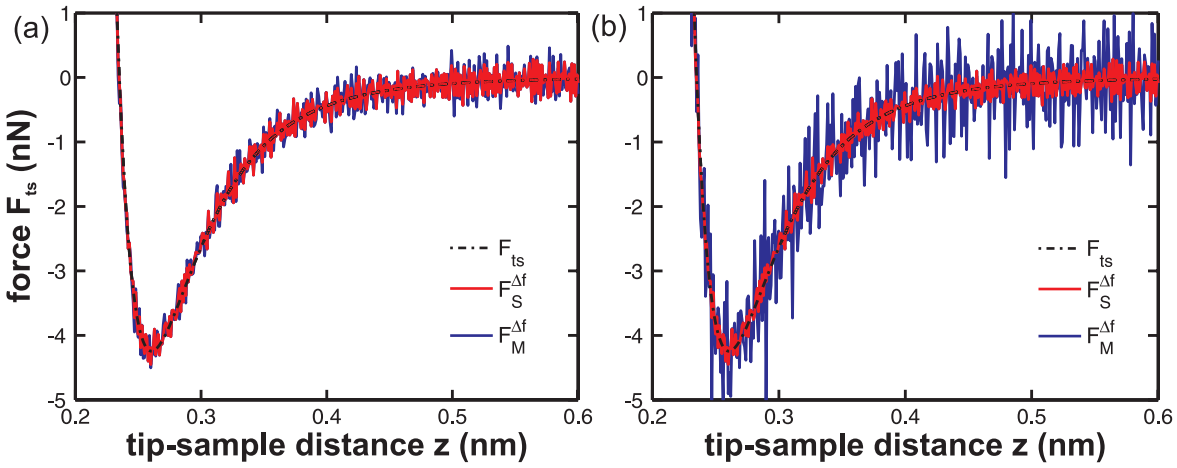

Figure 2.11: Simulation: Tip-sample force F_{ts} calculated from the Lennard-Jones potential (dash-dotted curve) compared to the force $F_{\mathrm{S}}^{\Delta f}$ (red curve) as well as $F_{\mathrm{M}}^{\Delta f}$ (blue curve) extracted from the noisy $\Delta f(z)$ curve using the Sader-Jarvis algorithm and the matrix method, respectively. (a) Force deconvolution on a $\Delta f(z)$ curve segment limited by $z_{\max} = 5$ nm. (b) Force deconvolution on a $\Delta f(z)$ curve segment limited by $z_{\max} = 43$ nm.

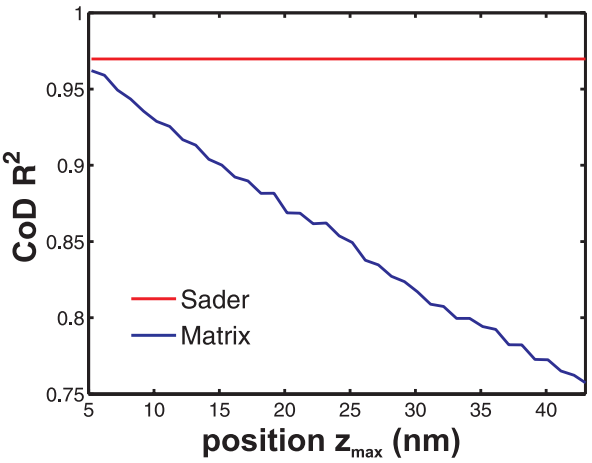

Figure 2.12: Coefficient of determination for the force deconvolution using the Sader-Jarvis algorithm as well as the matrix method on simulated noisy $\Delta f(z)$ curves as a function of $z_{\max}$ as the upper boundary of the deconvolution segment on the $\Delta f(z)$ curve.

axis includes an unknown offset regarding the true tip-sample distance as only the relative position z_p of the z-piezo is known; this does, however, not affect the deconvolution. This result illustrates a strong reduction of the signal-to-noise ratio of a deconvoluted force curve compared to the measured $\Delta f(z)$ curve. Therefore, lowest possible frequency shift noise is required to extract accurate force curves from measured data.

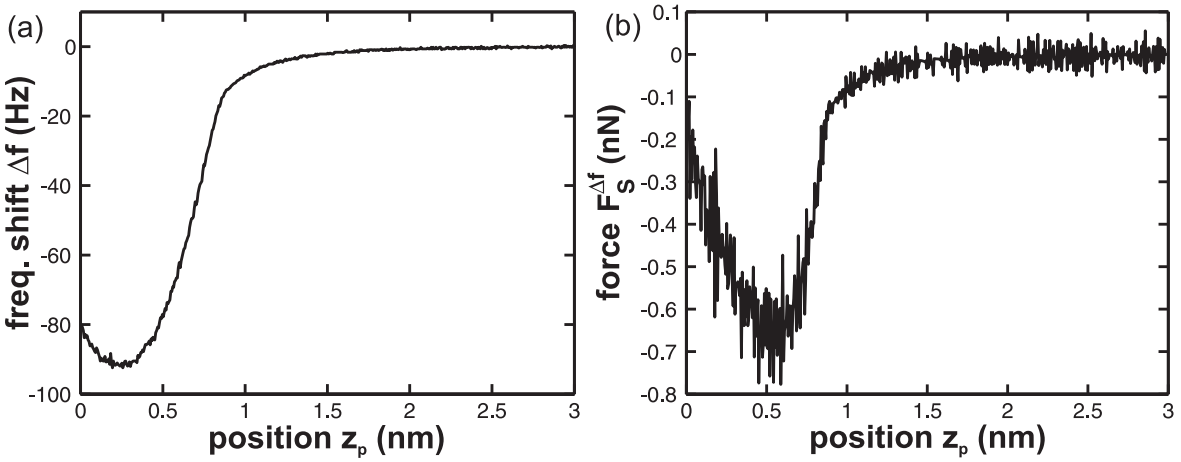

Figure 2.13: Measured $\Delta f(z)$ curve and its deconvolution to a force. (a) Measured $\Delta f(z)$ curve (cantilever $f_0 = 363484.6$ Hz, $k = 66$ N/m and $A = 5.2$ nm) obtained on $CaF_2(111)$ with compensated contact potential ($V_{bias} = -4.9$ V). z_p is the relative piezo position and not the absolute tip-sample distance z. (b) Force $F_\mathrm{S}^{\Delta f}$ extracted from (a) using the Sader-Jarvis algorithm.

In conclusion, both methods yield a high deconvolution quality for the parameters chosen here using amplitudes larger than 0.5 nm and assuming a noise-free $\Delta f(z)$ curve. However, the application of the matrix method is more limited by the size of datasets that can be handled by the data processing equipment. This is unfavourable especially for situations where large datasets are required, e.g. for large amplitude operation or investigations of short-range and long-range interactions at the same time. These datasets usually require high resolution in z. Considering noisy $\Delta f(z)$ curves, the deconvolution quality of the matrix method dramatically decreases for large datasets while the Sader-Jarvis algorithm is unaffected concerning this matter. Therefore, the Sader-Jarvis algorithm is preferable for large amplitude cantilever operation and especially for the investigation of long-range and short-range forces at the same time.

2.3 NC-AFM cantilevers

Most cantilevers used as force sensors for NC-AFM are produced by using silicon microstructure fabrication technology allowing the parallel production of a large number of cantilevers on a silicon wafer, all with well-defined mechanical properties. The entire force sensor is etched out of a silicon wafer with the tip pointing in a [001] crystal direction [47]. The sensor consists of the cantilever itself, an integrated tip at the free end and an attached handling piece called support chip. Figure 2.14 shows two scanning electron microscopy (SEM) micrographs of a typical cantilever. Although, the cantilevers usually have a trapezoidal cross-section, a simple model of a clamped rectangular beam with respective coordinate system as shown in Fig. 2.15 can be used for theoretical modelling with good accuracy [48]. High-resolution NC-AFM imaging requires cantilevers with sharp tips and suitable oscillation properties. These are eigenfrequency, stiffness and Q-factor, which will be introduced in the following.

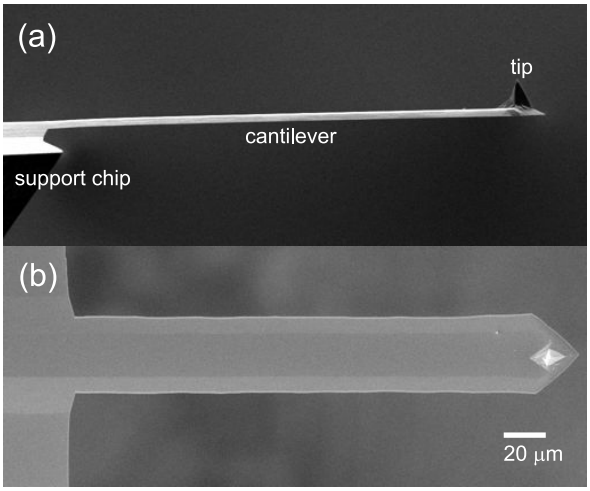

Figure 2.14: SEM micrographs of a cantilever and tip etched from mono-crystalline silicon in side view (a) and bottom view (b). The cantilever was manufactured by Nanoworld (Neuchâtel, Switzerland). SEM micrographs obtained by Bernd Walkenfort.

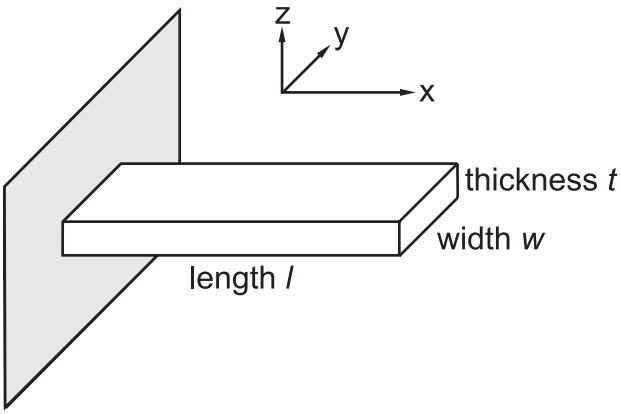

Figure 2.15: Schematic of a rectangular cantilever clamped at $x = 0$.

2.3.1 Oscillation modes

The equation of motion of a beam as characterised in Fig. 2.15 is given by

$$\rho\Gamma\frac{d^2u(x,\tau)}{d^2\tau} + EI\frac{d^4u(x,\tau)}{d^4x} = \widetilde{F} \tag{2.18}$$

with $u(x,\tau)$ as the displacement of the cantilever from its equilibrium position as a function of time τ, ρ and E as density and Young's modulus of its material, Γ as its cross section, I as its moment of inertia and $\widetilde{F}$ as an external force per unit length [49]. For a rectangular cantilever, cross-section and moment of inertia are given as

$$\Gamma = wt \quad \text{and} \quad I = \frac{wt^3}{12} \quad . \tag{2.19}$$

For a cantilever fixed at one end and being free at the other end, the following boundary conditions are applied [50]:

$$\begin{aligned} u(0,\tau) &= 0 \qquad & \frac{du(0,\tau)}{dx} &= 0 \\ \frac{d^2u(l,\tau)}{d^2x} &= 0 \qquad & \frac{d^3u(l,\tau)}{d^3x} &= 0 \end{aligned} \tag{2.20}$$

The fixation of inclination and amplitude of the cantilever at $x = 0$ is described by the first two conditions. At the free end $x = l$, the torque $M(x) \propto d^2u(x,\tau)/dx^2$ of the cantilever vanishes. The external force $F = dM/dx \propto d^3u(x,\tau)/dx^3$ is zero at the end of the cantilever, which is described by the fourth condition and only valid for the idealised case of a cantilever without an additional tip mass.

The solution for Eq. (2.18) is given by a sum over all vibration modes as:

$$u(x,\tau) = \sum_{n=0}^{\infty} \frac{A_n}{2}\sin(\omega_n\tau + \phi_n)\Phi_n(x) \tag{2.21}$$

where each summand consists of a time-dependent function and a function $\Phi_n(x)$, depending only on the position x along the cantilever [50]. The parameters A_n, ω_n and ϕ_n are the amplitude, the angular vibration frequency and the phase shift of the nth vibration mode, respectively. The x-position dependent part is given by [50, 51]

$$\begin{aligned} \Phi_n(x) = \Phi(x,\alpha_n) = &\cos\left(\frac{\alpha_n}{l}x\right) - \cosh\left(\frac{\alpha_n}{l}x\right) \\ &- \frac{\cos(\alpha_n)+\cosh(\alpha_n)}{\sin(\alpha_n)+\sinh(\alpha_n)}\left[\sin\left(\frac{\alpha_n}{l}x\right) - \sinh\left(\frac{\alpha_n}{l}x\right)\right] \end{aligned} \tag{2.22}$$

where the wavelength of the nth vibration mode l/α_n is related to the angular vibration frequency by

$$\alpha_n^4 = \frac{\Gamma \rho \omega_n^2 l^4}{EI} \quad . \tag{2.23}$$

Using the boundary conditions from Eq. (2.20) for the cantilever with the free end without an external force, the values for α_n need to fulfill the equation [50]

$$\cos(\alpha_n) + 1/\cosh(\alpha_n) = 0 \quad . \tag{2.24}$$

This yields

$$\begin{aligned} \alpha_0 &= 1.8751 & \alpha_1 &= 4.6941 \\ \alpha_2 &= 7.8548 & \alpha_3 &= 10.9955 \\ \alpha_n &= (n + 1/2)\pi & \text{for } n &\geq 4 \quad . \end{aligned} \tag{2.25}$$

The shape of the first four oscillation modes of a cantilever without an additional tip mass are shown in Fig. 2.16.

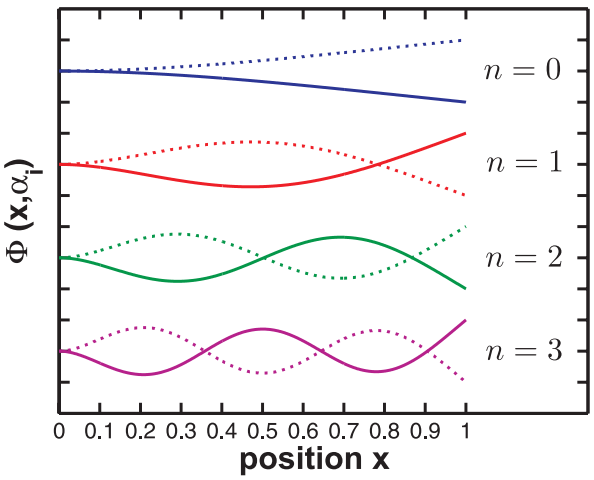

Figure 2.16: Shape of the first four vibration modes of a cantilever of length $l = 1$ with a free end without an additional tip mass.

Using Eq. (2.23) and with the static stiffness of a cantilever given as

$$k = \frac{3EI}{l^3} \quad , \tag{2.26}$$

the resonance frequencies f_n of the oscillation modes can be calculated as

$$f_n = \frac{\omega_n}{2\pi} = \frac{\alpha_n^2}{2\pi l^2}\sqrt{\frac{EI}{\Gamma\rho}} = \frac{1}{2\pi}\sqrt{\frac{k}{m_{\text{eff}}}} \tag{2.27}$$

with

$$m_{\text{eff}} = \frac{3l\Gamma\rho}{\alpha_n^4} \tag{2.28}$$

as the effective mass differing by a factor of $3/\alpha_n^4$ from the actual mass of the cantilever beam $m_{\text{beam}} = l\Gamma\rho$ [52]. For the lowest resonance frequency of a rectangular cantilever beam without an additional tip mass, this simplifies to

$$f_0 = \frac{\omega_0}{2\pi} = 0.162\frac{t}{l^2}\sqrt{\frac{E}{\rho}} \quad . \tag{2.29}$$

If the cantilever is equipped with a tip having a non-negligible mass, the fourth boundary condition of Eq. (2.20) changes to

$$\frac{d^3u(l,\tau)}{d^3x} = \frac{m_{\text{tip}}}{EI}\frac{d^2\tau u(l,\tau)}{d^2\tau} \tag{2.30}$$

where m_{tip} is assumed to be a point mass at the end of the cantilever beam [49]. The equation of motion stays the same but instead of Eq. (2.24) the following equation has to be used to determine the values α_n [49]

$$\cos\alpha_n + 1/\cosh\alpha_n + \mu\alpha_n(\tanh\alpha_n\cos\alpha_n - \sin\alpha_n) = 0 \tag{2.31}$$

with the mass ratio

$$\mu = \frac{m_{\text{tip}}}{m_{\text{beam}}} = \frac{m_{\text{tip}}}{l\Gamma\rho} \quad . \tag{2.32}$$

For a typical mass ratio $\mu = 0.1$, the value of α_0 is decreased to 1.7227 yielding for the resonance frequency

$$f_0^{m_{\text{tip}}} = 0.136\frac{t}{l^2}\sqrt{\frac{E}{\rho}} \quad . \tag{2.33}$$

This would rise an error of 20% if the tip mass is not considered to calculate the resonance frequency of the cantilever from its dimensions. Using Eq. (2.27), the resonance frequencies of the higher oscillation modes can be calculated as

$$f_n = \frac{f_0\alpha_n^2}{\alpha_0^2} \tag{2.34}$$

	mass ratio μ				
frequency ratio	0	0.01	0.05	0.1	-0.1
f_1/f_0	6.27	6.27	6.35	6.52	6.98
f_2/f_0	17.55	17.57	17.94	18.71	19.41
f_3/f_0	34.39	34.45	35.43	37.30	36.23
f_4/f_0	56.84	56.97	58.93	62.45	57.27

Table 2.1: Ratios of the eigenfrequency f_n of higher harmonics of a rectangular cantilever beam with a tip to the eigenfrequency f_0 of its fundamental mode for different mass ratios.

where the ratios between the higher harmonic eigenfrequencies f_n to the fundamental eigenfrequency f_0 in dependence on the mass ratio μ are given in Table 2.1. Negative tip masses can be used to model picket-shaped cantilevers with the formalism developed for rectangular cantilevers [53].

The modal stiffness for the nth eigenmode of a rectangular cantilever without an additional tip mass is given by

$$k_n = k\frac{\alpha_n^4}{12} \tag{2.35}$$

relating k_n to the static stiffness k of the cantilever [54]. In case of a non-negligible tip mass, the modal stiffness can be calculated as [51]

$$k_n = k\frac{\int_0^l dx(\Phi''(x,\alpha_n))^2}{3[\Phi(l,\alpha_n)]^2} \tag{2.36}$$

where α_n has to be determined for the respective mass ratio μ using Eq. (2.31).

	mass ratio μ				
stiffness ratio	0	0.01	0.05	0.1	-0.1
k_0/k	1.03	1.03	1.02	1.01	1.09
k_1/k	40.46	43.21	55.83	74.93	33.11
k_2/k	317.2	360.0	578.4	949.66	498
k_3/k	1218	1471	2890	5534	3581
k_4/k	3328	4274	10040	21554	15839

Table 2.2: Ratios of cantilever modal stiffness k_n to the static stiffness k calculated for several eigenmodes of a rectangular cantilever beam with a tip for different mass ratios.

In Chapter 5, several methods for the cantilever stiffness calculation are experimentally investigated regarding the influence of tip mass and the shape of the cross-section on the result. A method to determine the mass ratio μ from the ratio of first and second resonance frequency based on [55] is presented and implemented as a MATLAB algorithm available as supplemental material. To verify the obtained stiffness results, a cooperation with the Physikalisch-Technische Bundesanstalt (PTB, Braunschweig, Germany) offered an independent method for a high-precision measurement of the static cantilever stiffness. The dynamic measurement of the modal stiffness k_n utilising the thermally excited cantilever oscillation is discussed in Chapter 7.

2.3.2 Frequency response

The cantilever oscillating at its nth mode can be described as a damped harmonic oscillator with a periodic driving force given as

$$F_{\text{exc}}(\tau) = k_n A_{\text{exc}} \exp(i\omega\tau) \tag{2.37}$$

with A_{exc} as the drive amplitude and ω as drive frequency [56,57]. The equation of motion can be written as

$$\ddot{q}(\tau) + 2\beta_n\omega_n\dot{q}(\tau) + \omega_n^2 q(\tau) = \frac{F_{\text{exc}}(\tau)}{m_{\text{eff}}} \tag{2.38}$$

with the time dependent cantilever displacement $q(\tau) = q(l,\tau)$, the eigenfrequency ω_n and the damping ratio β_n. After a settling time, the oscillator will basically follow the driving force $F_{\text{exc}}(\tau)$. Therefore, the ansatz

$$q(\tau) = A\exp(i\omega\tau) \tag{2.39}$$

is inserted into Eq. (2.38) yielding a conditional equation for the Amplitude A

$$A(\omega_n^2 - \omega^2 + 2i\beta\omega\omega_n)\exp(i\omega\tau) = A_{\text{exc}}\omega_n^2\exp(i\omega\tau) \tag{2.40}$$

using $\omega_n^2 = k_n/m_{\text{eff}}$. The damping ratio β_n can also be expressed in terms of the quality factor

$$\beta_n = \frac{1}{2Q_n} \tag{2.41}$$

where Q_n is defined as

$$Q_n = 2\pi\frac{\text{energy stored in the oscillating system}}{\text{energy dissipated per cycle}} \quad . \tag{2.42}$$

The complex frequency response of the cantilever is given as

$$H_n(i\omega) = \frac{A}{A_{\text{exc}}} = \frac{1}{1-(\omega/\omega_n)^2 + i\omega/(Q_n\omega_n)} \tag{2.43}$$

for the nth oscillation mode. It can be written as the real amplitude response

$$G_n(\omega) = |H_0(i\omega)| = \frac{1}{\sqrt{(1-\omega^2/\omega_n^2)^2 + \omega^2/(\omega_n^2 Q_n^2)}} \tag{2.44}$$

with the phase angle ϕ_n between driving force and resulting displacement:

$$\phi_n(\omega) = \arctan\left(\frac{-\omega}{Q_n\omega_n(1-(\omega/\omega_n)^2)}\right) \quad . \tag{2.45}$$

A typical resonance curve representing Eq. (2.44) is shown in Fig. 2.17. If the cantilever is operated in high or ultra-high vacuum, the Q-factor is governed by the intrinsic damping of the cantilever as well as additional damping effects due to the fixation of the cantilever as investigated in Chapter 3. Generally, the resonance curve is very narrow. If the cantilever is not operated in vacuum, the Q-factor highly depends on the properties of the surrounding medium, which is shown in Chapter 4.

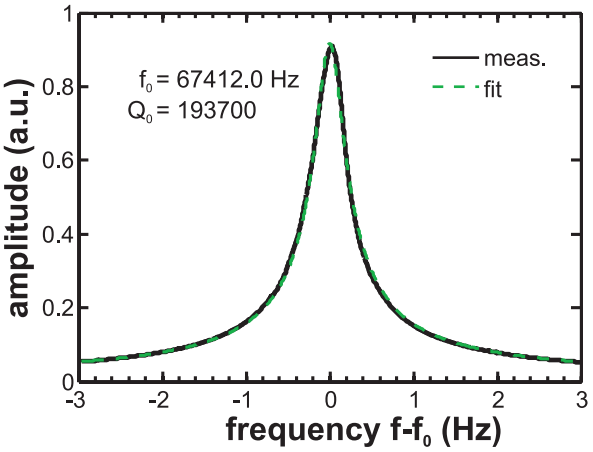

Figure 2.17: Resonance curve of a cantilever oscillating at its fundamental oscillation mode in vacuum. Quality factor Q_0 and resonance frequency f_0 are determined by a fit of Eq. (2.44) to the measured data.

2.3.3 Thermally excited cantilever oscillation

Thermally excited fluctuations of a cantilever are of special interest with regard to the ultimate noise limit in NC-AFM measurements as well as the determination of cantilever properties. Based on an approach originally proposed to describe thermal noise in a resistor [58], the power spectral density for the displacement D^z_{th} of a cantilever in thermal equilibrium with a thermal bath at temperature T is derived. According to the equipartition theorem [59], it is assumed that the mean potential energy of the one-dimensional cantilever oscillator in contact to the thermal bath is equal to $k_{\mathrm{B}}T/2$

$$\frac{1}{2}k\left\langle q^2(t)\right\rangle = \frac{1}{2}k_{\mathrm{B}}T \tag{2.46}$$

with k being the static stiffness of the cantilever. The cantilever is assumed to be excited by random thermal fluctuations in the thermal bath. Although, Eq. (2.46) suggests to determine the stiffness k from a measurement of $\langle q^2(t)\rangle$, this becomes difficult as $\langle q^2(t)\rangle$ is overlaid with noise from other sources. Therefore, a signal analysis in the frequency domain

is required to isolate the contribution due to the thermally excited cantilever excitation [60]. According to the Wiener-Khinchin theorem [59], the cantilever mean-square displacement of this random stationary process can be related to the power spectral density of the cantilever displacement D^z_{th} via

$$\left\langle q^2(t)\right\rangle = \frac{1}{2\pi}\int_0^\infty D^z_{\mathrm{th}}(\omega)d\omega \quad . \tag{2.47}$$

The total mean square cantilever displacement can be decomposed into the sum of displacements originating from its eigenmodes [50] and is related to constants of modal stiffness k_n for the nth eigenmode. Using Eq. (2.46) yields:

$$\begin{aligned}\frac{1}{2}k\left\langle q^2(t)\right\rangle &= \frac{k}{2}\sum_{n=0}^{\infty}\left\langle q_n^2(t)\right\rangle \\ &= \frac{k}{2}\sum_{n=0}^{\infty}\frac{k_{\mathrm{B}}T}{k_n} \\ &= \frac{k_{\mathrm{B}}T}{2}\sum_{n=0}^{\infty}\frac{k}{k_n}\end{aligned} \tag{2.48}$$

where q_n is the displacement corresponding to the nth eigenmode. Equation (2.48) demonstrates that the contribution of the nth eigenmode to the total energy of the thermally excited cantilever is $(k/k_n)(k_{\mathrm{B}}T/2)$.

It has been shown that the modal stiffness k_n, specifically for the higher harmonics, strongly depends on the mass ratio μ [51, 54]. Calculated relations between the modal stiffness and the static stiffness depending on the mass ratio are given in Table 2.2 for the first five eigenmodes. The table shows that 97% of the total oscillation energy is in the fundamental mode for a beam without a tip and this fraction increases as the tip mass increases.

Similar to the mean square cantilever displacement, the total thermal displacement power spectral density is represented as the sum of contributions from the cantilever eigenmodes:

$$D^z_{\mathrm{th}}(\omega) = \sum_{n=0}^{\infty} D^z_{\mathrm{th},n}(\omega) \quad . \tag{2.49}$$

To determine the displacement power spectral density for each mode n, a constant energy spectral density Ψ_n from the thermal bath is assumed to excite the cantilever following the arguments given by Nyquist for the explanation of a thermally excited electrical current in a resistor [58]. The response of the cantilever to this thermal excitation is determined by its amplitude response $G_n(\omega)$ given in Eq. (2.44). Therefore, the energy spectral density of the nth mode, being $(1/2)kD^z_{\mathrm{th},n}$, is represented as

$$\frac{1}{2}kD^z_{\mathrm{th},n}(\omega) = G_n^2(\omega)\Psi_n \quad . \tag{2.50}$$

Considering the result of Eq. (2.48), stating that a fraction k/k_n of the total energy $k_{\mathrm{B}}T/2$ goes to the nth eigenmode, and integrating over $D^z_{\mathrm{th},n}$ one can find for each mode:

$$\frac{k}{k_n}\frac{k_{\mathrm{B}}T}{2} = \frac{1}{4\pi}k\int_0^\infty D^z_{\mathrm{th},n}(\omega)d\omega \tag{2.51}$$

$$= \frac{1}{2\pi}\int_0^\infty G_n^2(\omega)\Psi_n d\omega \tag{2.52}$$

$$= \frac{\Psi_n}{2\pi}\int_0^\infty \frac{1}{(1-\omega^2/\omega_n^2)^2+\omega^2/(\omega_n^2 Q_n^2)}d\omega \quad . \tag{2.53}$$

Substituting $\zeta_n = \omega/\omega_n$ and $d\omega = \omega_n d\zeta_n$

$$\frac{k}{k_n}\frac{k_{\mathrm{B}}T}{2} = \frac{\Psi_n\omega_n}{2\pi}\int_0^\infty \frac{d\zeta_n}{\zeta_n^4+\left(\frac{1}{Q_n^2}-2\right)\zeta_n^2+1} \quad , \tag{2.54}$$

the integral can be solved using

$$\int_0^\infty \frac{d\zeta_n}{\zeta_n^4+a\zeta_n^2+b} = \frac{\pi}{2}\frac{1}{\sqrt{b}\sqrt{a+2\sqrt{b}}} \tag{2.55}$$

with $a = (1/Q_n^2-2)$ and $b = 1$ yielding the excitation energy spectral density for the nth mode:

$$\Psi_n = \frac{2k_BT}{Q_n\omega_n}\frac{k}{k_n} \quad . \tag{2.56}$$

Inserting this result in Eq. (2.50), yields for the displacement power spectral density of the thermally excited cantilever:

$$D^z_{\mathrm{th},n}(\omega) = \frac{4k_{\mathrm{B}}T/(k_nQ_n\omega_n)}{(1-(\omega/\omega_n)^2)^2+\omega^2/(\omega_nQ_n)^2} \tag{2.57}$$

or

$$D^z_{\mathrm{th},n}(f) = \frac{2k_{\mathrm{B}}T/(\pi k_nQ_nf_n)}{(1-(f/f_n)^2)^2+f^2/(f_nQ_n)^2} \tag{2.58}$$

for the nth oscillation mode. This agrees well with results reported by other authors [17,18, 61]. A calculated example of the displacement thermal noise spectral density $d^z_{\mathrm{th}} = \sqrt{D^z_{\mathrm{th}}}$ of a typical cantilever at room temperature for the first four oscillation modes is given in Fig. 2.18.

A short version of this section can be found in Section 2 of the Supporting Information of Chapter 6. The knowledge of the thermal excitation of the cantilever is used for investigating the ultimate noise limit in NC-AFM imaging and spectroscopy (see Chapter 6) and to obtain the cantilever stiffness from thermal noise (see Chapter 7).

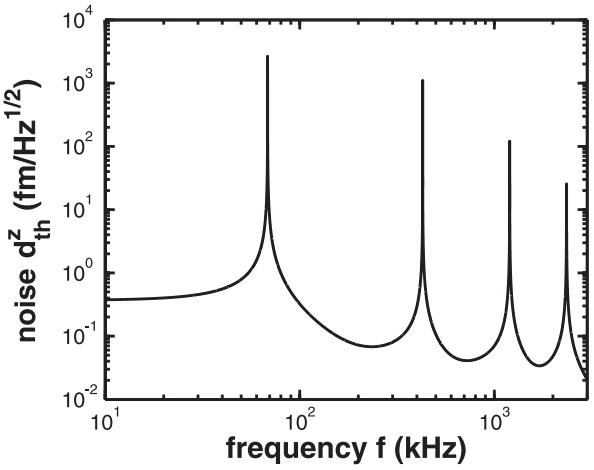

Figure 2.18: Calculated thermal noise spectral density d^z_{th} in the frequency range covering the first four modes of a cantilever with $f_0 = 68347$ Hz, $k_0 = 2.8$ N/m and $Q_0 = 103600$. Values for f_n and k_n of the higher modes are calculated neglecting the tip mass. The Q_n are typical values experimentally determined for a cantilever of this type ($Q_1 = 39000$, $Q_2 = 5800$, $Q_3 = 2000$).

Appendix - solution of the integral in Eq. (2.55)

Factoring:

$$\int_0^\infty \frac{dx}{x^4 + ax^2 + b} = \int_0^\infty \frac{dx}{(x^2 - A)(x^2 - B)} \tag{2.59}$$

Expansion into partial fractions:

$$\frac{C}{x^2 - A} + \frac{D}{x^2 - B} = \frac{1}{(x^2 - A)(x^2 - B)} = \frac{C(x^2 - B) + D(x^2 - A)}{(x^2 - A)(x^2 - B)} \tag{2.60}$$

yields

$$C + D = 0 \Leftrightarrow C = -D \tag{2.61}$$

$$-BC - AD = 1 \Leftrightarrow BD - AD = 1 \tag{2.62}$$

$$D = \frac{1}{B - A} \qquad C = \frac{1}{A - B} \tag{2.63}$$

Insertion yields:

$$\int_0^\infty \frac{dx}{(x^2 - A)(x^2 - B)} = \int_0^\infty \frac{dx}{x^2 - A} \cdot \frac{1}{A - B} + \int_0^\infty \frac{dx}{x^2 - B} \cdot \frac{1}{B - A} \quad . \tag{2.64}$$

The solution of the integral is

$$\int_0^\infty \frac{dx}{x^2 - A} = \frac{\pi}{2\sqrt{-A}} \qquad \text{if} \qquad \mathrm{Re}(A) \leq 0 \bigvee A \notin \mathbb{R} \quad . \tag{2.65}$$

The solutions of the quartic equation are

$$A, B = -\frac{a}{2} \pm \sqrt{\frac{a^2}{4} - b} \tag{2.66}$$

yielding:

$$\int_0^\infty \frac{dx}{x^2 - A} \cdot \frac{1}{A - B} + \int_0^\infty \frac{dx}{x^2 - B} \cdot \frac{1}{B - A} \tag{2.67}$$

$$= \frac{\pi}{2} \left(\frac{1}{\sqrt{-A}} \frac{1}{A - B} + \frac{1}{\sqrt{-B}} \frac{1}{B - A} \right) \tag{2.68}$$

$$= \frac{\pi}{2} \frac{1}{2\sqrt{\frac{a^2}{4} - b}} \left(\frac{1}{\sqrt{\frac{a}{2} - \sqrt{\frac{a^2}{4} - b}}} - \frac{1}{\sqrt{\frac{a}{2} + \sqrt{\frac{a^2}{4} - b}}} \right) \tag{2.69}$$

$$= \frac{\pi}{2} \frac{1}{2\sqrt{\frac{a^2}{4} - b}} \left(\frac{\sqrt{\frac{a}{2} + \sqrt{\frac{a^2}{4} - b}} - \sqrt{\frac{a}{2} - \sqrt{\frac{a^2}{4} - b}}}{\sqrt{b}} \right) \tag{2.70}$$

$$= \frac{\pi}{2} \frac{1}{\sqrt{b}} \sqrt{\frac{a - 2\sqrt{b}}{a^2 - 4b}} = \frac{\pi}{2} \frac{1}{\sqrt{b}} \sqrt{\frac{a - 2\sqrt{b}}{(a + 2\sqrt{b})(a - 2\sqrt{b})}} \tag{2.71}$$

$$= \frac{\pi}{2} \frac{1}{\sqrt{b}\sqrt{a + 2\sqrt{b}}} \quad . \tag{2.72}$$

2.4 Phase-Locked-Loop (PLL) and amplitude control

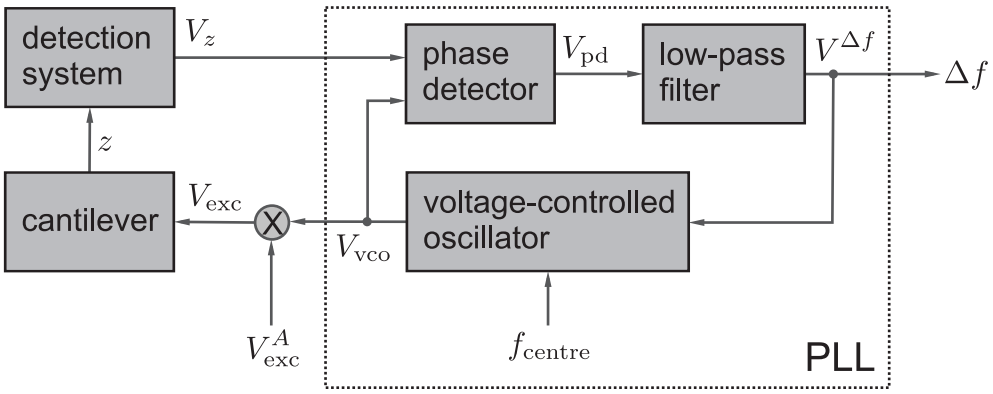

Figure 2.19: Working principle of a phase-locked loop (PLL) for measuring the frequency shift Δf and driving the cantilever oscillation by the voltage V_{exc}.

In NC-AFM, a phase-locked loop (PLL) circuit is used to determine the frequency shift Δf of the cantilever oscillation and to excite the cantilever at its current resonance frequency $f_0+\Delta f$, which is generally shifted with respect to the free oscillating case due to tip-sample interactions. The working principle of a simple PLL is shown in Fig. 2.19 [62]. It consists of a voltage controlled oscillator (VCO) generating a sinusoidal output voltage $V_{\mathrm{vco}}(t)$:

$$V_{\mathrm{vco}}(t) = V_{\mathrm{vco}}^0 \sin(2\pi f t) = V_{\mathrm{vco}}^0 \sin(2\pi(f_{\mathrm{centre}} + K_{\mathrm{vco}} V^{\Delta f}(t))t) \tag{2.73}$$

with the output voltage amplitude V_{vco}^0, the centre frequency f_{centre}, the VCO gain K_{vco} and the voltage $V^{\Delta f}(t)$ being proportional to the frequency shift. The centre frequency of the VCO is set to the eigenfrequency f_0 of the free-oscillating cantilever. The output signal $V_{\mathrm{vco}}(t)$ is used to excite the cantilever with a voltage $V_{\mathrm{exc}}(t) = V_{\mathrm{exc}}^A V_{\mathrm{vco}}(t)$, where the voltage V_{exc}^A defines the gain of the excitation signal. V_{exc}^A can be set either manually or by an amplitude control loop. The latter will be explained later in this section. The VCO gain K_{vco} has a negative sign and is given in units of Hz/V. The response of the cantilever is measured by the detection system (see Fig. 2.19), yielding the voltage signal $V_z(t)$ as the input of the PLL

$$V_z(t) = V_z^0 \sin(2\pi f t + \phi_z(t)) \tag{2.74}$$

with the cantilever oscillation voltage amplitude V_z^0 and the phase shift $\phi_z(t)$. This phase shift includes the phase response $\phi_{\mathrm{cl}}(f)$ of the cantilever, which is for the free-oscillating cantilever given by:

$$\phi_{\mathrm{cl}}(f) = \arctan\left(\frac{-f}{Q_0 f_0 (1-(f/f_0)^2)}\right) \quad . \tag{2.75}$$

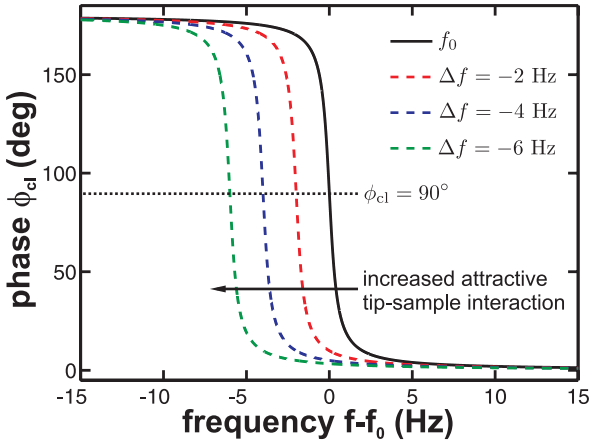

Figure 2.20: Solid line: Phase response of a cantilever with $f_0 = 70000$ Hz and $Q_0 = 100000$. Dashed lines: Phase response of the same cantilever where the resonance frequency is shifted to $f_0 - \Delta f$ Hz modelling tip-sample interactions.

This phase response is plotted as a solid curve in Fig. 2.20. As known from a driven harmonic oscillator, the phase of a cantilever excited at its resonance frequency with respect to the excitation signal is $90°$. The tip-sample interaction yields a shift of the resonance frequency to $f_0 + \Delta f$, where Δf is usually negative due to an attractive tip-sample force as explained before in Section 2.2.1. Dashed lines in Fig. 2.20 show the phase response for a shifted resonance frequency. The oscillation signal $V_z(t)$ as well as the reference $V_{\mathrm{vco}}(t)$ are fed into the phase detector (PD), which is typically realised as a voltage multiplier. Multiplying the signals from Eq. (2.73) and Eq. (2.74) yields

$$V_{\mathrm{pd}}(t) = V_z^0 \sin(2\pi f t + \phi_z(t)) \times V_{\mathrm{vco}}^0 \sin(2\pi f t) \tag{2.76}$$

$$= \frac{1}{2} V_z^0 V_{\mathrm{vco}}^0 \left[\cos(\phi_z(t)) - \cos(2\pi(2f)t + \phi_z(t))\right] \quad . \tag{2.77}$$

The high frequency $(2f)$ part is filtered out by the low-pass loop filter with a bandwidth $B \ll 2f$. Thus, the resulting signal at the output of the low-pass filter reads

$$V^{\Delta f}(t) = \frac{1}{2} V_z^0 V_{\mathrm{vco}}^0 \cos(\phi_z(t)) \quad . \tag{2.78}$$

This signal is fed into the VCO as the input voltage. If the cantilever is oscillated at its eigenfrequency f_0, $V^{\Delta f}(t)$ becomes zero because of $\phi_z(t) = 90°$. Therefore, the output frequency of the VCO remains constant. Now, we assume that the resonance frequency is slightly decreased due to attractive tip-surface interactions as exemplified in Fig. 2.20. As long as the frequency of the VCO is larger than the current resonance frequency, the phase $\phi_z(t)$ becomes smaller than $90°$ (see Fig. 2.20) and $V^{\Delta f}(t)$ becomes positive. Since K_{vco} is a negative gain, the positive $V^{\Delta f}(t)$ causes a decrease of the VCO frequency until $\phi_z(t) = 90°$. Thus, the PLL will always follow the actual resonance frequency of the cantilever. Therefore, the VCO input signal is a measure for the actual frequency shift Δf that can be determined as:

$$\Delta f(t) = K_{\mathrm{vco}} V^{\Delta f}(t) \quad . \tag{2.79}$$

The PLL is *locked* as long as the actual frequency of the VCO is identical to the cantilever resonance frequency, and the phase difference between these two signals is constant. This is possible only within a certain *lock range* that is the range of frequencies in which the resonance frequency can be followed by the VCO frequency. The ability of the PLL to follow fast changes of the resonance frequency is limited by its frequency response that is determined by the characteristics of the PLL regulation loop and loop filter settings.

In most technical realisations, a proportional-integral (PI) controller is put in the loop between low-pass and VCO input. The stability and frequency response of such a PLL system is highly dependent on the VCO gain, the transfer function of the low-pass filter and the PI controller settings. The impact of these settings on the noise behaviour is discussed in detail for several commercial PLL systems in Chapter 6.

To control the cantilever oscillation amplitude, there are basically two operation modes. In the *constant excitation* mode, a specific driving amplitude V_{exc}^{0} is set manually by the adjustment of V_{exc}^{A}. In this case, the oscillation amplitude will remain constant until dissipation due to tip-surface interactions occurs or the cantilever is oscillated besides its actual resonance frequency.

In the *constant amplitude* mode, a control loop is used to maintain a constant oscillation amplitude. The excitation amplitude V_{exc} is increased in case of higher dissipation to maintain a constant oscillation amplitude. The easiest way to measure the cantilever amplitude is by its root mean square (RMS) value

$$V_z^{\mathrm{rms}} = \sqrt{\frac{1}{\tau}\int_0^{\tau} V_z(t)^2 dt} = \frac{1}{\sqrt{2}} V_z^0 \tag{2.80}$$

of the oscillation signal $V_z(t)$ measured over a time interval τ where the last equality is only true for a strictly sinusoidal signal. A scheme for the realisation of a PLL system with RMS amplitude measurement and stabilisation of the amplitude to a pre-set value A_{set} is shown in Fig. 2.21. The disadvantage of this method is that it is not frequency selective. Thus, noise as well as spurious signals contribute to the RMS value. On the other hand, an amplitude measurement is still possible, even if the PLL is unlocked.

Another method is to use a dual-phase lock-in amplifier in the PLL loop yielding the oscillation amplitude V_z^0 and the voltage V^{ϕ} being proportional to the phase ϕ_z as shown in Fig. 2.22. The lock-in amplifier replaces the phase detector and the low-pass filter in Fig. 2.19 as it has an integrated low-pass filter, which is not shown in Fig. 2.22. The phase signal V^{ϕ} is used to close the phase-locked loop consisting of lock-in amplifier, PI controller and VCO. The amplitude V_z^0 is fed into the amplitude control loop controlling V_{exc}^{A} to maintain a constant amplitude of $V_z^0 = V_{\mathrm{set}}$. The advantage of this method is, that the amplitude measurement is performed only in a small frequency band around the resonance frequency defined by the bandwidth of the lock-in amplifier. Therefore, the amplitude determination is widely independent of noise and disturbances. But in case of the PLL being unlocked, the amplitude control fails.

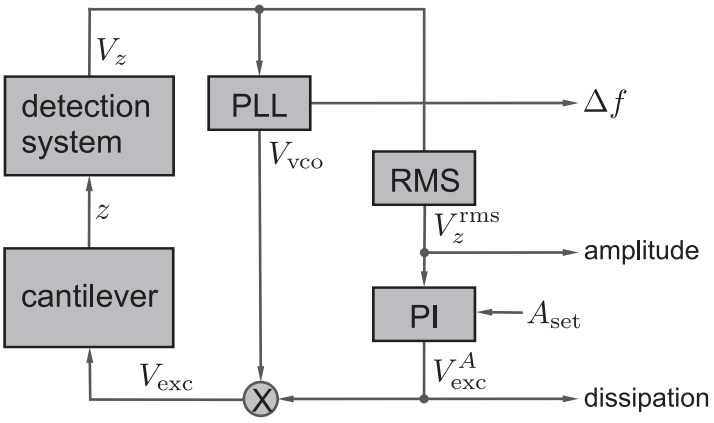

Figure 2.21: Realisation of a PLL system with an amplitude control loop. Here, the oscillation amplitude is determined by an RMS detector.

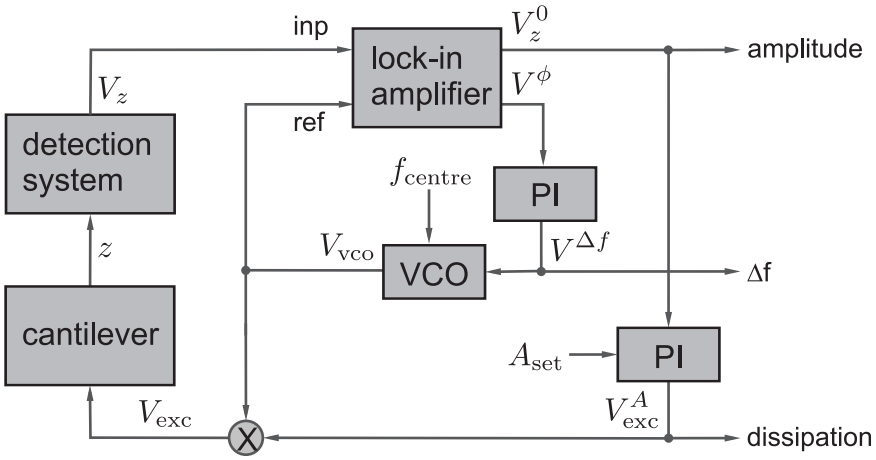

Figure 2.22: Realisation of a PLL system with an amplitude control loop. Here, the oscillation amplitude is determined by using a lock-in amplifier.

2.5 Optimisation of imaging parameters

The imaging quality in FM-AFM depends on many parameters. The eigenfrequency f_0, the spring constant k and the Q-factor are intrinsic properties of the cantilever being primarily defined by the cantilever dimensions and material. The eigenfrequency and the Q-factor are also affected by the mounting and the surrounding medium. Therefore, the measurement can be optimised by an appropriate selection of the cantilever and proper mounting. On the other hand, the oscillation amplitude A and the demodulation bandwidth B can be adjusted independently of the cantilever properties and, therefore, also used for an optimisation of measurements. Further optimisation is possible by the right choice of scanning speed in imaging experiments. Optimisation in this context refers to creating stable imaging conditions (see Section 2.5.1), to reducing noise (see Sections 2.5.2 and 2.5.3) and to diminish the impact of thermal drift (see Section 2.5.4). First, the impact of the force sensor on stability and noise is discussed.

2.5.1 Stability and jump-to-contact

High-resolution NC-AFM requires a sharp tip apex and atomically stable and well defined sensing cluster, which can be destroyed if the tip touches the surface. Therefore, it is important to avoid the "jump-to-contact" (JTC) where the cantilever sticks to the surface. Two conditions have to be considered to avoid the JTC [39]. A JTC will not happen if the force gradient k_{ts} of the tip-sample potential V_{ts} does not fully compensate the stiffness of the cantilever:

$$k + k_{\mathrm{ts}} > 0 \quad . \tag{2.81}$$

On the other hand, the JTC can be avoided if the overall force acting on the cantilever stays positive:

$$kA + F_{\mathrm{ts}} > 0 \tag{2.82}$$

where kA is the retracting force of the displaced cantilever.

A combination of these two criteria allows one to calculate the optimum spring constant k_{opt} for a given amplitude A

$$k_{\mathrm{opt}} = s\frac{-F_{\mathrm{ts}}^{\mathrm{min}}}{A + F_{\mathrm{ts}}^{\mathrm{min}}/k_{\mathrm{ts}}^{\mathrm{min}}} \tag{2.83}$$

where $s > 1$ as a safety factor [19]. $F_{\mathrm{ts}}^{\mathrm{min}}$ and $k_{\mathrm{ts}}^{\mathrm{min}}$ are the minima of the tip-sample force and force gradient, respectively. The calculated k_{opt} is shown in Fig. 2.23 for different safety factors s as a function of the amplitude while $F_{\mathrm{ts}}^{\mathrm{min}}$ and $k_{\mathrm{ts}}^{\mathrm{min}}$ are obtained from

the previously discussed Lennard-Jones model potential. Being larger than a certain spring constant, e.g., 2500 N/m for $s = 50$, the first condition, given by Eq. (2.81), is always fulfilled yielding stable operation independent of the oscillation amplitude.

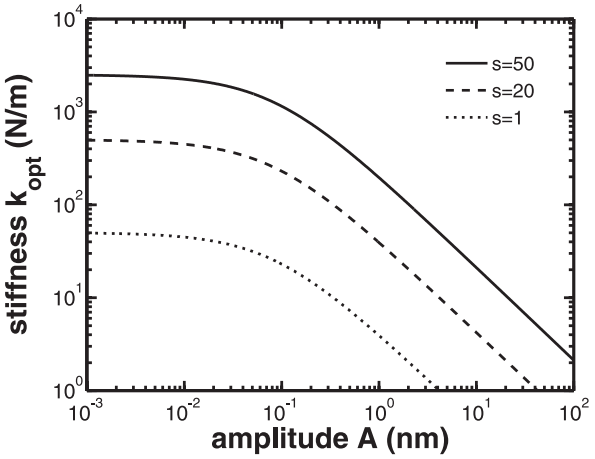

Figure 2.23: Calculated optimum spring constant k_{opt} as a function of the oscillation amplitude A using Eq. (2.83) and for different safety factors s.

2.5.2 Noise for negligible tip-sample interaction

The power spectral density $D_{\mathrm{tot}}^{\Delta f}$ of the frequency shift noise without tip-sample interaction as described in Chapter 6 consists of the following contributions:

$$D_{\mathrm{tot}}^{\Delta f}(\omega_m) = D_{\mathrm{th}}^{\Delta f} + D_{\mathrm{ds}}^{\Delta f} \quad . \tag{2.84}$$

$D_{\mathrm{th}}^{\Delta f}$ is the frequency-shift thermal noise power spectral density, which essentially depends on the cantilever temperature and its properties. $D_{\mathrm{ds}}^{\Delta f}$ describes the frequency-shift noise power spectral density originating from the noise floor D_{ds}^{z} of the detection system. To characterise the noise power spectral density $D_{\mathrm{tot}}^{\Delta f}(\omega_m)$ with a single number, the root mean square (RMS) of the total frequency shift noise is calculated as:

$$(\delta f_{\mathrm{tot}})^2 = (\delta f_{\mathrm{th}})^2 + (\delta f_{\mathrm{ds}})^2 = \frac{1}{2\pi}\int_0^\infty D_{\mathrm{tot}}^{\Delta f}(\omega_m) d\omega_m \quad . \tag{2.85}$$

The noise contributions $D_{\mathrm{th}}^{\Delta f}$ and $D_{\mathrm{ds}}^{\Delta f}$ scale inversely proportional to the squared cantilever oscillation amplitude A.

2.5.3 Noise with significant tip-sample interaction

Up to here, the frequency shift noise power spectral density $D_{\mathrm{tot}}^{\Delta f}$ was calculated without any tip-sample interaction. Practically, however, the frequency shift noise is distance dependent

as it is affected by the tip-sample interaction. Therefore, the quantity $D_{\mathrm{ts}}^{\Delta f}$ is introduced describing the additional frequency shift noise due to tip-sample interaction [18]. Here, a brief introduction into the theory describing $D_{\mathrm{ts}}^{\Delta f}$ is given, however, a detailed discussion and analysis is beyond the scope of this thesis. Based on this theory, the total frequency noise then reads:

$$D_{\mathrm{tot}}^{\Delta f}(\omega_m) = D_{\mathrm{th}}^{\Delta f} + D_{\mathrm{ds}}^{\Delta f} + D_{\mathrm{ts}}^{\Delta f} \tag{2.86}$$

with

$$D_{\mathrm{ts}}^{\Delta f}(\omega_m) = \alpha_{\mathrm{ts}}^2 \left| \frac{H_{\mathrm{filter}}}{1 - \frac{i}{Q} H_{\mathrm{c}} H_{\mathrm{filter}} + \beta_{\mathrm{ts}} H_z H_{\mathrm{filter}}} \right|^2 D^A \quad . \tag{2.87}$$

H_{filter} denotes the transfer function of the PLL frequency response as described in Chapter 6. $H_{\mathrm{c}}(\omega_m)$ is an approximation of the transfer function Eq. (2.43) of the cantilever oscillation with $\omega = \omega_0 + \omega_m$ for $\omega_m \ll \omega_0$:

$$H_{\mathrm{c}}(\omega_m) = \frac{1}{\frac{i}{Q} - \frac{2\omega_m}{\omega_0}} \quad . \tag{2.88}$$

The transfer function $H_z(\omega_m)$ of the PI distance control loop is given as

$$H_z(\omega_m) = P_z \left(1 + \frac{I_z}{i\omega_m} \right) \tag{2.89}$$

with the parameters P_z and I_z. The parameters $\alpha_{\mathrm{ts}}(A, z)$ and $\beta_{\mathrm{ts}}(A, z)$ have units of Hz/nm. They describe the coupling between amplitude noise δA as well as distance noise δz to frequency shift noise δf due to tip-surface interactions [18]. Both parameters have a complicated dependence on the tip-sample interaction $\Delta f(z)$ as is described in [18]. For the following simulations, α_{ts} is adjusted such that the resulting curves agree with the experimental data, while β_{ts} is adapted from [18]. The quantity D^A, which is the noise power spectral density of the oscillation amplitude, is given by

$$D^A(\omega_m) = 8 \left| \frac{H_{\mathrm{c}}}{1 - 2i H_{\mathrm{c}} H_A} \right|^2 \left(\frac{k_{\mathrm{B}} T}{k Q \omega_0} + |H_A|^2 D_{\mathrm{ds}}^z \right) \tag{2.90}$$

with the noise floor of the detection system D_{ds}^z (see Chapter 6) and the transfer function of the amplitude control loop $H_A(\omega_m)$

$$H_A(\omega_m) = -H_{\mathrm{lp}} P_A \left(1 + \frac{I_A}{i\omega_m} \right) \tag{2.91}$$

with H_{lp} as the transfer function of the low-pass filter in the amplitude control loop governed by parameters P_A and I_A.

In the following, a qualitative comparison of experiment and simulation is discussed for measurements performed with system C. Figure 2.24a shows the frequency shift noise spectral density $d_{\mathrm{tot}}^{\Delta f}$ measured for different frequency shift set-points Δf_{set}. While the curve for very large tip-sample separations without tip-sample interaction ($\Delta f_{\mathrm{set}} = 0$ Hz) is similar to curves described in Chapter 6, the curves obtained with larger Δf_{set} exhibit a broad peak at 60 Hz in the plateau region of $d_{\mathrm{tot}}^{\Delta f}(f_m)$ (see Chapter 7). This peak increases with larger Δf_{set}, i.e. increasing tip-sample interaction. The measured $\Delta f(z)$ curve shown in Fig. 2.24b can be used to relate these frequency shift set-points to quantities of tip-sample distance given by the piezo position z_{p}. Note that z_p has an unknown offset to the absolute tip-sample distance z. In Fig. 2.24c, a numerical simulation using Eq. (2.86) allows to obtain qualitatively similar results as for the measurement presented in Fig. 2.24a. Up to now, only the cantilever and PLL parameters have been precisely considered. To fully characterise the amplitude distance control loop, the ratio between voltage amplitude at the excitation piezo and the effective excitation of the cantilever needs to be investigated in future work. As the amplitude control loop operates with an input voltage of V_A and an output voltage V_{exc}, the value P_A of the amplitude control loop needs to be scaled by $V_A/(V_{\mathrm{exc}}Q)$ to fit to the simulation operating with amplitudes A in units of displacement. This factor is chosen to be 0.036 throughout the simulation for this cantilever. The settings for the distance control loop are taken from the simulation in [18] and not modeled exactly for this system. The comparison of Fig. 2.24a and Fig. 2.24c shows a good qualitative agreement for measurement and simulation. Figure 2.24d shows the measured RMS noise in dependence on Δf_{set}. In close proximity to the sample, the RMS noise is increased by more than a factor of two compared to the noise without tip-surface interaction.

Next, the influence of the amplitude gain settings on the total noise is investigated. Up to here, a value of $P_A = 0.013$ has been used yielding an optimum step-response for amplitude changes. Figure 2.25 shows the measured frequency shift noise spectral density close to the sample ($\Delta f_{\mathrm{set}} = -70$ Hz) for three different amplitude gain settings P_A. A gain reduction to $P_A = 0.008$ (dotted line) yields a slightly increased noise compared to the optimum setting of $P_A = 0.008$ (solid blue line). An increase of the amplitude gain to $P_A = 0.039$, however, yields a decrease of the noise spectral density in the peak centred at 60 Hz while a second peak centred at 300 Hz appears.

These results are qualitatively reproduced by the simulation shown in Fig. 2.26a. Note, that the low Q-factor of 1600 and the noise floor of $d_{\mathrm{ds}}^{z} = 312\ \mathrm{fm}/\sqrt{\mathrm{Hz}}$ measured for cantilever AR 20 are comparably bad values for a cantilever of this type. Cantilever AR 17 originating from the same batch as AR 20 has a Q-factor of 39200 and a noise floor of $d_{\mathrm{ds}}^{z} = 98\ \mathrm{fm}/\sqrt{\mathrm{Hz}}$ (see Chapter 6). Therefore, simulations are performed to investigate the effect of both quantities individually. All simulations in Fig. 2.26 are performed using the same PLL filter settings, yielding a bandwidth of $B_{-3\mathrm{dB}} = 258$ Hz. In case of Fig. 2.26a, the thermal noise limit (see Chapter 6) is $B_{\mathrm{th}}^{\mathrm{lim}} = 202$ Hz, thus, operation is performed close to the thermal noise limit. The RMS frequency shift noise of the curve with optimum

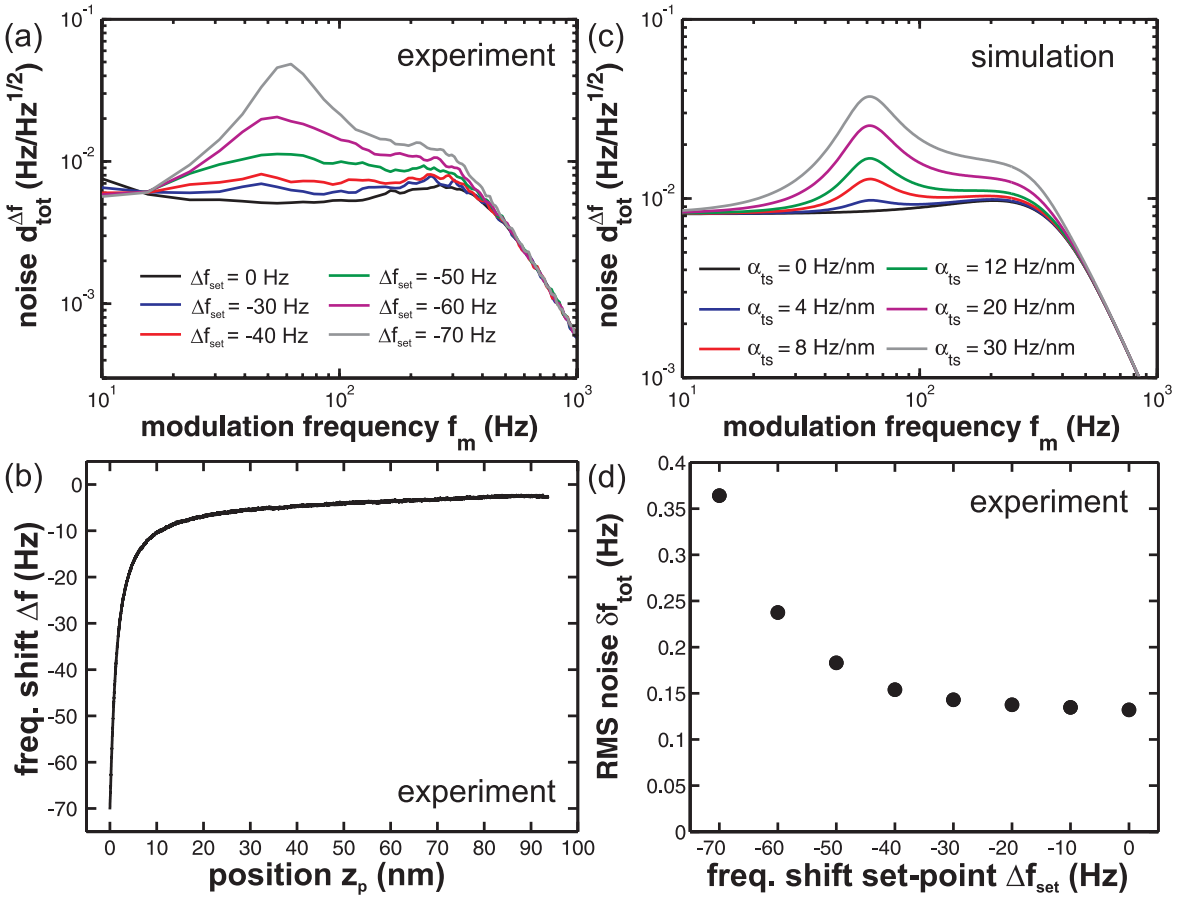

Figure 2.24: Measurements performed in system C with cantilever AR 20 ($f_0 = 269218.5$, $Q = 1600$, $k_{\mathrm{dim}} = 28$ N/m) at $T = 26.5$ K on a $CaF_2(111) + C_{60}$ sample. The detection system noise floor is $d_{\mathrm{ds}}^z = 312\ \mathrm{fm}/\sqrt{\mathrm{Hz}}$. The amplitude control loop is set to $P_A = 0.013$ and $I_A = 1$ Hz. The distance control loop is enabled. (a) Frequency shift noise spectral density $d_{\mathrm{tot}}^{\Delta f}$ for different Δf_{set}. (b) $\Delta f(z)$ curve recorded in dependence on the z-piezo position z_p. (c) Calculated noise spectral density $d_{\mathrm{tot}}^{\Delta f}$ for different values of α_{ts}. The frequency response H_{filter} of the PLL is modeled as described in Chapter 6 with parameters $o = 3$, $f_c = 500$ Hz, $P = -2.0$ Hz/deg, $I = 1$ Hz. The filter H_{lp} of the amplitude control loop is identical to the loop filter in the PLL for this system. The gain P_A of the amplitude control loop is scaled by 0.036 compared to the setting in the PLL device. The properties of the distance control loop are chosen as $\beta_{\mathrm{ts}} P_Z = 0.2$ and $\beta_{\mathrm{ts}} I_z = 2000$ Hz identical to the simulation in [18]. The values α_{ts} are chosen to obtain qualitatively similar results as for the measurement shown in (a). (d) RMS value of the total frequency shift noise determined in dependence on Δf_{set}.

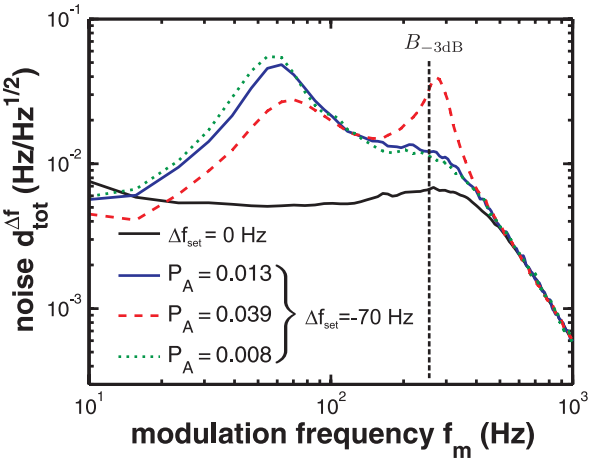

Figure 2.25: Measured noise spectral density $d_{\mathrm{tot}}^{\Delta f}$ for three different settings of the P gain of the amplitude control loop and $\Delta f_{\mathrm{set}} = -70$ Hz. The black line is a measurement of the noise spectral density without any tip-sample interaction. The other parameters are identical to Fig. 2.24.

amplitude gain $P_A = 0.013$ is $\delta f = 0.35$ Hz, while the curve with $P_A = 0.039$ yields $\delta f = 0.46$ Hz due to the additional peak. In the simulation shown in Fig. 2.26b, the noise floor is reduced to $d_{\mathrm{ds}}^z = 100\ \mathrm{fm}/\sqrt{\mathrm{Hz}}$ increasing the thermal noise limit to $B_{\mathrm{th}}^{\mathrm{lim}} = 629$ Hz. The changes compared to (a) are negligible except for a significant decrease of noise for the curve simulated with $P_A = 0.039$. Here, the RMS noise of the curve with $P_A = 0.013$ is $\delta f = 0.29$ Hz, while the curve with $P_A = 0.039$ has almost the same RMS value of $\delta f = 0.28$ Hz. In Fig. 2.26c, the Q-factor is increased to 40000, while the noise floor stays at $d_{\mathrm{ds}}^z = 312\ \mathrm{fm}/\sqrt{\mathrm{Hz}}$. Compared to (a) and (b), where the total noise is mostly dominated by the thermal noise, (c) is dominated by the contribution of the detection system noise. The RMS noise of the curve with $P_A = 0.013$ is $\delta f = 0.26$ Hz. For the setting of $P_A = 0.039$, a sharp peak at 355 Hz appears, meaning an oscillation in the Δf signal. The RMS value of $\delta f = 1.95$ Hz is an order of magnitude larger than the RMS values of the other curves. Finally, in Fig. 2.26d, the noise floor is reduced to $d_{\mathrm{ds}}^z = 100\ \mathrm{fm}/\sqrt{\mathrm{Hz}}$ while the Q-factor stays at 40000. Here, the RMS noise of the curve with $P_A = 0.013$ is $\delta f = 0.11$ Hz, which is only one third compared to the RMS value determined for (a). The sharp peak in the curve for $P_A = 0.039$ is still present, while the total RMS noise is reduced to $\delta f = 0.66$ Hz.

These simulations give a first impression on modelling the frequency noise spectral density under the influence of tip-surface interactions and comparing the theoretical results to experimental data. The theoretically predicted effect of additional noise in the case of a tip-sample interaction is confirmed experimentally. Although a detailed discussion on the influence of all involved parameters is beyond the scope of this work, it is found that additional peaks appear in the frequency shift noise spectral density spectrum due to tip-sample interaction and the aforementioned coupling of the feedback loops. Similar to the findings for the frequency shift noise without tip-sample interaction, the total frequency noise can be decreased by a reduction of the thermal noise represented by an increase of the Q-factor as well as by a decreased noise floor. However, the adjustment of the amplitude feedback loop becomes more critical for higher Q-values as sharp peaks in the frequency noise spectral density may appear that bear the risk of invoking oscillations in the Δf signal.

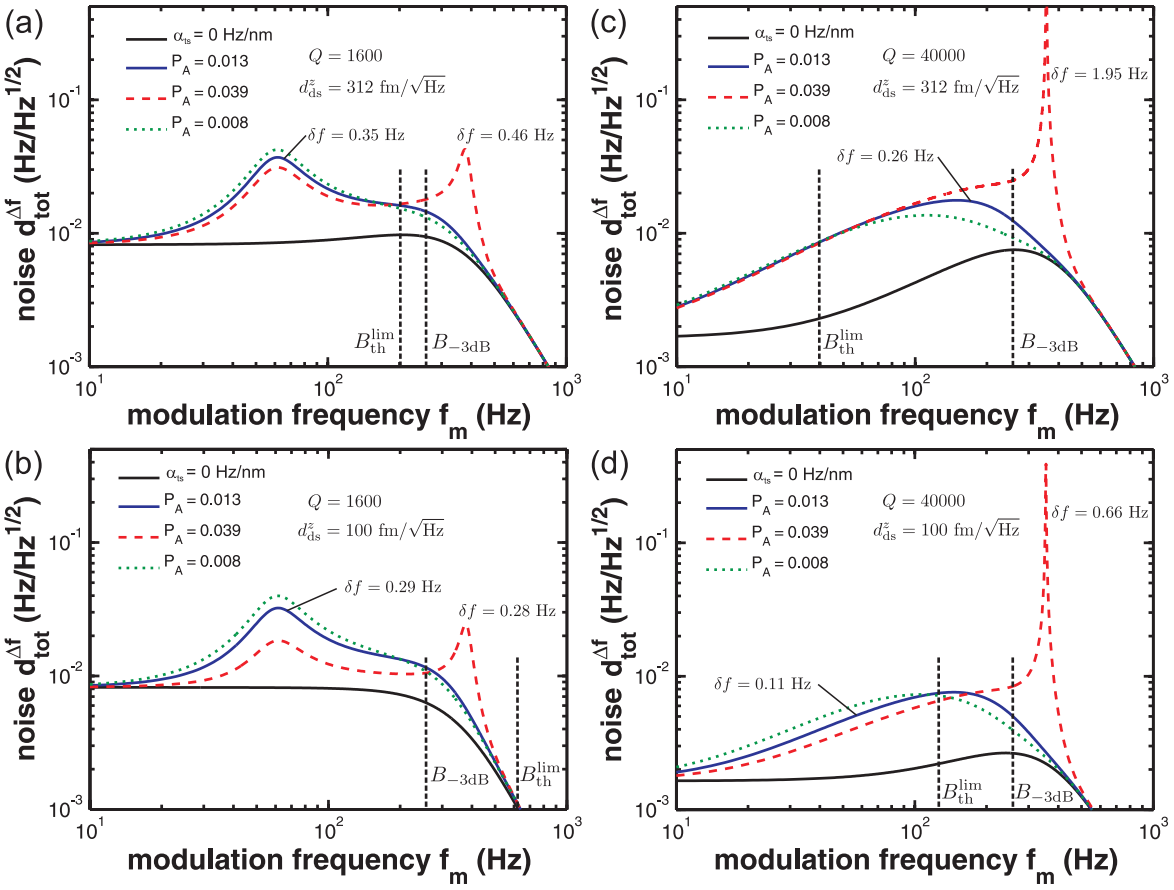

Figure 2.26: Simulated noise spectral density $d^{\Delta f}_{\text{tot}}$ for three different amplitude gains P_A while noise floor d^z_{ds} and Q-factor are varied from (a) to (d). The black curves represent the frequency noise spectral density without tip-sample interaction. The other simulation parameters are identical to Fig. 2.24c.

2.5.4 Bandwidth, scan speed and thermal drift

As shown in Chapter 6, the range of modulation frequencies f_m up to which the frequency noise is limited only by thermal noise is given by

$$B_{\mathrm{th}}^{\mathrm{lim}} = \sqrt{\frac{f_0 k_B T}{2\pi k Q}} \frac{1}{d_{\mathrm{ds}}^z} \tag{2.92}$$

where f_0, k and Q are cantilever properties contributing to the thermal noise, d_{ds}^z is the displacement noise of the detection system. To facilitate thermal noise limited operation, the effective bandwidth of the PLL demodulator is set to a value smaller than or equal to $B_{\mathrm{th}}^{\mathrm{lim}}$.

It should be considered that a small modulation bandwidth limits the scan speed that can be used for imaging structures with a certain periodicity. To understand this practically, several imaging parameters need to be introduced: The image is typically a square with an edge length w_{image}. It is scanned line by line where each of the n_{pixel} lines consists of n_{pixel} points due to the square shape. To scan a single line takes a time t_{line}, yielding a scan speed of $v_{\mathrm{scan}} = w_{\mathrm{image}}/t_{\mathrm{line}}$. Therefore, the acquisition time of the entire image is $t_{\mathrm{image}} = 2 \cdot n_{\mathrm{pixel}} \cdot t_{\mathrm{line}}$ as each of the lines is scanned forward and backward. We assume to record an atomic resolution image with an interatomic distance a. The modulation frequency of the atomic features during image acquisition can be calculated as $f_m = v_{\mathrm{scan}}/a$. To avoid a loss of information, f_m needs to be significantly smaller than the bandwidth of the PLL demodulator.

However, a lower scan speed and, therefore larger acquisition time enhances distortions due to thermal drift expressed by the drift velocity v_{drift}. In this example, only lateral drift is considered. After each image, the position of the scanner relative to the sample is shifted by $w_{\mathrm{drift}} = t_{\mathrm{image}} \cdot v_{\mathrm{drift}}$.

To illustrate these considerations, a simulation is performed based on a simple model and typical instrumental parameters. The surface with a square atomic structure is modeled as a constant-height frequency shift image exhibiting sinusoidal periodicity

$$\Delta f(x,y) = \frac{1}{2} \sin\left[(x + t v_{\mathrm{drift}} \cos\phi_{\mathrm{drift}}) \frac{2\pi}{a}\right] \sin\left[(y + t v_{\mathrm{drift}} \sin\phi_{\mathrm{drift}}) \frac{2\pi}{a}\right] \tag{2.93}$$

and having a corrugation of 1 Hz. To visualize the effect of drift, a defect modeled by a Gaussian function

$$\begin{aligned} \Delta f_{\mathrm{defect}}(x,y) = &\exp\left[-\left(\frac{x + t v_{\mathrm{drift}} \cos\phi_{\mathrm{drift}} - 5.25a}{a/4}\right)^2\right] \\ &\times \exp\left[-\left(\frac{y + t v_{\mathrm{drift}} \sin\phi_{\mathrm{drift}} - 3.75a}{a/4}\right)^2\right] \end{aligned} \tag{2.94}$$

is added to the image. The lateral drift is expressed by the drift speed v_{drift} and the drift angle ϕ_{drift} measured relative to the x-direction as depicted in Fig. 2.27. Drift in z-direction,

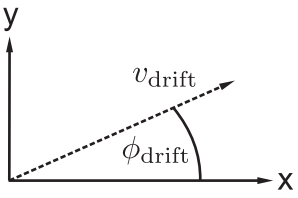

Figure 2.27: Coordinate system illustrating drift speed v_{drift} and drift angle ϕ_{drift}.

nonlinear drift behaviour, as well as drift of the eigenfrequency f_0 are not considered here. The effect of the demodulation bandwidth on the measured corrugation is expressed by an attenuation due to $G_{\mathrm{filter}}(f_m)$ (see Chapter 6). The effect of frequency shift noise is generated by a set of random numbers $\Delta f_{\mathrm{noise}}(x, y)$ being added to $\Delta f(x, y)$. For a realistic magnitude of noise, $\Delta f_{\mathrm{noise}}(x, y)$ is normalised to a typical RMS frequency shift noise value based on the parameters in Table 2.3:

$$\left\langle \Delta f_{\mathrm{noise}}^2(x, y) \right\rangle = \delta f_{\mathrm{tot}} \quad . \tag{2.95}$$

Table 2.3: Experimental parameters and oscillation properties of cantilever AR 17 operated in system C (see Chapter 6).

temperature	T	300 K
eigenfrequency	f_0	276 360 Hz
quality factor	Q	39 200
spring constant	k	26 N/m
noise of detection system	d_{ds}^z	$98\ \mathrm{fm}/\sqrt{\mathrm{Hz}}$
oscillation amplitude	A	10 nm
demodulation bandwidth	$B_{-3\mathrm{dB}}$	105 Hz

This simplification considers neither the spectral configuration of the noise as investigated in Chapter 6 nor the increase of the frequency noise level in close distance to the sample surface as investigated in Section 2.5.3.

Table 2.4: Imaging parameters used for the simulation based on typical experimental parameters for atomic resolution imaging. Variations of these parameters are specified in the simulated images.

interatomic distance	a	0.3 nm
image size	$(w_{\mathrm{image}})^2$	3×3 nm
points per line	n_{pixel}	512
drift speed	v_{drift}	100 pm/min
drift angle	ϕ_{drift}	$0\,^\circ$
line time	t_{line}	300 ms
modulation frequency	f_m	33.3 Hz

A simulation using the imaging parameters from Table 2.4 and different demodulation bandwidth settings $B_{-3\mathrm{dB}}$ is shown in Fig. 2.28. The RMS frequency shift noise, which is calculated from the given bandwidth and the experimental parameters from Table 2.4 is ranging from $\delta f_{\mathrm{tot}} = 0.025$ Hz for $B_{-3\mathrm{dB}} = 103$ Hz to $\delta f_{\mathrm{tot}} = 0.42$ Hz for $B_{-3\mathrm{dB}} =$

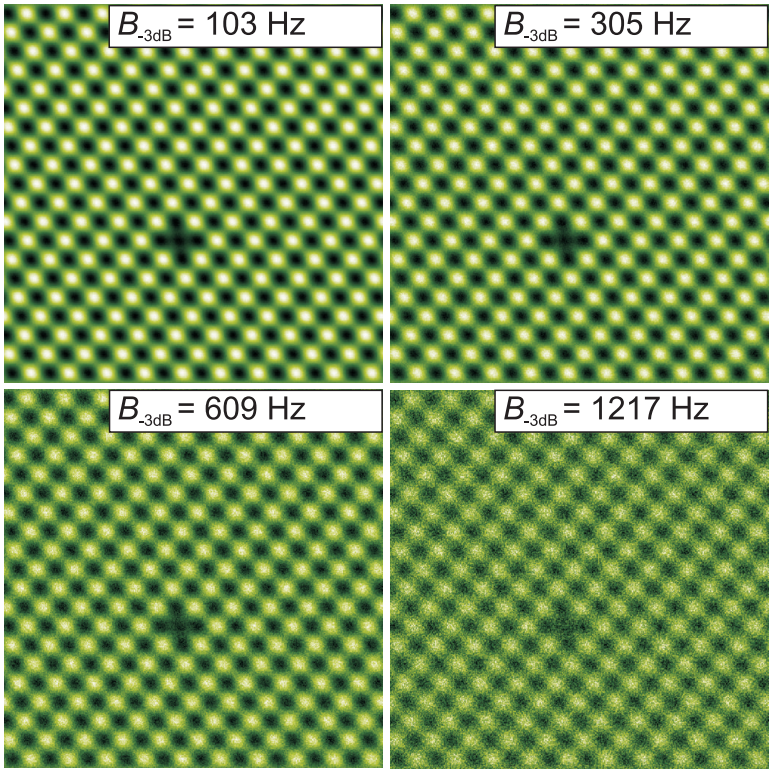

Figure 2.28: Simulated Δf images based on Eqs. (2.93) and (2.94) with different demodulation bandwidth settings $B_{-3\mathrm{dB}}$ ranging from 103 Hz to 1217 Hz. Image size 3×3 nm.

1217 Hz. As the modulation frequency f_m is only 33 Hz, there is no attenuation of the corrugation by the filter of the PLL system even for the low bandwidth setting $B_{-3\mathrm{dB}} = 103$ Hz. In this case, thermal noise limited operation is possible. The total drift per image is $w_{\mathrm{drift}} = 1.5$ nm, which is five times the interatomic distance $a = 0.3$ nm.

In Fig. 2.29, the simulation is performed using different line times t_{line} but the same demodulation bandwidth of $B_{-3\mathrm{dB}} = 103$ Hz for all images. In case of $t_{\mathrm{line}} = 30$ ms, the total drift per image is only 51 pm. But the high modulation frequency $f_m = 333$ Hz yields an attenuation of the corrugation by $G_{\mathrm{filter}}(f_m) = 0.08$. Therefore, the corrugation is only about three times larger than the RMS frequency noise of δf_{tot}. Increasing the line time to $t_{\mathrm{line}} = 100$ ms, the simulation is performed with $f_m = 100$ Hz close to the demodulator bandwidth. The corrugation is attenuated by $G_{\mathrm{filter}}(f_m) = 0.73$ and the total drift per image is 171 pm. For the higher line times simulated here, the attenuation by the filter of the demodulator becomes negligible, but the effect of the drift becomes more important as visualized by the displacement of the defect. For the commonly used line time of $t_{\mathrm{line}} = 300$ ms, the drift per image if about 0.5 nm. Having a total drift close to the image size (1.7 nm at $t_{\mathrm{line}} = 1000$ ms) or even larger (3.4 nm at $t_{\mathrm{line}} = 2000$ ms) does not allow any retrospective drift correction based on tracking a feature over a sequence of images as this feature will be lost after one image. In that case, an in-situ drift correction is required. Without any additional drift compensation, the optimum line time for this situation is between 100 ms and 300 ms where the drift is small while the corrugation is not attenuated by the filter.

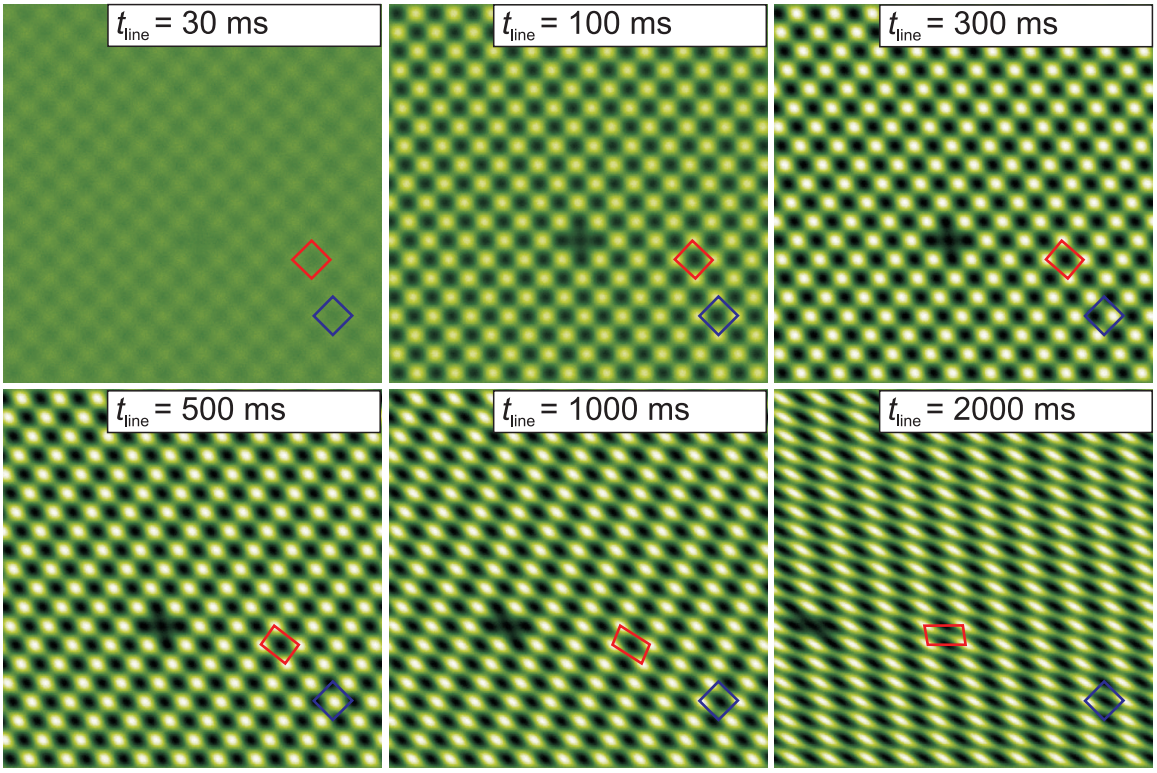

Figure 2.29: Simulated Δf image based on Eqs. (2.93) and (2.94) with different line times t_{line} ranging from 30 ms to 2000 ms. The blue square indicates a unit cell of the undistorted surface while the red parallelogram indicates how the measured unit cell is affected by drift. Image size 3×3 nm.

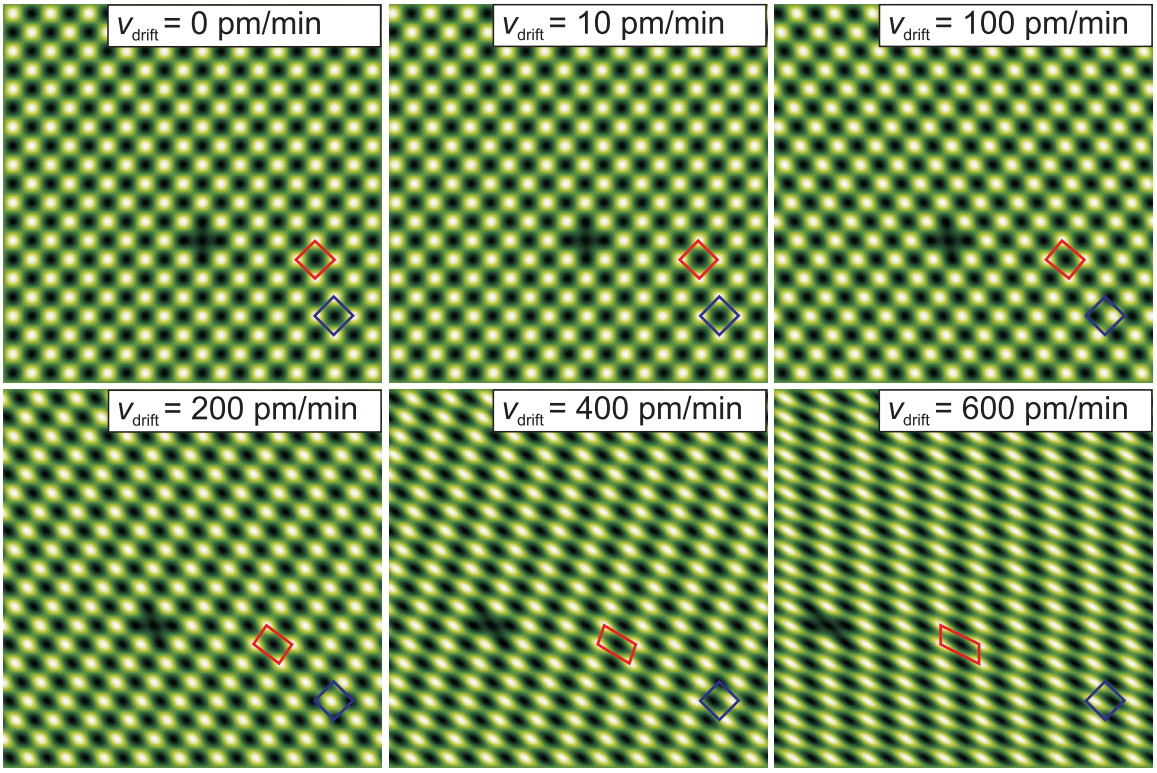

Figure 2.30: Simulated Δf image based on Eqs. (2.93) and (2.94) with different drift velocities v_{drift} ranging from 0 pm/min to 600 pm/min. The blue square indicates a unit cell of the undistorted surface while the red parallelogram indicates how the measured unit cell is affected by drift. Image size 3×3 nm.

In Fig. 2.30, the simulation is performed using different drift velocities v_{drift} ranging from 0 pm/min up to 600 pm/min. An image without any drift is only hypothetical. A drift speed of 10 pm/min is what typically can be obtained when applying atom-tracking and feed-forward techniques [15]. For this drift speed, a total drift per image is 51 pm. Drift speeds of 100 pm/min are commonly measured if the system is in good thermal equilibrium. With 0.5 nm, the drift per image is slightly larger than the interatomic distance. Drift velocities of the order of 600 pm/min cause a heavy distortion of the measured image. Such drift velocities are typical for a system that is thermally unbalanced due to sample heating, cooling or unstable ambient conditions in the laboratory.

To be consistent with the drift behaviour of the $CaF_2(111)$ surface, a hexagonal pattern is generated by a superposition of three plane waves propagating from the origin under an angle of $120\,^\circ$ from each other [63]:

$$\begin{aligned}\Delta f(x,y) =& \frac{2}{9}\left\{\cos\left[\frac{2(y+tv_{\mathrm{drift}}\sin\phi_{\mathrm{drift}})}{\sqrt{3}}\cdot\frac{2\pi}{a}\right]\right.\\ &+\cos\left[\left(x+tv_{\mathrm{drift}}\cos\phi_{\mathrm{drift}}-\frac{(y+tv_{\mathrm{drift}}\sin\phi_{\mathrm{drift}})}{\sqrt{3}}\right)\cdot\frac{2\pi}{a}\right]\\ &\left.+\cos\left[\left(x+tv_{\mathrm{drift}}\cos\phi_{\mathrm{drift}}+\frac{(y+tv_{\mathrm{drift}}\sin\phi_{\mathrm{drift}})}{\sqrt{3}}\right)\cdot\frac{2\pi}{a}\right]\right\}\end{aligned} \tag{2.96}$$

The simulation of the hexagonal surface pattern in Fig. 2.31 is performed analogue to the rectangular pattern in Fig. 2.30. While the pattern is clearly hexagonal up to a drift speed of 100 pm/min, it appears to be rectangular or rhombohedral at higher drift speeds.

In Fig. 2.32, the simulation has been performed for a drift velocity of $v_{\mathrm{drift}} = 300$ pm/min and different drift angles ϕ_{drift}. For drift angles $\phi_{\mathrm{drift}} = 0\,^\circ$ and $\phi_{\mathrm{drift}} = 180\,^\circ$, drift occurs only in x-direction that is the fast scan direction where the scan speed is orders of magnitude larger than the drift velocity. Therefore, there is no significant distortion of the shape of a single scan line, however, the whole scan lines are shifted against each other yielding a deformation in the appearance of the atoms. Additionally, the lattice appears to be rectangular instead of hexagonal. The distance between the horizontal lines is still correct. The scan speed in y-direction is 586 pm/min, which is of the same order of magnitude as the drift speed. Turning the drift angle towards the y-axis, some other distortion effects are revealed. With $\phi_{\mathrm{drift}} = 90\,^\circ$, the drift is parallel to the y-direction. This increase of the effective scan speed in the slow scanning direction yields a scanner movement of 4.5 nm instead of 3 nm, increasing the number of displayed atomic lines and the atoms appearing smaller. Otherwise, a drift angle of $\phi_{\mathrm{drift}} = 270\,^\circ$ being antiparallel the the y movement reduces the effective scan speed and, therefore, the scanner movement from 3 nm to 1.5 nm. In that case, the visible distance between the horizontal lines is increased and the atoms appear to be larger. This behaviour can also be observed if the scan direction is alternated after each image changing the orientation of the slow scanning direction towards the drift. As extreme situation, the drift could totally compensate the slow scanning movement yielding stripes instead of single atoms if the same line is scanned during the entire image acquisition.

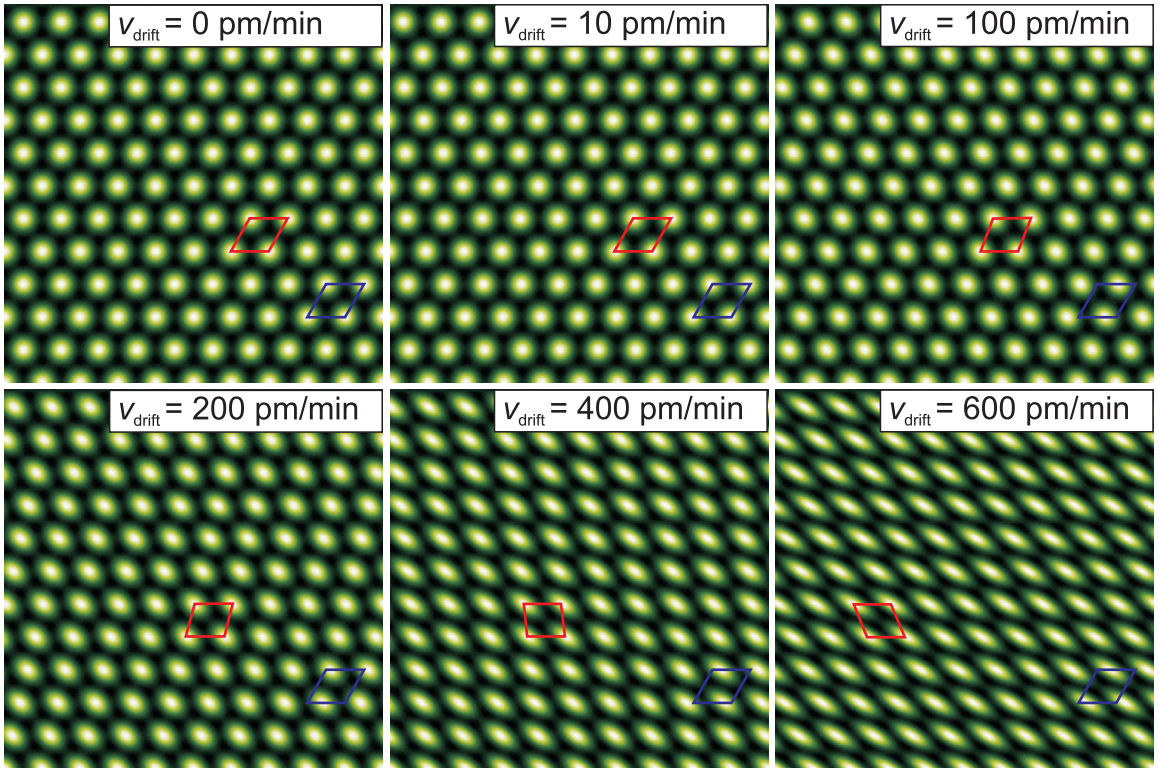

Figure 2.31: Simulated Δf image of a surface with hexagonal symmetry based on Eq. (2.96) with different drift velocities v_{drift} ranging from 0 pm/min to 600 pm/min. The blue parallelogram indicates a hexagonal unit cell of the undistorted surface while the red parallelogram indicates how the measured unit cell is affected by drift. Image size 3×3 nm.

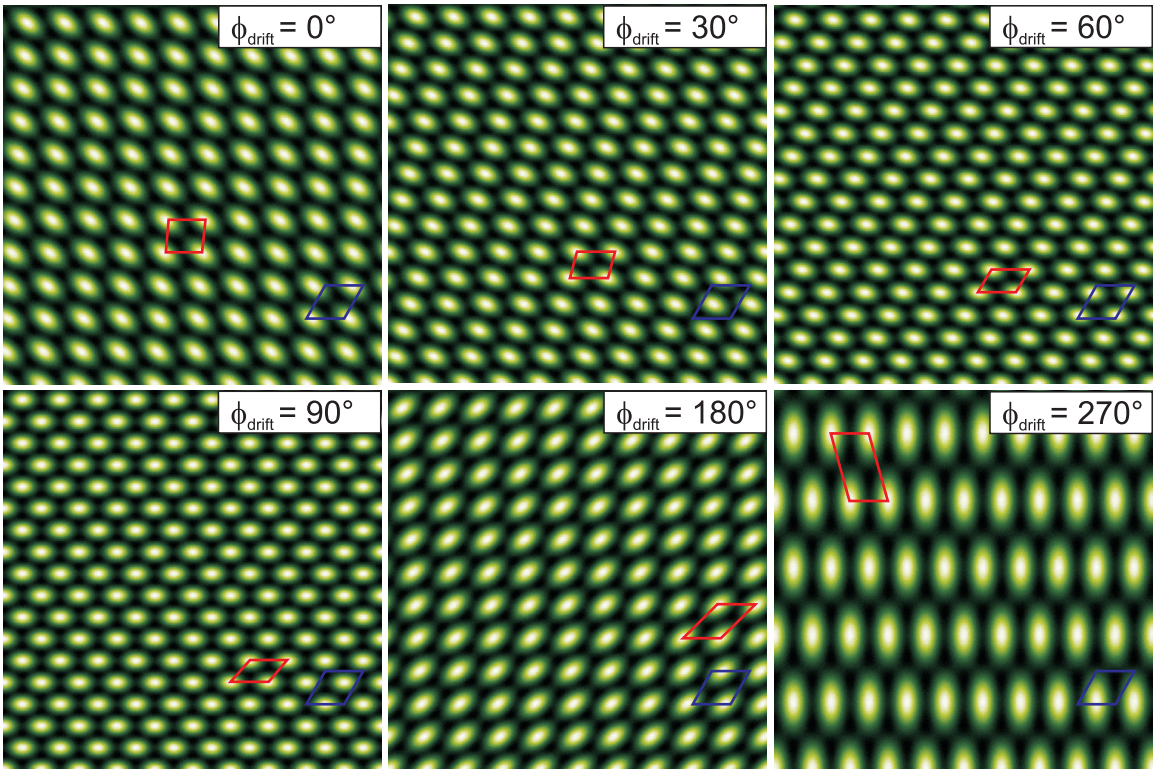

Figure 2.32: Simulated Δf image of a surface with hexagonal symmetry based on Eq. (2.96) with a drift velocity $v_{\mathrm{drift}} = 300$ pm/min and different drift angles ϕ_{drift}. The blue parallelogram indicates a hexagonal unit cell of the undistorted surface while the red parallelogram indicates how the measured unit cell is affected by drift. Image size 3×3 nm.

2.6 Experimental setups

The thesis focuses on cantilever properties and noise related to the detection of the cantilever deflection; corresponding measurements are performed on different setups, which are briefly introduced as NC-AFM systems A, B and C and supplementary systems like a cantilever test chamber. Most investigations have been performed in system C and the cantilever test chamber. Therefore, these systems are described in somewhat more detail. More details on all NC-AFM systems, especially regarding the noise performance, can be found in Chapter 6.

The cantilever holders for the NC-AFM systems as well as the mounting stage of the cantilever test chamber are shown in Fig. 2.33. The cantilever holders of system A and system B are fixed by a three-point bearing in the AFM system. The holder of system A is clamped while the holder of system B is magnetically held in its position. The holder of system C is pushed with only two pins into spring bushings on the AFM scan head. This introduces an additional degree of freedom allowing slightly different distances between cantilever and sample holder, but makes cantilever adjustment less reproducible. In contrast to these holders, which require the cantilever to be glued, the mounting stage of the test chamber allows for cantilever fixation by clamping.

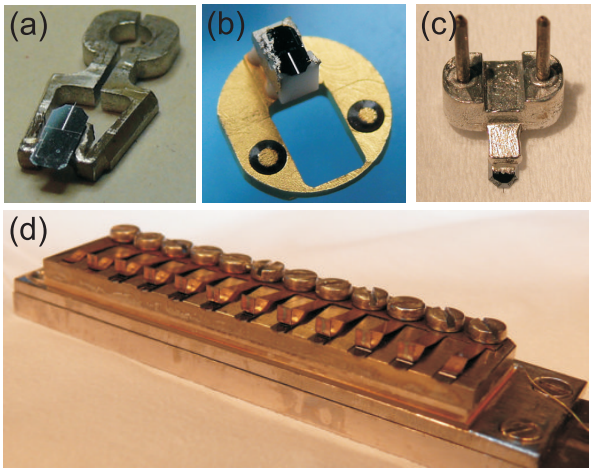

Figure 2.33: Cantilever holders for (a) system A, (b) system B, (c) system C. (d) Stage for clamping cantilevers in the test chamber.

2.6.1 Omicron UHV AFM/STM (system A)

This system is used to investigate the reproducibility of Q-factor measurements depending on the fixation of cantilever holders on which the cantilevers are glued (see Chapter 3). Additionally, the noise behaviour of this system is investigated in Chapter 6. The system is a room temperature UHV AFM/STM (Omicron NanoTechnology GmbH, Taunusstein, Germany) based on the design of Howald *et al.* [64]. The system has been improved by replacing the light source of the beam deflection system by an external laser diode and

by replacing the preamplifier by a home-built one. These changes raised the signal-to-noise ratio by a factor of 10 [65]. In this system, the cantilever and the beam deflection system are stationary, while the surface scanning is realised by moving the sample. This system is equipped with a Nanosurf easyPLL controller and detector (Nanosurf AG, Liestal, Switzerland) as the amplitude feedback loop and frequency demodulator. A cantilever holder for this system is shown in Fig. 2.33a.

2.6.2 Omicron VT AFM/STM (system B)

This system is used to investigate the Q-factors as well as the modal stiffness of cantilevers with resonance frequencies around 300 kHz at room temperature (see Chapters 3 and 7). Furthermore, this system is used to verify experimentally various theoretical descriptions on noise behaviour of cantilevers and the detection system, as presented in Chapter 6. The variable temperature AFM/STM (VT SPM, Omicron Nanotechnology GmbH, Taunusstein, Germany) operates in a sample temperature range from 25 K to 1500 K. This system has been optimised for the signal-to-noise ratio [66] and was later extended with an atom-tracking system [15, 29]. In this system, the sample is fixed, while the cantilever holder is moved (see Fig. 2.33b for the cantilever holder). An easyPLL plus controller and detector (Nanosurf AG, Liestal, Switzerland) is used as the amplitude feedback loop and frequency demodulator.

2.6.3 RHK UHV 750 (system C)

This system is used to investigate the oscillation properties of cantilever in the range from 50 kHz to 2 MHz. High-frequency cantilevers as well as higher harmonic oscillation modes of 70 kHz and 300 kHz cantilevers are studied regarding eigenfrequencies f_n, quality factors Q_n and the modal stiffness k_n (see Chapter 7). Additionally, the frequency response and noise characteristics of this system is investigated for several cantilever types as reported in Chapter 6. This setup consists of three UHV chambers, namely the AFM chamber housing a commercial UHV 750 (RHK Technology, Inc., Troy, MI, USA), a sample preparation chamber and a load lock. The latter is used to introduce new cantilevers and samples into the system, maintaining the UHV pressure in AFM and preparation chamber. The base pressure of this system is below 10^{-10} mbar. The whole UHV system is placed on pneumatic isolators for protection from external vibrations. Further information about this setup and previously made improvements can be found in previous theses [67, 68]. Recent modifications of the preparation chamber as well as the sample preparation procedures for the $CaF_2(111)$ surface and the deposition of C_{60} on the surface are explained in [69].

The UHV 750 is based on a beetle type scanner [70, 71]. In this system, the scan head (see Fig. 2.34) including cantilever and optical beam deflection setup is moved while the sample is fixed. The scan head has three legs, each consisting of a piezoceramic tube and a sapphire sphere at its end. The cantilever is glued on a cantilever holder as shown in

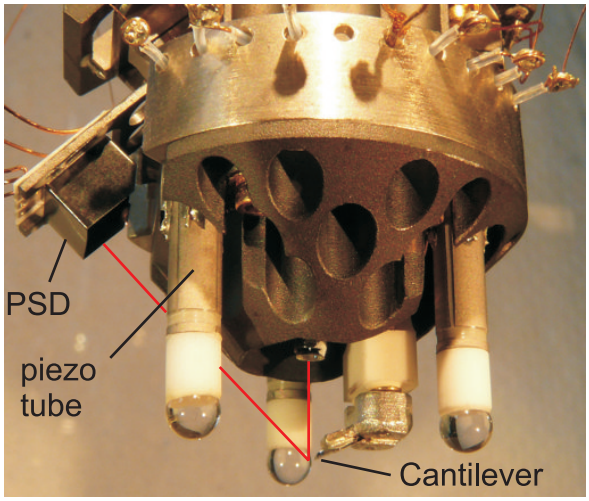

Figure 2.34: Photograph of the UHV 750 scan head with three piezo legs. The central piezo stack is covered by the scan head chassis and not visible here. A cantilever holder is plugged into the spring bushings on the bottom of the central piezo stack. The optical path of the laser light, entering from the lens at the optical fibre end to the back side of the cantilever and the reflection to the PSD is indicated by a red line.

Fig. 2.33c. The holder consists of die-cast aluminum and is equipped with two pins. These pins are plugged into spring bushings on the central piezo stack ensuring a stable fixation of the cantilever. The microscope uses optical beam deflection for detecting the cantilever displacement. The light for the OBD comes from an external laser diode and is coupled and is coupled into the system by an optical fibre. The optical fibre with a small lens glued at its end focuses the light on the back side of the cantilever. The fibre end can be moved by a piezo motor mounted on the scan head to adjust the laser spot on the cantilever. The reflected laser light is directly reflected onto the PSD, which can be moved laterally to center the spot of the reflected beam in its most sensitive area. The piezo legs are used for coarse positioning and approach by walking on the ramp on top of the sample holder (see Fig. 2.35) using inertial motion. The same piezo tubes perform the lateral scan movement

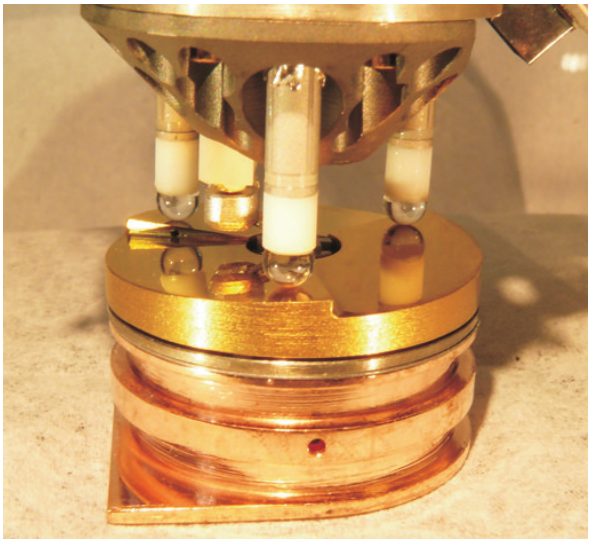

Figure 2.35: Photograph of the UHV 750 scan head standing on the sample holder ramp. The body of the sample holder has a specimen mount and a filament integrated in its bottom to allow for heating.

during image acquisition. The central piezo stack is used to control the tip-sample distance in z-direction and to excite the cantilever oscillation. An advantage of this compact setup with circular symmetry is that relative movements of tip and surface due to thermal drift

are reduced [70]. On the other hand, the height of the sample holder ramp limits the z coarse motion to about 1 mm. Therefore, the cantilever as well as the sample have to be well adjusted regarding the height in their respective holders. Additionally, the orientation of the scan area to the sample may be rotated up to $120°$ depending on the scanner position on the ramp.

Figure 2.36 shows a schematic overview of the electrical connections of system C. An RHK PLLpro2 is used as the amplitude feedback loop and frequency demodulator. The cantilever excitation signal V_{exc} is connected to the excitation piezo (z-mod) on the scan head (see Fig. 2.37 for a schematic overview of the scan head wiring). The cantilever displacement yields a current difference ΔI_z between the quadrants of the photodiode, which is converted by the preamplifier into a voltage signal V_z. This voltage V_z is fed into the PLLpro2 for demodulation. More details about frequency response of the preamplifier and the PLL system as well as the noise performance of the detection system can be found in Chapter 6. The signals for frequency shift Δf, amplitude and dissipation are transferred from the PLLpro2 to the SPM 100 byelectrical connections.

Except for the cantilever excitation, all piezos are controlled by the SPM 100. The signal ground and the $\pm$X and $\pm$Y signals are connected to a switchbox (RHK PPC 100) distributing these signals to the AFM scan head. The signal ground is connected to the body of the scanner, to piezo electrodes as counterpart of the z-scan and z-mod signals and to a shielding between cantilever holder and piezo stack. The $\pm$X and $\pm$Y signals are distributed to the outer electrodes of the three piezo tubes, denoted as $\pm\mathrm{X}_{1/2/3}$ and $\pm\mathrm{Y}_{1/2/3}$. With the given piezo calibration factors, the maximum image size is $5.07\ \mu\mathrm{m}$ in x- and y-direction. The inner electrodes of the piezo tubes are connected to z-offset, where the output voltage is manually controlled by potentiometers allowing for a distance compensation in z-direction of up to 728 nm. The z-scan signal is controlled by the distance control loop and is connected to two piezos in a parallel arrangement in the center stack. The maximum operating range is 187.2 nm in z-direction. A bias voltage can be applied to the cantilever to compensate for long-range electrostatic interactions between tip and sample.

For inertial motion, the $\pm$X output of the SPM 100 is able to generate a sawtooth voltage with 20 ms period and 130 V amplitude. The PPC 100 is used to apply this waveform on the $\pm\mathrm{X}_{1/2/3}$ or the $\pm\mathrm{Y}_{1/2/3}$ electrodes for lateral coarse movement in x- or y-direction. For coarse movement in z-direction as well as tip-sample approach, the signal $\pm$X is mixed on the $\pm\mathrm{X}_{1/2/3}$ and $\pm\mathrm{Y}_{1/2/3}$ electrodes in a way to generate a rotational movement.

Noise from the piezo electronics plays an important role in NC-AFM imaging and has, therefore, to be considered and eliminated. While noise in the low frequency region mainly contributes to a positioning uncertainty, noise contributions in a higher frequency region covering the cantilever resonance frequency are critical for proper signal detection. Discrete disturbances close to the resonance frequency may appear also in the frequency shift signal (see Chapter 6) and, therefore, as disturbing oscillations in the image. If a spurious peak is far enough away from the resonance, it can simply be suppressed by the filter of the PLL system. Peaks in close distance to the resonance are critical, as the cantilever is more

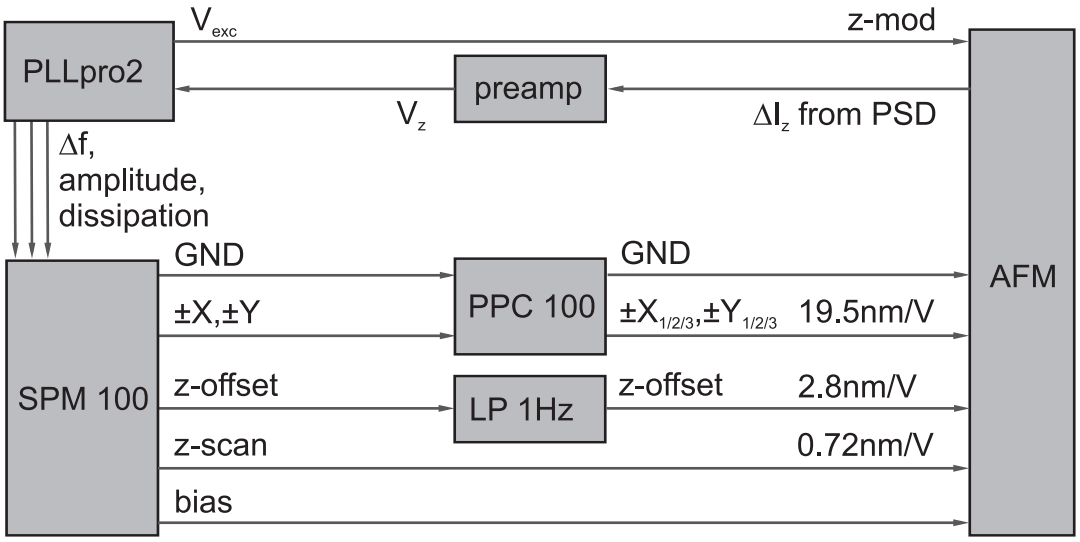

Figure 2.36: Schematic overview of the signal flow in system C. The piezo control outputs (±X, ±Y, z-offset, z-scan) of the SPM 100 have an operating range of ±130 V. The bias voltage can be set to ±10 V. The piezos of the scan head have different sensitivities relating the applied voltage to piezo expansion.

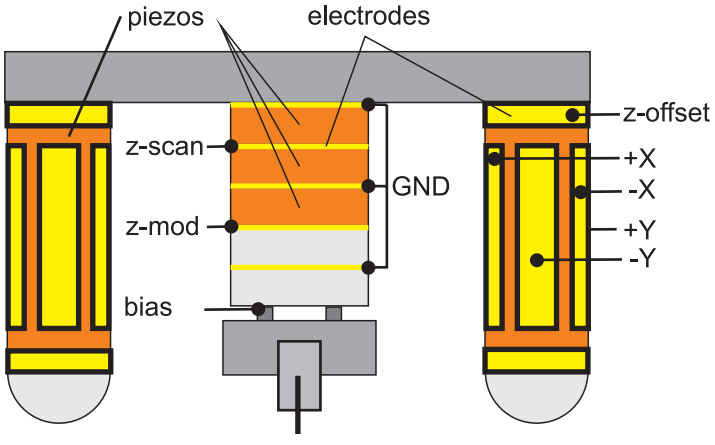

Figure 2.37: Schematic illustration of the UHV 750 scan head layout and its wiring.

sensitive for excitations close to the resonance. Smaller separations are even more critical, as the cantilever becomes more sensitive for excitations close to its resonance frequency and the PLL may fail to follow the actual resonance frequency of the cantilever. Ideally, the noise in the displacement signal is limited to the thermal noise of the cantilever (see Chapter 6). But white noise on the outputs of the piezo control electronics yields an additional excitation of the cantilever. Effectively, this yields an additional excitation of the cantilever similar to thermal excitation. The largest contribution of electrical noise originates from the z-offset channel of the SPM 100 as illustrated in Fig. 2.38. Although

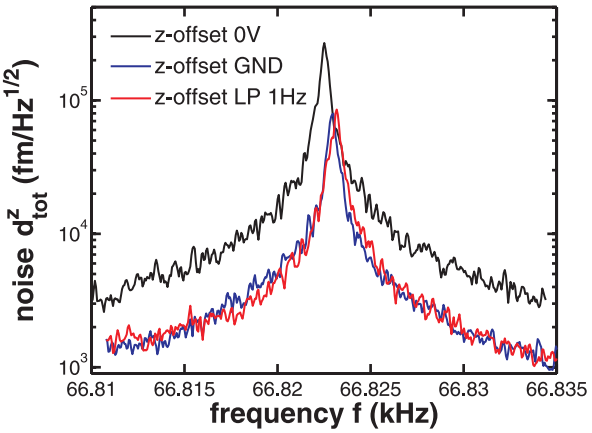

Figure 2.38: Measurements of the effective displacement noise spectral density of the thermally excited oscillation of a cantilever with $f_0 = 66824$ Hz and $Q_0 = 186000$ with additional excitation by electrical noise. The z-mod cable is disconnected from the PLL excitation signal. The piezo connections z-scan, $+$X, $-$X, $+$Y and $-$Y are connected to GND (see Figs. 2.36 and 2.37). The curves are recorded for three different conditions of the z-offset signal (set to 0 V, connected to GND, set to 0 V with low-pass filter).

the piezo tubes are not directly connected to the cantilever (see Fig. 2.37), the presence of the z-offset signal yields a deflection noise about three times larger than for thermal excitation alone (all other piezos connected to GND). Considering that the thermally excited displacement noise is described by the relation $d^z_{\mathrm{th}} \propto \sqrt{k_{\mathrm{B}}T/k}$, this increased noise level corresponds to a temperature of about 3000 K. Using $T = 300$ K, this would underestimate the stiffness by a factor of 0.1. As the z-offset signal is only set manually and does not require fast changes, a lowpass filter with a cutoff frequency of about 1 Hz can be placed between the SPM 100 and the z-offset electrodes on the scan head (see Fig. 2.36). The effect of this filter is illustrated in Fig. 2.38. With the 1 Hz lowpass filter, the measured displacement noise spectral density is identical to the thermally excited displacement noise spectral density measured with z-offset connected to GND. The purely thermal excitation is highly important for the characterisation of cantilevers from thermal noise as is discussed in Chapter 7. Having a line time of about 100 ms, the fast scan direction operates with a frequency of about 10 Hz while the movement in the perpendicular direction is even slower. The z-signal typically does not exceed a frequency of 1 kHz to follow the surface corrugation. As the piezos have a capacity of approximately $C_{\mathrm{p}} = 5$ nF, resistors can be included in the signal lines to form first order lowpass filters with a cutoff frequency of

$$f_c = \frac{1}{2\pi R \cdot C_{\mathrm{p}}} \quad . \tag{2.97}$$

In the present setup, the z-signal is filtered with a resistor $R = 10$ kΩ ($f_c = 3.18$ kHz). The x and y signals are filtered with resistors $R = 33$ kΩ ($f_c = 0.96$ kHz). Technically, the

latter filter is equipped with a switchable bypass of the resistors to allow for passing the coarse motion sawtooth voltage.

2.6.4 Cantilever test chamber

The cantilever test chamber, described in more detail in Chapter 3, can be used to measure cantilever resonance frequencies and their Q-factors under UHV conditions (see Fig. 2.39). To allow for reusing the cantilevers in other NC-AFM systems, the cantilevers are mounted using a clamping mechanism (see Fig. 2.33d). This does not require glueing the cantilever support chip onto a specific holder. To measure the cantilever oscillation behaviour as a function of pressure, a combined pirani/cold-cathode pressure gauge is used [72, 73]. The electronics of this setup has initially been designed for frequencies ranging from 60 kHz to 240 kHz. Accepting a significant loss of signal intensity, an operation from 10 kHz up to 400 kHz is, however, possible. This range covers the eigenfrequencies of the most commonly used cantilever types.

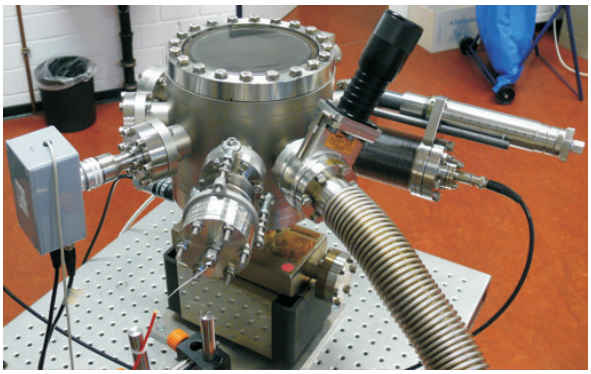

Figure 2.39: Exterior view of the test chamber setup allowing to investigate the oscillation behaviour of NC-AFM cantilevers under UHV conditions.

2.6.5 Scanning electron microscope (SEM)

Beside the characterisation of cantilever oscillation properties in the AFM system or the test chamber setup, an analysis of cantilever dimensions is performed. Commercial silicon cantilevers are typically pre-characterised by the manufacturer regarding the cantilever beam dimensions where length l and width w are obtained by optical microscopy with uncertainties of $\Delta l = 2.5$ μm and $\Delta w = 1.5\mu$m, respectively, while the thickness t is obtained by laser interferometry with an uncertainty of $\Delta t = 0.2\mu$m. As optical microscopy is limited to a resolution in order of the wavelength of the visible light, it is not suitable for the investigation of the cantilever tip shape and the determination of the tip radius. In contrast, the scanning electron microscope (SEM) offers a resolution down to a few nanometers. The SEM measurements presented in this thesis were performed on a commercial SEM (type Auriga with Supra 55 technology, Carl Zeiss Microscopy GmbH, Jena, Germany) located at the Hochschule Osnabrück (see Fig. 2.40a). To allow for an investigation of cantilever

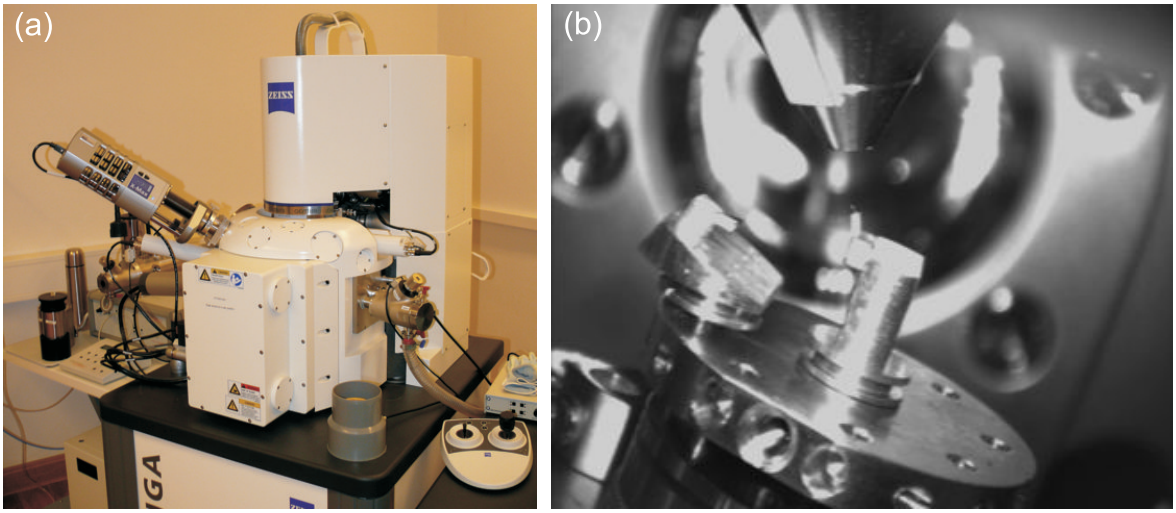

Figure 2.40: (a) Photograph of the SEM instrument located at the Hochschule Osnabrück. (b) Camera view into the SEM chamber with a cantilever fixation for front view imaging.

tips before and after performing NC-AFM measurements, suitable adaptors were designed, allowing to support the cantilevers glued on the AFM specific cantilever holder inside the SEM chamber. The design allows for three different viewing angles. Therefore, the full size and shape information of cantilevers can be obtained. Figure 2.40b shows an interior view of the SEM chamber, one cantilever is visible in a front view perspective (see Fig. 2.41i for the respective adaptor carrying a cantilever holder for system C). The SEM measurement is performed at a base pressure of 10^{-6} mbar and an accelerating voltage of 3 kV. Utmost care has to be taken in the precise alignment of the cantilever holder to obtain accurate dimensional results. The top view of the full cantilever, as shown in Fig. 2.41b, allows to determine the length and the mean width of the cantilever beam as $l = 127 \pm 7$ μm and $\overline{w} = 29 \pm 2$ μm in this example. The thickness of this cantilever beam is obtained from the side view shown in Fig. 2.41(f) as $t = 3.8 \pm 0.2$ μm. Although one might expect a specifically high precision from a SEM measurement, the SEM measurement uncertainty is similar or slightly larger than that of the dimensions given in the manufacturer's datasheet.

The view of a macroscopic pyramidal tip as given by Fig. 2.41(c), (g) and (j) allows one to estimate the tip mass. The determination of spring constant and resonance frequency from cantilever dimensions under consideration of the tip mass is discussed in Chapter 5. Highly resolved images of the tip apex as shown in Fig. 2.41(d), (h) and (l) are used for an estimation of the tip radius, which is, e.g., required for the investigation of long-range electrostatic and van-der-Waals tip-sample interactions.

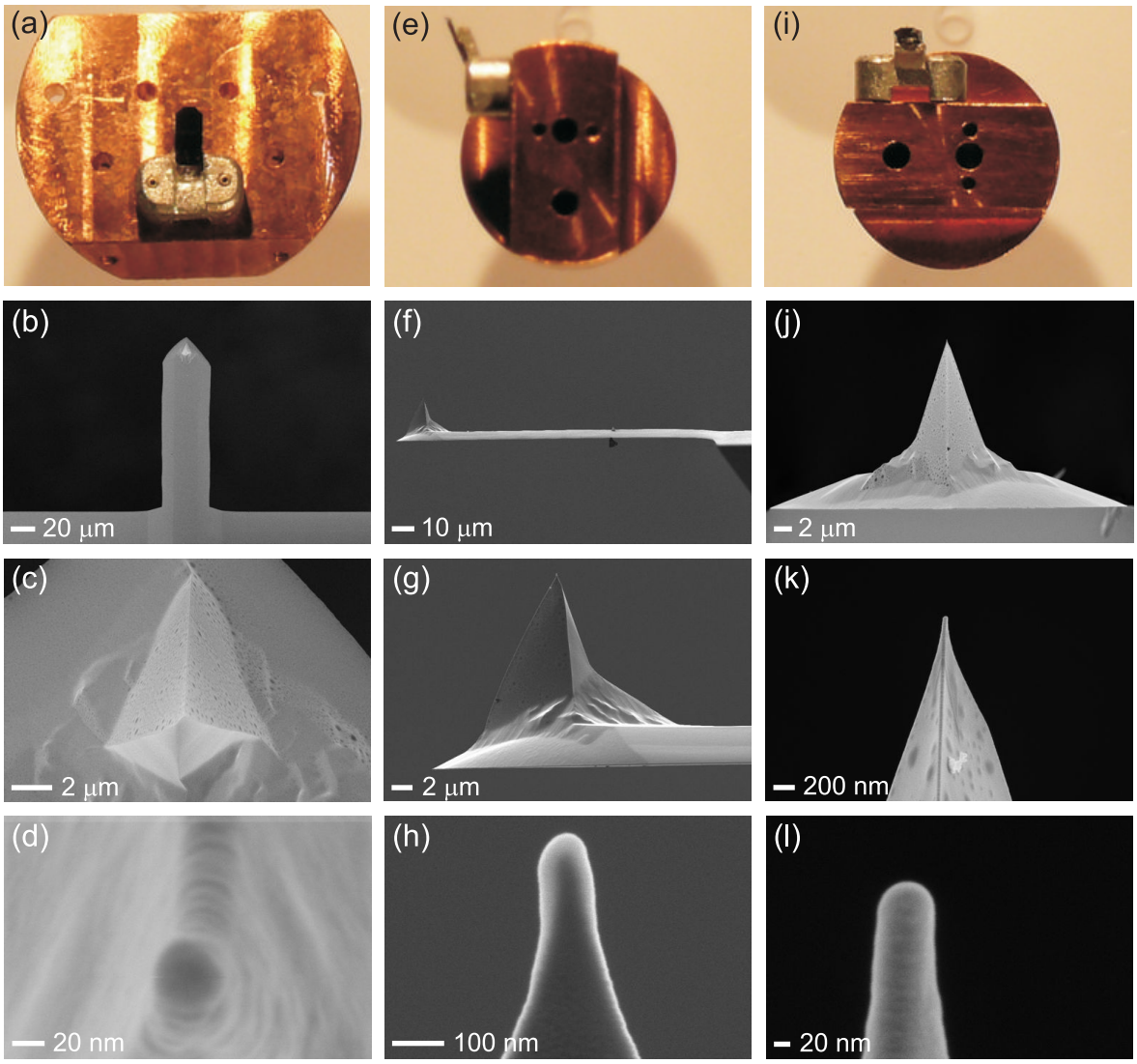

Figure 2.41: Cantilever AG 3 (type NCHPt, $f_0 = 239781$ Hz) with PtIr coating glued on a holder for system C investigated in the SEM. (a) SEM compatible holder allowing to obtain top view images of a cantilever equipped with cantilever holder and glued cantilever. (b)-(d) top view images with increasing magnification. (e) Holder for side view images. (f)-(h) side view images with increasing magnification. (i) Holder for front view images. (j)-(l) front view images with increasing magnification. (SEM images obtained by Bernd Walkenfort, Universität Osnabrück.)

2.6.6 Static cantilever stiffness measurement

To verify the cantilever stiffness obtained from dimensional analysis, a static stiffness measurement setup located at the Physikalisch-Technische Bundesanstalt (PTB, Braunschweig, Germany) is used. For a measurement, a cantilever is glued its their support chip on stainless a steel plate that is magnetically fixed to the stamp of a precision balance. The cantilever is bent by an edge attached to a precision positioning unit while the force applied to the cantilever is measured by the ultra-precision balance. The determination of the static stiffness from the resulting force-bending curves yields an uncertainty better than $\pm 5\%$. As the tip is pressed against an edge, this method is tip destructive and can, therefore, only applied after NC-AFM measurements. Measurements are performed under highly stabilised ambient temperature, pressure and humidity conditions. This setup and the respective measurements are described in detail in Chapter 5. It is also used as reference method for the measurements presented in Chapter 7.

3 Achieving high effective Q-factors in ultra-high vacuum dynamic force microscopy

Original publication: Measurement Science and Technology **21**, 125501 (2010)
available at http://dx.doi.org/10.1088/0957-0233/21/12/125501

J. Lübbe[1], L. Tröger[1], S. Torbrügge[1], R. Bechstein[1], C. Richter[2], A. Kühnle[3], M. Reichling[1]
[1] *Fachbereich Physik, Universität Osnabrück, Barbarastraße 7, 49076 Osnabrück, Germany*
[2] *Nanoworld Services GmbH, Schottkystraße 10, 91058 Erlangen, Germany*
[3] *Institut für Physikalische Chemie, Johannes Gutenberg-Universität Mainz, Jakob-Welder Weg 11, 55099 Mainz, Germany*

Electronic mail: reichling@uos.de

Abstract
The effective Q-factor of the cantilever is one of the most important figures-of-merit for a non-contact atomic force microscope (NC-AFM) operated in ultra-high vacuum (UHV). We provide a comprehensive discussion of all effects influencing the Q-factor and compare measured Q-factors to results from simulations based on the dimensions of the cantilevers. We introduce a methodology to investigate in detail how the effective Q-factor depends on the fixation technique of the cantilever. Fixation loss is identified as a most important contribution in addition to the hitherto discussed effects and we describe a strategy for avoiding fixation loss and obtaining high effective Q-factors in the force microscope. We demonstrate for room temperature operation, that an optimum fixation yields an effective Q-factor for the NC-AFM measurement in UHV that is equal to the intrinsic value of the cantilever.

4 Measurement and modelling of non-contact atomic force microscope cantilever properties from ultra-high vacuum to normal pressure conditions

Original publication: Measurement Science and Technology **22**, 055501 (2011)
available at http://dx.doi.org/10.1088/0957-0233/22/5/055501

J. Lübbe, M. Temmen, H. Schnieder, M. Reichling
Fachbereich Physik, Universität Osnabrück, Barbarastraße 7, 49076 Osnabrück, Germany

Electronic mail: reichling@uos.de

Abstract
The resonance frequency and Q-factor of cantilevers typically used for non-contact atomic force microscopy (NC-AFM) are measured as a function of the ambient pressure varied from 10^{-8} mbar to normal pressure. The Q-factor is found to be almost constant up to a pressure in the range of 10^{-2}–10^{-1} mbar and then decreases by about three orders of magnitude when increasing the pressure further to normal pressure. The decrease in the resonance frequency measured over the same pressure range amounts to less than 1% where a significant change is observed in the range of 10–10^{3} mbar. The pressure dependence of the effective Q-factor and resonance frequency is approximated by analytical models accounting for different processes in the molecular and viscous flow regimes. By introducing a heuristic approach for describing the pressure dependence in the transition regime, we are able to well approximate the cantilever properties over the entire pressure range.

5 Precise determination of force microscopy cantilever stiffness from dimensions and eigenfrequencies

Original publication: Measurement Science and Technology **23**, 045401 (2012)
available at http://dx.doi.org/10.1088/0957-0233/23/4/045401

J. Lübbe[1], L. Doering[2], M. Reichling[1]
[1] *Fachbereich Physik, Universität Osnabrück, Barbarastraße 7, 49076 Osnabrück, Germany*
[2] *Physikalisch-Technische Bundesanstalt (PTB), Nano- and Micrometrology, Bundesallee 100, 38116 Braunschweig, Germany*

Electronic mail: reichling@uos.de and lutz.doering@ptb.de

Abstract
We demonstrate the non-destructive measurement of the stiffness of single-beam, monocrystalline silicon cantilevers with a trapezoidal cross-section and tips as used for atomic force microscopy from the knowledge of cantilever dimensions, eigenfrequencies and material parameters. This yields stiffness values with an uncertainty of $\pm 25\%$ as the result critically depends on the thickness of the cantilever that is experimentally difficult to determine. The uncertainty is reduced to $\pm 7\%$ when the measured fundamental eigenfrequency is included in the calculation and a tip mass correction is applied. The tip mass correction can be determined from the eigenfrequencies of the fundamental and first harmonic modes. Results are verified by tip destructive measurements of the stiffness with a precision instrument recording a force-bending curve yielding an uncertainty better than $\pm 5\%$.

6 Thermal noise limit for ultra-high vacuum noncontact atomic force microscopy

Original publication: Beilstein Journal of Nanotechnology **4**, 32 (2013)
available at http://dx.doi.org/10.3762/bjnano.4.4

J. Lübbe[1], M. Temmen[1], S. Rode[2], P. Rahe[2], A. Kühnle[2], M. Reichling[1]
[1] *Fachbereich Physik, Universität Osnabrück, Barbarastraße 7, 49076 Osnabrück, Germany*
[2] *Institut für Physikalische Chemie, Johannes Gutenberg-Universität Mainz, Duesbergweg 10-14, 55099 Mainz, Germany*

Electronic mail: reichling@uos.de

Abstract
The noise of the frequency shift signal Δf in noncontact atomic force microscopy (NC-AFM) consists of cantilever thermal noise, tip-surface-interaction noise and instrumental noise from the detection and signal processing systems. We investigate how the displacement-noise spectral density d^z at the input of the frequency demodulator propagates to the frequency-shift-noise spectral density $d^{\Delta f}$ at the demodulator output in dependence of cantilever properties and settings of the signal processing electronics in the limit of a negligible tip-surface interaction and a measurement under ultrahigh-vacuum conditions. For a quantification of the noise figures, we calibrate the cantilever displacement signal and determine the transfer function of the signal-processing electronics. From the transfer function and the measured d^z, we predict $d^{\Delta f}$ for specific filter settings, a given level of detection-system noise spectral density d^z_{ds} and the cantilever-thermal-noise spectral density d^z_{th}. We find an excellent agreement between the calculated and measured values for $d^{\Delta f}$. Furthermore, we demonstrate that thermal noise in $d^{\Delta f}$, defining the ultimate limit in NC-AFM signal detection, can be kept low by a proper choice of the cantilever whereby its Q-factor should be given most attention. A system with a low-noise signal detection and a suitable cantilever, operated with appropriate filter and feedback-loop settings allows room temperature NC-AFM measurements at a low thermal-noise limit with a significant bandwidth.

7 Determining cantilever stiffness from thermal noise

Original publication: Beilstein Journal of Nanotechnology **4**, 227 (2013)
available at http://dx.doi.org/10.3762/bjnano.4.23

J. Lübbe[1], M. Temmen[1], P. Rahe[2], A. Kühnle[2], M. Reichling[1]
[1] *Fachbereich Physik, Universität Osnabrück, Barbarastraße 7, 49076 Osnabrück, Germany*
[2] *Institut für Physikalische Chemie, Johannes Gutenberg-Universität Mainz, Duesbergweg 10-14, 55099 Mainz, Germany*

Electronic mail: reichling@uos.de

Abstract
We critically discuss the extraction of intrinsic cantilever properties, namely eigenfrequency f_n, quality factor Q_n and specifically the stiffness k_n of the nth cantilever oscillation mode from thermal noise by an analysis of the power spectral density of displacement fluctuations of the cantilever in contact with a thermal bath. The practical applicability of this approach is demonstrated for several cantilevers with eigenfrequencies ranging from 50 kHz to 2 MHz. As such an analysis requires a sophisticated spectral analysis, we introduce a new method to determine k_n from a spectral analysis of the demodulated oscillation signal of the excited cantilever that can be performed in the frequency range of 10 Hz to 1 kHz regardless of the eigenfrequency of the cantilever. We demonstrate that the latter method is in particular useful for noncontact atomic force microscopy (NC-AFM) where the required simple instrumentation for spectral analysis is available in most experimental systems.

8 Summary

Different methods for the determination of cantilever properties were investigated. The applied strategies include dimensional, static and dynamic measurements and benefits, drawbacks as well as absolute errors were discussed. A key aspect is the determination of the cantilever stiffness, which is essential for a quantitative NC-AFM data analysis including the retrieval of the tip-surface interaction force and potential. In a second part, a systematic analysis of the displacement noise in the cantilever oscillation detection was performed and a special focus was on the thermally excited cantilever oscillation. The influence of NC-AFM cantilever properties and experimental parameters on the total frequency shift noise as a limiting factor of NC-AFM imaging and spectroscopy was studied. The findings were utilised to describe optimum imaging parameters. Most interestingly, from this theory a new method for the determination of the cantilever stiffness from a frequency shift noise analysis was introduced for the first time.

The effective Q-factor of cantilevers, one of the most important figures-of-merit for NC-AFM operation in UHV, was investigated. Intrinsic Q-factors were calculated from cantilever dimensions and material properties. These calculations show that commercially available high-quality cantilever generally have high intrinsic Q-factors. The best measured effective Q-factors in UHV are close to these intrinsic values, however, it was realised that the Q-factor may be strongly reduced by unfavourable mounting of the cantilever. Gluing the cantilever to the holder is the most reliable method to yield a high effective Q-factor, while clamping yields large fluctuations unless utmost care in positioning the cantilever and cleanliness of the cantilever and holder is taken. Taking the necessary care in mounting the cantilever, it is possible to routinely obtain effective Q-factors in NC-AFM measurements in UHV that are within a 20% margin of the intrinsic Q-factor. To be on the safe side, the Q-factor should be verified for any cantilever mounted in the NC-AFM system as an ex-situ characterisation of cantilevers cannot guarantee high Q-factors in the NC-AFM system.

The resonance frequency and the effective Q-factor of a cantilever depend on the ambient pressure. Therefore, a measurement of both quantities starting from UHV up to normal pressure was presented for four cantilevers differing in geometry. For all cantilevers, the pressure dependence is well described by analytical models based on the physics of free molecular and viscous flow. The introduction of a heuristic approach for describing the pressure dependence in the transition regime allows one to well approximate the cantilever properties over the entire pressure range from 10^{-8} to 10^{3} mbar. The Q-factor is found to be almost constant from UHV up to a pressure in the range of 10^{-2} to 10^{-1} mbar. A further increase of the pressure to normal pressure yields a decrease of the Q-factor by up to three orders of magnitude, depending on the cantilever dimensions. However, the shift

of the resonance frequency is less than 1% over the full pressure range under investigation, where the only significant change is observed in the range of 10 to 10^3 mbar. Comparing the results obtained under low-pressure with high-pressure conditions it became apparent that measurements of Q-factors at ambient pressure conditions cannot give any reliable information about the intrinsic Q-factor. However, a reliable prediction of the resonance frequency is possible.

The stiffness of cantilevers with rectangular cross-sections can be calculated from their dimensions and material parameters. This strategy was found to yield values k_{dim} with an uncertainty of $\pm 25\%$. This method mainly suffers from the uncertainty of the cantilever thickness due to its difficult experimental determination. To remove the thickness dependence from the stiffness calculation, the relation between the eigenfrequency of the cantilever and its dimensions can be utilized. However, calculated eigenfrequencies are typically overestimated by about 15% due to the additional mass of the tip at the end. A tip mass correction is, therefore, required and is realised employing the eigenfrequencies of the fundamental and first harmonic modes. Still, a limitation of the method are systematic errors introduced by inhomogeneities in the cantilever cross-section or thickness caused by disturbances during etching. The ultimate uncertainty in the determination of the stiffness k_{dim,f_0} from cantilever dimensions and eigenfrequencies is $\pm 7\%$. Approximating the trapezoidal cross-section as being rectangular by using its mean width and ignoring the decrease of Young's modulus due the doping of silicon typically yields an overestimate of 3% for k_{dim} and an underestimate of 2.5% for k_{dim,f_0}. Results are verified by tip-destructive static measurements of the stiffness k_{stat} with a precision instrument recording a force-bending curve with an uncertainty better than $\pm 5\%$.

The relation between the displacement noise in NC-AFM measurements and the corresponding frequency shift noise at the output of the demodulator was investigated. Frequency shift noise predictions based on demodulator transfer functions are found to be well reproduced by experiments. For a quantitative analysis of the noise, a precise amplitude calibration of the detection system is inevitable. The displacement noise of an NC-AFM system can be measured directly with a spectrum analyser at the output of the detection system. The thermal component of the displacement noise extracted from such spectra agrees well with spectra derived from a model for thermal cantilever oscillation. The noise contribution of the detection system can be obtained from the white noise floor of the measured spectrum. The knowledge of the detection system transfer functions allows one to predict the frequency shift noise from the measured displacement noise. A measurement of the detection system noise floor from the frequency shift noise is possible and was presented herein for the first time. While the former analysis requires a spectrum analyser with very high resolution and an operating range including the eigenfrequency of the cantilever, the latter procedure requires only a measurement of the frequency shift noise with a device covering the frequency range between about 10 Hz and 10 kHz at moderate frequency resolution. Therefore, a rather complete noise characterisation with a simple spectrum analyser as integrated in many NC-AFM systems is possible for a fully calibrated system. The framework of modelling noise in NC-AFM systems in combination with the experimental practice developed here provides a clear guideline for system design and the choice of experimen-

tal parameters for thermal noise limited operation. The analysis shows that for a noise optimised NC-AFM measurement, the suitable choice of the cantilever is most important. Especially obtaining a high effective Q-factor should be given great attention to keep the level of thermal noise to a minimum. The bandwidth of thermal noise limited operation is determined by the noise generated in the detection system. By an appropriate choice of PLL filter settings, one can make full use of this bandwidth without limiting the NC-AFM signal while, at the same time, most efficiently eliminating most of the detection system noise. It is found that with a technically optimised system and an appropriate choice of experimental parameters, room temperature thermal noise limited NC-AFM measurements over a bandwidth of typically 100 Hz are possible.

The aforementioned findings on thermal noise in the NC-AFM can be employed for the determination of cantilever properties. Here, especially the stiffness is essential for a quantitative analysis of any kind of NC-AFM force spectroscopy. The intrinsic cantilever properties eigenfrequency, Q-factor and the stiffness for the nth oscillation mode can be obtained from a calibrated spectrum of the thermally excited displacement noise spectral density measured around the cantilever resonance. Using the previously found relations between displacement noise and frequency shift noise, the stiffness can be obtained from a measurement of the frequency shift noise spectral density in the frequency range of 10 Hz to 1 kHz at the output of the demodulator if the cantilever eigenfrequency and the Q-factor are known. These methods allow one to extract the modal stiffness for several eigenmodes of a cantilever without any knowledge of the cantilever dimensions and tip mass. Stiffness results are compared to calculations based on the cantilever dimensions and reference experiments based on an independent static stiffness measurement. The stiffness determination performed directly from the displacement noise spectral density yields an error of about 10% compared to the reference values while the stiffness determination from the frequency shift noise spectral density yields uncertainties of about 20%. Modal stiffness values for higher harmonics are verified within the framework of cantilever oscillation theory as the modal stiffness can not be directly compared to static stiffness values. Measurements reveal a strong influence of the tip mass on the modal stiffness of higher harmonic eigenmodes.

It was experimentally shown that additional frequency shift noise contributions in the frequency range of 10 Hz to 1 kHz appear at a close tip-sample distance. This additional noise can be modeled by consideration of the coupling of PLL, amplitude and distance feedback loops. The simulations illustrate that high Q-factors may yield a lower frequency shift noise, but are more critical regarding the feedback settings and the excitation of spurious oscillations.

Bibliography

[1] G. Binnig, H. Rohrer, C. Gerber, E. Weibel: Surface Studies by Scanning Tunneling Microscopy.
Phys. Rev. Lett. **49**, 57 (1982). – DOI 10.1103/PhysRevLett.49.57

[2] G. Binnig, H. Rohrer: Scanning tunneling microscopy.
Surf. Sci. **126**, 236 (1983). – DOI 10.1016/0039–6028(83)90716–1

[3] G. Binnig, C. F. Quate, C. Gerber: Atomic Force Microscope.
Phys. Rev. Lett. **56**, 930 (1986). – DOI 10.1103/PhysRevLett.56.930

[4] T. R. Albrecht, P. Grütter, D. Horne, D. Rugar: Frequency modulation detection using high-Q cantilevers for enhanced force microscope sensitivity.
J. Appl. Phys. **69**, 668 (1991). – DOI 10.1063/1.347347

[5] F. J. Giessibl: Atomic Resolution of the Silicon (111)-(7x7) Surface by Atomic Force Microscopy.
Science **267**, 68 (1995). – DOI 10.1126/science.267.5194.68

[6] S. Kitamura, M. Iwatsuki: Observation of $\mathbf{7 \times 7}$ Reconstructed Structure on the Silicon (111) Surface using Ultrahigh Vacuum Noncontact Atomic Force Microscopy.
Jpn. J. Appl. Phys. **34**, L145 (1995). – DOI 10.1143/JJAP.34.L145

[7] M. Bammerlin, R. Lüthi, E. Meyer, A. Baratoff, J. Lü, M. Guggisberg, C. Gerber, L. Howald, H.-J. Güntherodt: True Atomic Resolution on the Surface of an Insulator via Ultrahigh Vacuum Dynamic Force Microscopy.
Probe Microscopy **1**, 3 (1997)

[8] M. Reichling, C. Barth: Scanning Force Imaging of Atomic Size Defects on the $CaF_2(111)$ Surface.
Phys. Rev. Lett. **83**, 768 (1999). – DOI 10.1103/PhysRevLett.83.768

[9] J. V. Lauritsen, M. Reichling: Atomic resolution non-contact atomic force microscopy of clean metal oxide surfaces.
J. Phys. Condens. Matter **22**, 263001 (2010). – DOI 10.1088/0953–8984/22/26/263001

[10] Y. Sugimoto, P. Pou, M. Abe, P. Jelinek, R. Perez, S. Morita, O. Custance: Chemical identification of individual surface atoms by atomic force microscopy.
Nature **446**, 64 (2007). – DOI 10.1038/nature05530

[11] Y. Sugimoto, T. Namikawa, K. Miki, M. Abe, S. Morita: Vertical and lateral force mapping on the $\mathrm{Si}(111)$-(7×7) surface by dynamic force microscopy.
Phys. Rev. B **77**, 195424 (2008). – DOI 10.1103/PhysRevB.77.195424

[12] K. Ruschmeier, A. Schirmeisen, R. Hoffmann: Site-specific force-vector field studies of KBr(001) by atomic force microscopy.
Nanotechnology **20**, 264013 (2009). – DOI 10.1088/0957–4484/20/26/264013

[13] B. Such, T. Glatzel, S. Kawai, S. Koch, E. Meyer: Three-dimensional force spectroscopy of KBr(001) by tuning fork-based cryogenic noncontact atomic force microscopy.
J. Vac. Sci. Technol. B **28**, C4B1 (2010). – DOI 10.1116/1.3382230

[14] S. Kawai, T. Glatzel, S. Koch, A. Baratoff, E. Meyer: Interaction-induced atomic displacements revealed by drift-corrected dynamic force spectroscopy.
Phys. Rev. B **83**, 035421 (2011). – DOI 10.1103/PhysRevB.83.035421

[15] P. Rahe, J. Schütte, W. Schniederberend, M. Reichling, M. Abe, Y. Sugimoto, A. Kühnle: Flexible drift-compensation system for precise 3D force mapping in severe drift environments.
Rev. Sci. Instrum. **82**, 063704 (2011). – DOI 10.1063/1.3600453

[16] T. Fukuma, M. Kimura, K. Kobayashi, K. Matsushige, H. Yamada: Development of low noise cantilever deflection sensor for multienvironment frequency-modulation atomic force microscopy.
Rev. Sci. Instrum. **76**, 053704 (2005). – DOI dx.doi.org/10.1063/1.1896938

[17] K. Kobayashi, H. Yamada, K. Matsushige: Frequency noise in frequency modulation atomic force microscopy.
Rev. Sci. Instrum. **80**, 043708 (2009). – DOI 10.1063/1.3120913

[18] J. Polesel-Maris, M. A. Venegas de la Cerda, D. Martrou, S. Gauthier: Noise in frequency-modulation dynamic force microscopy.
Phys. Rev. B **79**, 235401 (2009). – DOI 10.1103/PhysRevB.79.235401

[19] F. J. Giessibl, H. Bielefeldt, S. Hembacher, J. Mannhart: Calculation of the optimal imaging parameters for frequency modulation atomic force microscopy.
Appl. Surf. Sci. **140**, 352 (1999). – DOI 10.1016/S0169–4332(98)00553–4

[20] U. Gysin, S. Rast, P. Ruff, E. Meyer, D. W. Lee, P. Vettiger, C. Gerber: Temperature dependence of the force sensitivity of silicon cantilevers.
Phys. Rev. B **69**, 045403 (2004). – DOI 10.1103/PhysRevB.69.045403

[21] F. J. Giessibl, F. Pielmeier, T. Eguchi, T. An, Y. Hasegawa: Comparison of force sensors for atomic force microscopy based on quartz tuning forks and length-extensional resonators.
Phys. Rev. B **84**, 125409 (2011). – DOI 10.1103/PhysRevB.84.125409

[22] P. Rahe, R. Bechstein, A. Kühnle: Vertical and lateral drift corrections of scanning probe microscopy images.
J. Vac. Sci. Technol. B **28**, C4E31 (2010). – DOI 10.1116/1.3360909

[23] M. Abe, Y. Sugimoto, O. Custance, S. Morita: Atom tracking for reproducible force spectroscopy at room temperature with non-contact atomic force microscopy.
Nanotechnology **16**, 3029 (2005). – DOI 10.1088/0957–4484/16/12/050

[24] M. Abe, Y. Sugimoto, T. Namikawa, K. Morita, N. Oyabu, S. Morita: Drift-compensated data acquisition performed at room temperature with frequency modulation atomic force microscopy.
Appl. Phys. Lett. **90**, 203103 (2007). – DOI 10.1063/1.2739410

[25] M. A. Lantz, H. J. Hug, R. Hoffmann, P. J. A. van Schendel, P. Kappenberger, S. Martin, A. Baratoff, H.-J. Güntherodt: Quantitative Measurement of Short-Range Chemical Bonding Forces.
Science **291**, 2580 (2001). – DOI 10.1126/science.1057824

[26] J. Welker, E. Illek, F. J. Giessibl: Analysis of force-deconvolution methods in frequency-modulation atomic force microscopy.
Beilstein J. Nanotechnol. **3**, 238 (2012). – DOI 10.3762/bjnano.3.27

[27] F. J. Giessibl: High-speed force sensor for force microscopy and profilometry utilizing a quartz tuning fork.
Appl. Phys. Lett. **73**, 3956 (1998). – DOI 10.1063/1.122948

[28] T. An, T. Nishio, T. Eguchi, M. Ono, A. Nomura, K. Akiyama, Y. Hasegawa: Atomically resolved imaging by low-temperature frequency-modulation atomic force microscopy using a quartz length-extension resonator.
Rev. Sci. Instrum. **79**, 033703 (2008). – DOI 10.1063/1.2830937

[29] P. A. Rahe: The Calcite(10$\bar{1}$4) Surface: A Versatile Substrate for Molecular Self-Assembly, Johannes Gutenberg Universität Mainz, Diss., 2011

[30] J. E. Sader, S. P. Jarvis: Accurate formulas for interaction force and energy in frequency modulation force spectroscopy.
Appl. Phys. Lett. **84**, 1801 (2004). – DOI 10.1063/1.1667267

[31] F. J. Giessibl: A direct method to calculate tip–sample forces from frequency shifts in frequency-modulation atomic force microscopy.
Appl. Phys. Lett. **78**, 123 (2001). – DOI 10.1063/1.1335546

[32] L. Gross, F. Mohn, N. Moll, P. Liljeroth, G. Meyer: The Chemical Structure of a Molecule Resolved by Atomic Force Microscopy.
Science **325**, 1110 (2009). – DOI 10.1126/science.1176210

[33] J. N. Israelachvili: Intermolecular and Surface Forces. Second Edition, reprinted. London, UK : Academic Press, 2006. – ISBN 978–0–12–375181–2

[34] H. Hamaker: The London-van der Waals attraction between spherical particles.
Physica **4**, 1058 (1937). – DOI 10.1016/S0031–8914(37)80203–7

[35] F. London: The general theory of molecular forces.
Trans. Faraday Soc. **33**, 8b (1937). – DOI 10.1039/TF937330008B

[36] S. Sadewasser, M. C. Lux-Steiner: Correct Height Measurement in Noncontact Atomic Force Microscopy.
Phys. Rev. Lett. **91**, 266101 (2003). – DOI 10.1103/PhysRevLett.91.266101

[37] W. Melitz, J. Shen, A. C. Kummel, S. Lee: Kelvin probe force microscopy and its application.
Surf. Sci. Rep. **66**, 1 (2011). – DOI 10.1016/j.surfrep.2010.10.001

[38] J. E. Lennard-Jones: Cohesion.
Proc. Phys. Soc. **43**, 461 (1931). – DOI 10.1088/0959–5309/43/5/301

[39] F. J. Giessibl: Forces and frequency shifts in atomic-resolution dynamic-force microscopy.
Phys. Rev. B: Condens. Matter **56**, 16010 (1997). – DOI 10.1103/PhysRevB.56.16010

[40] P. M. Morse: Diatomic Molecules According to the Wave Mechanics. II. Vibrational Levels.
Phys. Rev. **34**, 57 (1929). – DOI 10.1103/PhysRev.34.57

[41] R. A. Buckingham: The Classical Equation of State of Gaseous Helium, Neon and Argon.
Proc. R. Soc. Lond. A **168**, 264 (1938). – DOI 10.1098/rspa.1938.0173

[42] F. H. Stillinger, T. A. Weber: Computer simulation of local order in condensed phases of silicon.
Phys. Rev. B **31**, 5262 (1985). – DOI 10.1103/PhysRevB.31.5262

[43] P. Rahe, R. Bechstein, J. Schütte, F. Ostendorf, A. Kühnle: Repulsive interaction and contrast inversion in noncontact atomic force microscopy imaging of adsorbates.
Phys. Rev. B **77**, 195410 (2008). – DOI 10.1103/PhysRevB.77.195410

[44] M. Guggisberg, M. Bammerlin, C. Loppacher, O. Pfeiffer, A. Abdurixit, V. Barwich, R. Bennewitz, A. Baratoff, E. Meyer, H.-J. Güntherodt: Separation of interactions by noncontact force microscopy.
Phys. Rev. B **61**, 11151 (2000). – DOI 10.1103/PhysRevB.61.11151

[45] J. E. Sader, S. P. Jarvis: Mathematica® notebook for implementation of formulas. – http://www.ampc.ms.unimelb.edu.au/afm/bibliography.html#FMAFM – (accessed May 7, 2012)

[46] R. G. D. Steel, J. H. Torrie, D. A. Dickey: *Principles and procedures of statistics: a biometrical approach*. McGraw-Hill, 1997 (McGraw-Hill series in probability and statistics). – ISBN 9780070610286

[47] O. Wolter, T. Bayer, J. Greschner: Micromachined silicon sensors for scanning force microscopy.
J. Vac. Sci. Technol. B **9**, 1353 (1991). – DOI 10.1116/1.585195

[48] J. Lübbe, L. Doering, M. Reichling: Precise determination of force microscopy cantilever stiffness from dimensions and eigenfrequencies.
Measurement Science and Technology **23**, 045401 (2012)

[49] F. J. Elmer, M. Dreier: Eigenfrequencies of a rectangular atomic force microscope cantilever in a medium.
J. Appl. Phys. **81**, 7709 (1997). – DOI 10.1063/1.365379

[50] H. J. Butt, M. Jaschke: CALCULATION OF THERMAL NOISE IN ATOMIC-FORCE MICROSCOPY.
Nanotechnology **6**, 1 (1995). – DOI 10.1088/0957–4484/6/1/001

[51] J. R. Lozano, D. Kiracofe, J. Melcher, R. Garcia, A. Raman: Calibration of higher eigenmode spring constants of atomic force microscope cantilevers.
Nanotechnology **21**, 465502 (2010). – DOI 10.1088/0957–4484/21/46/465502

[52] C. J. Chen: Introduction to Scanning Tunneling Microscopy. New York : Oxford University Press, 1993. – ISBN 978–0–19–921150–0

[53] D. Kiracofe, A. Raman: On eigenmodes, stiffness, and sensitivity of atomic force microscope cantilevers in air versus liquids.
J. Appl. Phys. **107**, 033506 (2010). – DOI 10.1063/1.3284206

[54] J. Melcher, S. Q. Hu, A. Raman: Equivalent point-mass models of continuous atomic force microscope probes.
Appl. Phys. Lett. **91**, 053101 (2007). – DOI 10.1063/1.2767173

[55] M. S. Allen, H. Sumali, P. C. Penegor: DMCMN: Experimental/Analytical Evaluation of the Effect of Tip Mass on Atomic Force Microscope Cantilever Calibration.
J. Dyn. Sys., Meas., Control **131**, 064501 (2009). – DOI 10.1115/1.4000160

[56] F. J. Giessibl: Advances in atomic force microscopy.
Rev. Mod. Phys. **75**, 949 (2003). – DOI 10.1103/RevModPhys.75.949

[57] W. Nolting: Grundkurs Theoretische Physik 1: Klassische Mechanik. 6. Auflage. Springer, 2003. – ISBN 3–540–42115–7

[58] H. Nyquist: Thermal Agitation of Electric Charge in Conductors.
Phys. Rev. **32**, 110 (1928). – DOI 10.1103/PhysRev.32.110

[59] F. Reif: *Fundamentals of statistical and thermal physics*. Auckland : McGraw-Hill, 2008 (McGraw-Hill series in fundamentals of physics). – ISBN 0–07–085615–X

[60] J. L. Hutter, J. Bechhoefer: Calibration of atomic-force microscope tips.
Rev. Sci. Instrum. **64**, 1868 (1993). – DOI 10.1063/1.1143970

[61] S. M. Cook, T. E. Schäffer, K. M. Chynoweth, M. Wigton, R. W. Simmonds, K. M. Lang: Practical implementation of dynamic methods for measuring atomic force microscope cantilever spring constants.
Nanotechnology **17**, 2135 (2006). – DOI 10.1088/0957–4484/17/9/010

[62] H. Geschwinde: Einführung in die PLL-Technik. Braunschweig : Vieweg, 1978. – ISBN 3–528–04077–7

[63] A. Kühnle, G. Meyer, S. W. Hla, K.-H. Rieder: Understanding atom movement during lateral manipulation with the STM tip using a simple simulation method.
Surf. Sci. **499**, 15 (2002). – DOI 10.1016/S0039–6028(01)01848–9

[64] L. Howald, E. Meyer, R. Lüthi, H. Haefke, R. Overney, H. Rudin, H.-J. Güntherodt: Multifunctional probe microscope for facile operation in ultrahigh vacuum.
Appl. Phys. Lett. **63**, 117 (1993). – DOI 10.1063/1.109732

[65] S. Torbrügge, J. Lübbe, L. Tröger, M. Cranney, T. Eguchi, Y. Hasegawa, M. Reichling: Improvement of a dynamic scanning force microscope for highest resolution imaging in ultrahigh vacuum.
Rev. Sci. Instrum. **79**, 083701 (2008). – DOI 10.1063/1.2964119

[66] R. Bechstein: Pristine and Doped Titanium Dioxide Studied by NC-AFM, Universität Osnabrück, Diss., 2009

[67] S. Hirth: Laterale Manipulation von Wassermolekülen auf Fluoridoberflächen, Universität Osnabrück, Diss., 2007

[68] F. Ostendorf: Strukturuntersuchungen an mineralischen und polaren Oberflächen, Universität Osnabrück, Diss., 2008

[69] F. Loske: Tailoring molecule nanostructures on insulating surfaces investigated by non-contact atomic force microscopy, Johannes Gutenberg Universität Mainz, Diss., 2011

[70] K. Besocke: An easily operable scanning tunneling microscope.
Surf. Sci. **181**, 145 (1987). – DOI 10.1016/0039–6028(87)90151–8

[71] Q. Dai, R. Vollmer, R. W. Carpick, D. F. Ogletree, M. Salmeron: A variable temperature ultrahigh vacuum atomic force microscope.
Rev. Sci. Instrum. **66**, 5266 (1995). – DOI 10.1063/1.1146097

[72] J. Lübbe, H. Schnieder, M. Reichling: Pressure dependence of the Q-factor of cantilevers used for NC-AFM.
e-J. Surf. Sci. Nanotech. **9**, 30 (2011). – DOI 10.1380/ejssnt.2011.30

[73] J. Lübbe, M. Temmen, H. Schnieder, M. Reichling: Measurement and modelling of non-contact atomic force microscope cantilever properties from ultra-

high vacuum to normal pressure conditions.
Meas. Sci. Technol. **22**, 055501 (2011). – DOI 10.1088/0957–0233/22/5/055501

Publications and presentations

Publications in peer-reviewed journals

- **Improvement of a dynamic scanning force microscope for highest resolution imaging in ultrahigh vacuum**
  S. Torbrügge, J. Lübbe, L. Tröger, M. Cranney, T. Eguchi, Y. Hasegawa, M. Reichling
  Rev. Sci. Instrum. **79**, 083701 (2008). – DOI 10.1063/1.2964119
- **Quantitative description of C_{60} diffusion on an insulating surface**
  F. Loske, J. Lübbe, J. Schütte, M. Reichling, A. Kühnle
  Phys. Rev. B **82**, 155428 (2010). – DOI 10.1103/PhysRevB.82.155428
- **Achieving high effective Q-factors in ultra-high vacuum dynamic force microscopy**
  J. Lübbe, L. Tröger, S. Torbrügge, R. Bechstein, A. Kühnle, M. Reichling
  Meas. Sci. Technol. **21**, 125501 (2010). – DOI 10.1088/0957-0233/21/12/125501
- **Pressure Dependence of the Q-factor of Cantilevers Used for NC-AFM**
  J. Lübbe, H. Schnieder, M. Reichling
  e-J. Surf. Sci. Nanotech. **9**, 30 (2011). – DOI 10.1380/ejssnt.2011.30
- **Measurement and modelling of non-contact atomic force microscope cantilever properties from ultra-high vacuum to normal pressure conditions**
  J. Lübbe, M. Temmen, H. Schnieder, M. Reichling
  Meas. Sci. Technol. **22**, 055501 (2011). – DOI 10.1088/0957-0233/22/5/055501
- **Modification of a commercial AFM for low-noise, high-resolution frequency-modulation imaging in liquid environment**
  S. Rode, R. Stark, J. Lübbe, L. Tröger, J.Schütte, K. Umeda, K. Kobayashi, H. Yamada, A. Kühnle
  Rev. Sci. Instrum. **82**, 073703 (2011). – DOI 10.1063/1.3606399
- **Precise determination of force microscopy cantilever stiffness from dimensions and eigenfrequencies**
  J. Lübbe, L. Doering, M. Reichling
  Meas. Sci. Technol. **23**, 045401 (2012). – DOI 10.1088/0957-0233/23/4/045401

- **Thermal noise limit for ultra-high vacuum noncontact atomic force microscopy**
  J. Lübbe, M. Temmen, S. Rode, P. Rahe, A. Kühnle, M. Reichling
  Beilstein J. Nanotechnol. **4**, 32 (2013). – DOI 10.3762/bjnano.4.4
- **Determining cantilever stiffness from thermal noise**
  J. Lübbe, M. Temmen, P. Rahe, A. Kühnle, M. Reichling
  Beilstein J. Nanotechnol. **4**, 227 (2013). – DOI 10.3762/bjnano.4.23

Conference contributions

(presenting author is underlined)

Talks

- **Optimum excitation and detection of cantilever oscillation in vacuum**
  J. Lübbe, S. Torbrügge, S. Gritschneder, L. Tröger, M. Cranney, T. Eguchi, Y. Hasegawa, M. Reichling
  (DPG spring meeting 2007, Regensburg, Germany)
- **Extracting intrinsic cantilever properties from thermal noise**
  J. Lübbe, M. Temmen, P. Rahe, A. Kühnle, M. Reichling
  (DPG spring meeting 2012, Berlin, Germany)
- **Morphology and electric potential of C_{60} islands on $CaF_2(111)$**
  M. Temmen, J. Schütze, P. Sommer, J. Lübbe, M. Reichling
  (NC-AFM 2012, Český Krumlov, Czech republic)

Posters

- **Significant performance improvement of a commercial dynamic scanning force microscope**
  J. Lübbe, S. Torbrügge, L. Tröger, M. Cranney, T. Eguchi, Y. Hasegawa, M. Reichling
  (NC-AFM 2008, Madrid, Spain)
- **Measuring and optimising quality factors Q of cantilevers used in dynamic force microscopy**
  J. Lübbe, S. Torbrügge, L. Tröger, M. Reichling
  (NC-AFM 2008, Madrid, Spain)
- **A practical guide to high effective Q-factors for cantilever based NC-AFM**
  J. Lübbe, L.Tröger, S. Torbrügge, R. Bechstein, C. Richter, A. Kühnle, M. Reichling
  (NC-AFM 2010, Kanazawa, Japan)
- **Complete characterisation of cantilevers for precision NC-AFM in the UHV**
  J. Lübbe, S. Rode, F. Loske, A. Kühnle, M. Reichling
  (NC-AFM 2010, Kanazawa, Japan)
- **Noise figures of optimised, cantilever-based NC-AFM systems for high resolution imaging in the ultra-high vacuum**
  J. Lübbe, S. Rode, P. Rahe, A. Kühnle and M. Reichling
  (NC-AFM 2010, Kanazawa, Japan)

- **Determination of cantilever stiffness from dimensions and eigenfrequencies**
  J. Lübbe, L. Doering, M. Reichling
  (NC-AFM 2011, Lindau, Germany)
- **Quantification of noise in NC-AFM systems for UHV applications**
  J. Lübbe, M. Temmen, S. Rode, M. Reichling
  (NC-AFM 2011, Lindau, Germany)
- **Measurement of intrinsic cantilever properties from thermal noise**
  J. Lübbe, M. Temmen, M. Reichling
  (NC-AFM 2011, Lindau, Germany)
- **Precise determination of force microscopy cantilever stiffness from dimensions and eigenfrequencies**
  J. Lübbe, L. Doering, M. Reichling
  (DPG spring meeting 2012, Berlin, Germany)
- **How to operate a non-contact atomic force microscope (NC-AFM) for ultra-high vacuum applications at the thermal noise limit**
  M. Temmen, J. Lübbe, S. Rode, P. Rahe, A. Kühnle, M. Reichling
  (DPG spring meeting 2012, Berlin, Germany)
- **Precise characterisation of CaF_2(111) by NC-AFM and KPFM**
  M. Temmen, J. Lübbe, T. Bollmann, M. Reichling
  (NC-AFM 2012, Český Krumlov, Czech republic)